UNIVERSITY OF ALBERTA

Evaluation of Air Flow in the Unsaturated Zone During Soil Vapour Extraction from Horizontal and Vertical Wells

BY

Darlene Victoria Atkinson ©

A thesis submitted to the Faculty of Graduate Studies and Research in partial fulfillment of the requirements for the degree of Master of Science.

DEPARTMENT OF EARTH AND ATMOSPHERIC SCIENCES

Edmonton, Alberta
Fall 1999

National Library
of Canada

Acquisitions and
Bibliographic Services

395 Wellington Street
Ottawa ON K1A 0N4
Canada

Bibliothèque nationale
du Canada

Acquisitions et
services bibliographiques

395, rue Wellington
Ottawa ON K1A 0N4
Canada

Your file Votre référence

Our file Notre référence

The author has granted a non-exclusive licence allowing the National Library of Canada to reproduce, loan, distribute or sell copies of this thesis in microform, paper or electronic formats.

L'auteur a accordé une licence non exclusive permettant à la Bibliothèque nationale du Canada de reproduire, prêter, distribuer ou vendre des copies de cette thèse sous la forme de microfiche/film, de reproduction sur papier ou sur format électronique.

The author retains ownership of the copyright in this thesis. Neither the thesis nor substantial extracts from it may be printed or otherwise reproduced without the author's permission.

L'auteur conserve la propriété du droit d'auteur qui protège cette thèse. Ni la thèse ni des extraits substantiels de celle-ci ne doivent être imprimés ou autrement reproduits sans son autorisation.

0-612-47004-0

Canada

UNIVERSITY OF ALBERTA

LIBRARY RELEASE FORM

NAME OF AUTHOR: Darlene Victoria Atkinson

TITLE OF THESIS: Evaluation of Air Flow in the Unsaturated Zone During Soil Vapour Extraction from Horizontal and Vertical Wells

DEGREE: Master of Science

YEAR THIS DEGREE GRANTED: 1999

Permission is hereby granted to the University of Alberta Library to reproduce single copies of this thesis and to lend or sell such copies for private, scholarly or scientific research purposes only.

The author reserves all other publication and other rights in association with the copyright in the thesis, and except as hereinbefore provided neither the thesis nor any substantial portion thereof may be printed or otherwise reproduced in any material form whatever without the author's prior written permission.

(Signed) D. Atkinson

Darlene Victoria Atkinson
Box 102
Kirkton Ontario
Canada, N0K 1K0

Date: Aug. 3, 1999

UNIVERSITY OF ALBERTA

FACULTY OF GRADUATE STUDIES AND RESEARCH

The undersigned certify that they have read, and recommend to the Faculty of Graduate Studies and Research for acceptance, a thesis entitled **Evaluation of Air Flow in the Unsaturated Zone During Soil Vapour Extraction from Horizontal and Vertical Wells** submitted by Darlene Victoria Atkinson in partial fulfillment of the requirements for the degree of Master of Science.

Carl Mendoza
Dr. C. A. Mendoza (Supervisor)

Kevin Biggar
Dr. K. W. Biggar (External)

Ben Rostron
Dr. B. J. Rostron (Examiner)

Dr. B. J. Rostron (Chair)

Date: Aug. 3/99

For my parents,
Diane and Don Atkinson
and my sisters,
Kathryn and Karen Atkinson

Abstract

Soil vapour extraction (SVE) is a remediation technique for removing volatile contaminants from the unsaturated zone. Quantifying the importance of the various processes and factors that control air flow during SVE is essential for predicting flow and transport of vapours. Air flow to both horizontal and vertical SVE wells was simulated for two field sites in Western Canada.

Two numerical models were used to simulate steady-state air flow: VapourT, a finite-element model (FEM) that simulates incompressible flow in either two-dimensional axisymmetric or cartesian coordinates; and AIR3D, a finite-difference model (FDM) that simulates compressible flow in three-dimensions. A one-dimensional analysis demonstrated that the difference between a compressible and incompressible flow analysis is minimal under typical SVE pressure drawdowns. A two-dimensional analysis of flow to vertical extraction wells showed that the two models can yield slightly different solutions because of differences in the FEM and FDM formulation. These differences are only minimal if the grid discretization is small in areas of large fluxes. AIR3D was used to estimate the unsaturated zone permeabilities from field data obtained during horizontal well SVE tests.

A sensitivity analysis was used to examine the impact of geological, hydrogeological and well parameters, and model design, on the air flow solution by comparing the pressure distributions, the travel times and flowpaths to the extraction well, and the volume of porous media influenced in a given time. Permeability and the presence of an impermeable cover were determined to be the most sensitive parameters examined. The large variance in the solutions resulting from small changes in

permeability, within expected ranges at the sites, emphasized the need for accurate parameter characterization with field and laboratory analyses.

Three-dimensional simulations demonstrated that the small pressure drawdowns created by a long horizontal well at one of the sites could be approximated with a two-dimensional cartesian coordinate solution, whereas the large pressure drawdowns created by a short horizontal well at the other site could be approximated with a two-dimensional axisymmetric flow solution.

Acknowledgements

I would like to thank my supervisor, Carl Mendoza, for all the assistance he provided during my time at U of A. Your support of my thesis and guidance in seeing to the end is appreciated. Thank-you to my committee members, Dr. Kevin Biggar and Dr. Ben Rostron, for their time and feedback on my thesis. Next I would like to thank the Department of Earth and Atmospheric Science for funding provided through Graduate Teaching & Research Assistantships. A special thank-you goes to James Armstrong at Komex International Ltd. for providing data and information on the two sites used in the thesis. I would also like to acknowledge Dr. Vicki Remenda and Dr. Bernard Kueper of Queen's University, and Jennifer McLellan and Ron Flemming at Centralia College who first sparked my interest in hydrogeology and encouraged me to enter grad school. And thanks Todd McAlary for all the interesting hydro discussions we had while I worked at Beak.

I would like to acknowledge everyone who has been in the Hydrogeology Group during my time at U of A. A special thank-you to Sheri, Leroy, Brent, Melody and Tannis for helping with all those "little" questions! I will always laugh when I hear our office mottos: "it's only a few lines of code" and "can you help me find this bug". And special thanks to Brent and Karen for your friendship, understanding and support. I would also like to thank Kerrie-Ann. You are a great friend and gave me so much support and advice even when you were across the Pond or in the Arctic. You have all my support while you finish off your PhD! And thanks goes to my EAS and Alberta friends.

Finally, biggest thanks to my family, my Mom and Dad, Diane and Don Atkinson,

and sisters, Karen and Kathryn. Without all your love and support, I wouldn't have made it through. Mom and Dad, thanks for encouraging your daughters to pursue our dreams and strive to be the best we can. And kisses and hugs to Gumbo, Kayley, Mikeal, Sly, Delcey and Clifford!

Contents

1 Introduction 1

1.1 Overview of Soil Vapour Extraction 1

1.2 Study Objectives 4

1.3 Literature Review 6

2 Theory 13

2.1 Conceptual Model 13

2.2 Mathematical Equations for Flow 18

2.2.1 Incompressible Flow 23

2.2.2 Compressible Flow 24

2.3 Boundary Conditions 25

2.4 End Effects 26

2.5 Flow Nets 30

2.6 Summary 31

3 Numerical Models 33

3.1 Overview of Models 33

3.1.1 Grid Design 34

3.1.2 Fluid Balance and Fate 37

3.2 Well Representation 38

3.3 Well Flux Calculations 40

3.4 Example Simulations 42

3.4.1 One-Dimensional Flow Analysis 43

List of Figures

1.1 NAPL phases and associated partitioning coefficients 2
1.2 Conceptual model of horizontal SVE system 2
1.3 Conceptual model of SVE 3

2.1 Conceptual model of the unsaturated and saturated zones 14
2.2 Conceptual model of oil and water distributions during watertable fluctuations 16
2.3 Conceptual model of horizontal well in 2D cartesian coordinates. . . 27
2.4 Two-dimensional cartesian coordinates simulation with symmetry boundary 27
2.5 Conceptual model of vertical well with axisymmetric coordinates. . . 28
2.6 Cross-section B-B′ from Figure 2.5. Two-dimensional axisymmetric coordinates simulation with symmetry boundary. 28
2.7 Representation of horizontal well in two-dimensions 29
2.8 Conceptual model of flow net transformation theory 32

3.1 Nodal connectivity for the FDM 35
3.2 Nodal connectivity for the FEM 36
3.3 Conceptual model of 1D flow analysis. 43
3.4 VapourT grid for 1D simulation 44
3.5 AIR3D grid for 1D simulation 44
3.6 Pressure drawdown versus volumetric flowrate for one-dimensional incompressible and compressible flow analysis 46

3.7 Boundary conditions and dimensions for the FDM (AIR3D) and FEM (VapourT) example problem 48
3.8 Initial grid for VapourT simulations. 50
3.9 Initial grid for AIR3D simulations. 50
3.10 Pressure drawdown distribution for VapourT vertical well simulation 51
3.11 Pressure drawdown distribution for VapourT vertical well simulation 51
3.12 Pressure drawdown distribution for AIR3D vertical well simulation . 51
3.13 Illustration of full, half and quarter grids in AIR3D. 53
3.14 Pressure drawdown at vertical extraction well elevation 56
3.15 Pressure drawdown at 0.5 m depth 57
3.16 Comparison with analytical solution at vertical extraction well elevation 58

4.1 Site map at Strachan 63
4.2 Field pressure drawdown distributions at Strachan 68
4.3 Conceptual model at Strachan 70
4.4 Schematic illustration of the boundary conditions for horizontal well AIR3D simulations. 71
4.5 Model and field well pressures within the 30 m horizontal well at Strachan. 72
4.6 AIR3D 3D horizontal well model drawdowns vs. field drawdowns at Strachan 76
4.7 VapourT 2D axisymmetric vertical well model drawdowns vs. field drawdowns at Strachan. 79
4.8 VapourT 2D cartesian coordinates horizontal well model drawdowns vs. field drawdowns at Strachan. 80
4.9 Site map at Site B 83
4.10 Field pressure drawdown distributions at Site B 86
4.11 AIR3D 3D horizontal well model drawdowns vs. field drawdowns at Site B 90
4.12 Model well pressures within the 60 m horizontal well at Site B. . . . 92

5.1 Location of cross-sections for sensitivity analysis figures. 97
5.2 Pressure distributions for Base Case A 98
5.3 Volume of porous media influenced, Case A 102
5.4 Volumetric flowrates per unit area for Base Case A 104
5.5 Travel times to well for different particle locations, Case A and B . . 105
5.6 Varying the sand permeability, Case A 106
5.7 Varying the till permeability, Case A 108
5.8 Varying the number of horizontal extraction wells, Case A 111
5.9 0.01 and 0.1 %atm pressure contours for two horizontal wells at different distances apart, Case A 111
5.10 Volumetric flowrate per unit area, Case A 112
5.11 Varying the number of vertical extraction wells, Case A 114
5.12 Zone of capture of V^*_5 for different well combinations, Case A 115
5.13 Varying well placement, Case A 116
5.14 Varying well properties, Case A 118
5.15 Varying model design, Case A 119
5.16 Pressure distributions for Base Case B 121
5.17 Volume of porous media influenced, Case B 124
5.18 Volumetric flowrates per unit area for Base Case B 126
5.19 Varying the till permeability, Case B 128
5.20 Pressure distribution for adding a cover and Base Case B 128
5.21 Varying the well location, Case B 129
5.22 Varying the well type and number, Case B 131
5.23 Volumetric flowrate per unit area, Case B 132
5.24 Varying the well length, Case B 133
5.25 Varying the well permeability, Case B 135
5.26 2D cartesian coordinates, Case B 135
5.27 Comparison of the two Base Cases 137

A.1 AIR3D quarter grid ($a3_q$) 146

A.2 AIR3D full initial grid (a3) 146
A.3 VapourT initial grid, $r_i = 0$ m (v1) 147
A.4 AIR3D full fine grid (a4) 148
A.5 VapourT initial grid, $r_i = 0.1$ m (v1$_r$) 149
A.6 VapourT fine grid, $r_i = 0$ m (v2) 150
A.7 VapourT fine grid, $r_i = 0.1$ m (v2$_r$) 151

List of Tables

2.1 Equilibrium partitioning coefficients and other properties of selected hydrocarbons at 25°C 19

3.1 Parameters used for pipe permeability analysis. 40
3.2 Parameters used for 1D flow analysis. 45
3.3 Volumetric flowrates for 1D flow analysis. 47
3.4 VapourT simulations 54
3.5 AIR3D simulations 54

4.1 Permeabilities selected for modelling simulations at Strachan 65
4.2 Input parameters required for AIR3D modelling at Strachan. 74
4.3 Input permeabilities, pressure drawdowns and extraction rates for different AIR3D and VapourT simulations for Strachan 75
4.4 Till permeabilities selected for modelling simulations at Site B. 85
4.5 Input parameters required for AIR3D modelling at Site B. 89
4.6 Input permeabilities, pressure drawdowns and extraction rates for different AIR3D simulations for Site B 89

5.1 Parameters for Base Case A 95
5.2 Parameters for Base Case B 95
5.3 Results from sensitivity analyses for varying different geological and grid parameters, Case A 99
5.4 Results from sensitivity analyses for varying well properties, Case A . 100
5.5 Results from sensitivity analyses for Case B 122

Notation

General

A	area	$[L^2]$
d	diameter	$[L]$
g	gravitational constant	$[L/T^2]$
k	permeability	$[L^2]$
L	length	$[L]$
M_w	effective molecular weight	$[M/mol]$
P	gas pressure	$[M/LT^2]$
q	specific discharge/volumetric flux	$[L/T]$
Q	volumetric flowrate	$[L^3/T]$
r	horizontal radial coordinate direction	$[L]$
R	Universal Gas Constant	$[ML^2/molT^2K]$
T	temperature	$[K]$
t	time	$[T]$
v	velocity	$[L/T]$
V	volume	$[L^3]$
x, y	horizontal Cartesian coordinate direction	$[L]$
z	vertical coordinate direction	$[L]$
μ	kinematic viscosity	$[M/LT]$
ρ	fluid/air density	$[M/L^3]$
θ	air-filled porosity	$[-]$

Air Flow and Transport

C_g	equilibrium gas/vapour phase concentration	$[M/L^3]$
C_w	equilibrium water concentration	$[M/L^3]$
f	friction factor	$[-]$
h	aqueous hydraulic head	$[L]$
h^*	equivalent head potential	$[L]$
H	Henry's Law Constant	$[-]$
k^i	intrinsic permeability	$[L^2]$
k^*	relative permeability	$[-]$
k	effective permeability	$[L^2]$
k_l	laminar flow well permeability	$[L^2]$
k_t	turbulent flow well permeability	$[L^2]$
K	hydraulic conductivity	$[L/T]$
P_{atm}	atmospheric pressure	$[M/LT^2]$
P_D	pressure drawdown	$[M/LT^2]$
P_L	pressure loss	$[M/LT^2]$
P_o	initial gas pressure	$[M/LT^2]$
ΔP	change in gas pressure	$[M/LT^2]$
Q_{air}	AIR3D extraction rate	$[L^3/T]$
Q_{ex}	volumetric extraction rate	$[L^3/T]$
Q_{mod}	MODFLOW extraction rate	$[L^3/T]$
R_{ed}	Reynolds number	$[-]$
R_r	Relative Roughness	$[-]$

Air Flow and Transport (Continued)

S_g	pneumatic specific storage	$[1/L]$
S_s	aqueous specific storage	$[1/L]$
S_{2D}	VapourT specific storage	$[1/L]$
S_{3D}	Air3D specific storage	$[T]$
S	aqueous solubility	$[M/L^3]$
V_p	vapour pressure	$[M/LT^2]$
V_t^*	volume of porous media influenced after t days	$[L^3]$
W	sink term	$[M^2/L^2T^4]$
X_i	mole fraction of constituent i	$[-]$
β	fluid compressibility	$[LT^2/M]$
ϵ	average pipe roughness	$[L]$
γ	porous media compressibility	$[LT^2/M]$
ν	dynamic viscosity	$[L^2/T]$
Φ	fluid potential	$[L^2/T^2]$
ρ_{NAPL}	NAPL density	$[M/L^3]$
ρ_o	uncontaminated air density	$[M/L^3]$
ρ_{well}	air density in extraction well	$[M/L^3]$
σ	change of variable	$[M^2/L^2T^4]$

Numerical Model

E	element number (FEM)	$[-]$
$\{F\}$	flux vector	$[L/T]$
$[H]$	conductance matrix	$[L^2/T]$
$\{h\}$	head vector	$[L]$
i	node	$[-]$
ne	number of elements (FEM)	$[-]$
nn	number of nodes (FEM)	$[-]$
nx	number of rows (FDM)	$[-]$
nx	number of nodes in the horizontal direction (FEM)	$[-]$
ny	number of columns	$[-]$
nz	number of layers (FDM)	$[-]$
nz	number of nodes in the vertical direction (FEM)	$[-]$
r_{ex}	well radius	$[L]$
Δt	time step	$[T]$
Δx, Δy	horizontal (column and row) grid discretization	$[L]$
Δz	vertical (layer) grid discretization	$[L]$

3.4.2 Two-Dimensional Flow to a Single Vertical Well 47

3.5 Summary 59

4 Case Studies 60

4.1 Strachan 60

4.1.1 Geology and Hydrogeology 61

4.1.2 Contamination Characterization 62

4.1.3 Vertical and Horizontal Well Installation and Configuration . . 62

4.1.4 Previous Field Activities and Modelling Results 64

4.1.5 Numerical Model Set-up 67

4.1.6 AIR3D Horizontal Well Numerical Modelling Results 73

4.1.7 VapourT Numerical Modelling Results 78

4.2 Site B 81

4.2.1 Geology and Hydrogeology 81

4.2.2 Contamination 82

4.2.3 Vertical and Horizontal Well Installation and Configuration . . 82

4.2.4 Previous Field Activities and Modelling Results 84

4.2.5 Numerical Model Set-up 85

4.2.6 Numerical Modelling Results 88

5 Generic Sensitivity Analysis 93

5.1 Approach 93

5.2 Method of Presenting Results 96

5.3 Base Case A 97

5.4 Sensitivity Analysis for Case A 103

5.4.1 Permeability 105

5.4.2 Watertable Location 109

5.4.3 Well Characteristics 109

5.4.4 Model Design 119

5.5 Base Case B 120

5.6 Sensitivity Analysis for Case B 125
5.6.1 Permeability 125
5.6.2 Watertable Location 127
5.6.3 Well Characteristics 129
5.6.4 2D Flow 136
5.7 Comparison of Case A to Case B 136
5.8 Summary 136

6 Conclusions **141**

A FDM and FEM Grid Discretization Figures **145**

References **152**

Chapter 1

Introduction

Contamination of groundwater and soil by volatile organic contaminants, such as petroleum products or chlorinated solvents, is an important environmental issue in Alberta, and elsewhere. Such contaminants, accidently released into the unsaturated zone as non-aqueous phase liquids (NAPL), may volatilize into the vapour phase, dissolve into soil water, partition onto soil solids, or remain in their immiscible phase (Figure 1.1). Once the contaminants have partitioned into the vapour phase, diffusive transport can rapidly transport contaminants throughout much of the unsaturated zone. Phase-partitioning processes commonly result in the contamination of underlying groundwater, rendering this essential resource unfit for human consumption for years.

1.1 Overview of Soil Vapour Extraction

Soil vapour extraction (SVE), also known as vacuum extraction, in-situ air stripping, or soil venting, is a method currently used to remove volatile organic compounds (VOC) from the unsaturated zone by pumping air out of horizontal or vertical extraction wells (Figures 1.2 and 1.3). The removal of air creates pressure gradients in the subsurface, inducing air to flow towards the well. The continual removal of air from the subsurface causes VOCs stored in other phases to partition to the gas phase. Subsequently, these contaminants are removed from the subsurface with the

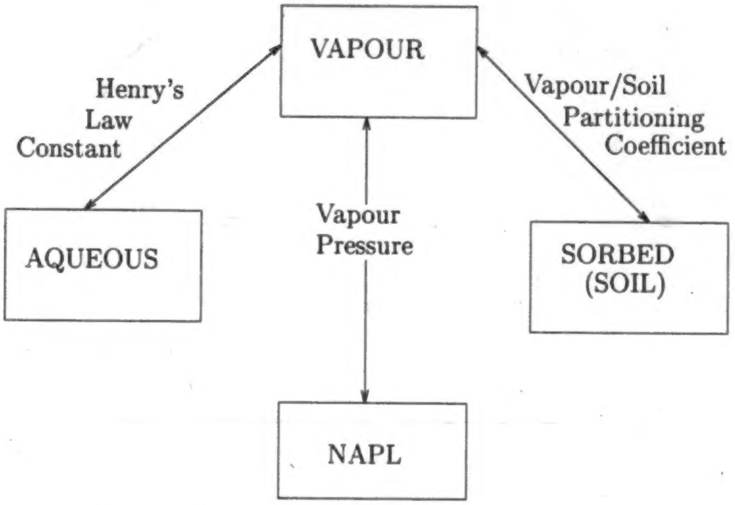
VAPOUR
Henry's Law Constant
Vapour/Soil Partitioning Coefficient
Vapour Pressure
AQUEOUS
SORBED (SOIL)
NAPL

Figure 1.1: NAPL phases and associated partitioning coefficients

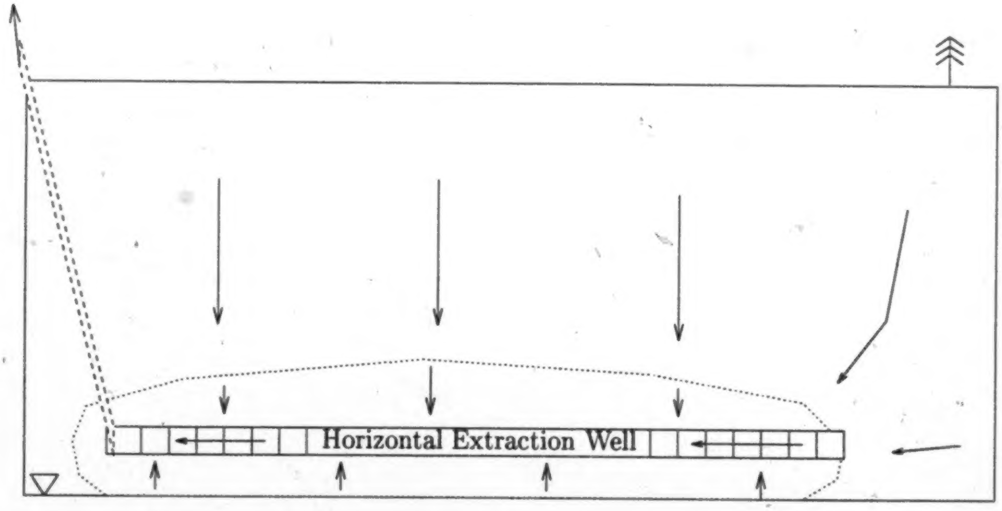
Horizontal Extraction Well

Figure 1.2: Conceptual model of a horizontal well SVE system.

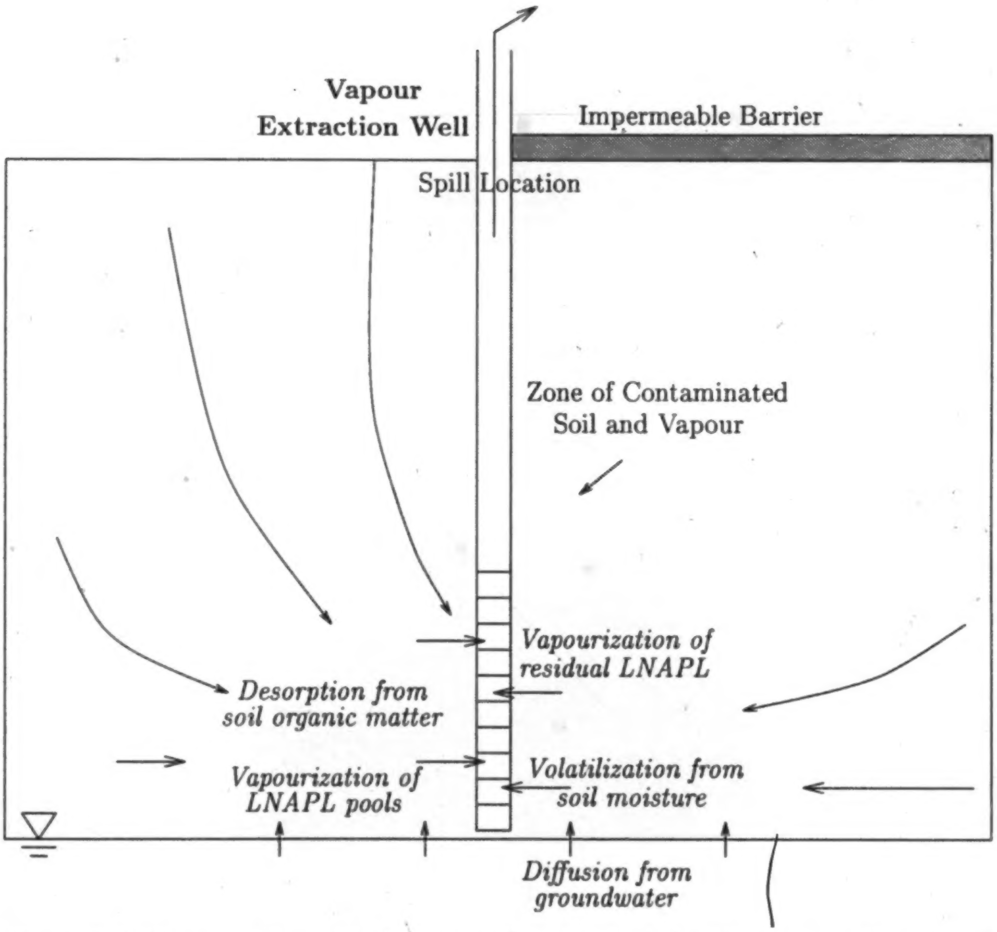
Vapour
Extraction Well
Impermeable Barrier
Spill Location
Zone of Contaminated
Soil and Vapour
Vapourization of
residual LNAPL
Desorption from
soil organic matter
Vapourization of
LNAPL pools
Volatilization from
soil moisture
Diffusion from
groundwater

Figure 1.3: Conceptual model of sources of contaminated soil vapour and a vertical soil vapour extraction system.

extracted air. SVE also has the effect of replenishing subsurface oxygen which may enhance in-situ biodegradation of the contaminant (Gilmour, 1996). Depending on the emission regulations applicable to the site, contaminated air may be expelled to the atmosphere or treated. Common treatment processes include sorption on to activated carbon, catalytic conversion, incineration and enhanced biodegradation (Johnson *et al.*, 1990a; Goldfarb *et al.*, 1994).

SVE is an alternative remediation technique to excavation and disposal or incineration. Other remediation techniques that are similar to SVE include: bioventing, where microorganisms in the subsurface degrade the hydrocarbons, enhanced by the addition of oxygen and nutrients delivered by SVE wells; air sparging, in which air is injected in the saturated zone and soil vapour is removed from the unsaturated zone; multi-phase extraction, where free-phase product, air and water are removed simultaneously; and soil piles, in which contaminated soil is piled on the surface and soil vapour is removed with an extraction system.

The use of horizontal wells instead of vertical wells in a SVE system has recently been proposed and may have a number of advantages. These include the ability to minimize surface infrastructure, to extract from beneath surface structures, to readily provide a boundary cut-off, and to have elongated containment zones that mimic plume shapes (Massmann and Madden, 1994; Armstrong *et al.*, 1995; Mast, 1996). Possible disadvantages of horizontal well SVE systems are the inability to access several units of horizontal stratification and difficulties associated with installation in deep unsaturated zones.

1.2 Study Objectives

The objectives of this research were to:

- develop a conceptual model of flow of air to horizontal wells during SVE;
- compare incompressible and compressible air flow predictions;

- analyze the performance of vertical and horizontal SVE systems at two field sites; and
- determine which geological, hydrogeologic, and well parameters, and model design exert the greatest influence over predicted air flow solutions.

These objectives were accomplished by modifying existing numerical models to simulate and analyze the performance of SVE, using available data from two gas plants in Western Canada. The two numerical models utilized in this study were:

1. VapourT (Mendoza, 1992), a two-dimensional finite-element model (FEM) that simulates the flow of incompressible gas and/or transport of vapour in the unsaturated zone; and
2. AIR3D (Joss and Baehr, 1995), a three-dimensional finite-difference model (FDM) that simulates compressible air flow in the unsaturated zone.

Because results from a FEM and FDM were compared, it was necessary to analyze how differences in well-flux calculations between the two model formulations affect the numerical model solutions.

Using data available on the geological conditions and field pressure observations at the two sites, the two numerical models were used to simulate air flow behavior during SVE with horizontal wells. A sensitivity analysis was performed to assess the data requirements for numerical modelling and to delineate the bounds of applicability for horizontal wells. The analysis examined geological and hydrogeological parameters, well characteristics and grid design to determine which parameters exerted the greatest control over the air flow solution. The simulations were evaluated in terms of comparing pressure distributions, travel times and flowpaths to the extraction well, and the volume of soil influenced by extraction between different simulations. The results of the horizontal SVE system were compared to that of vertical SVE systems installed at the sites.

1.3 Literature Review

Subsurface geological properties and flow parameters must be quantified to design an effective and efficient soil vapour extraction system. Basic concepts of air flow in the unsaturated zone and soil vapour extraction are outlined in this section. A review of horizontal environmental wells is included, followed by a summary of a number of sites that have employed horizontal wells for SVE. Finally, a brief examination of models that describe flow of air during SVE is provided.

A vital parameter controlling air flow is the soil permeability. Soil permeability, which is a function of the intrinsic permeability and the moisture content, can change during air extraction, although the two processes that typically cause the alteration may counteract one another (Beckett and Huntley, 1994; DiGiulio, 1996). The incoming atmospheric air may be drier than the soil air, which can lead to dehydration of the unsaturated zone. Beckett and Huntley (1994) conclude that this process is likely to be negligible. Watertable upwelling, the opposing process which increases the moisture content in the unsaturated zone, is a result of decreased capillary pressure during SVE (Beckett and Huntley, 1994).

Massmann (1989) and Massmann and Madden (1994) present three methods for estimating soil air permeability: 1) based on known hydraulic conductivity values; 2) based on grain-size parameters; and 3) using curve fitting from vertical and horizontal SVE tests. For the latter, the Theis and Hantush aquifer test methods were used to analyze pressure versus time observations from SVE tests. Confined and leaky conditions, for homogeneous and isotropic porous media, were considered. Horizontal wells were accommodated by assuming two-dimensional flow, neglecting any end effects, and using image wells to represent the boundary conditions (Massmann and Madden, 1994). These analyses were applied to a landfill site in Alaska (Massmann and Madden, 1994). A 12 m horizontal well was installed in a trench at a depth of 2.4 m and a vertical well was screened to the watertable at a depth of 8.5 m. The average unsaturated hydraulic conductivity was estimated to be 1.7×10^{-4} m/s; however, the horizontal well test yielded conductivities approximately twice those of the vertical well test. The authors note that a vertical test tends to represent a conductivity over a vertical section compared to a horizontal test which tends to represent the horizontal section. Thus, these small differences were attributed to varying degrees of leakage through surface asphalt or stratification for the two configurations.

The flow of air through clay during SVE was investigated by Gibson *et al.* (1993). Field studies of SVE, conducted over 8 months, indicated that the radius of influence was approximately 6 m from the vertical well and that the clay permeability was between 2×10^{-11} and 8×10^{-12} m^2. Laboratory studies showed that porosity enhancement and fracturing can occur when organic solvents are introduced to clay, thereby increasing the air permeability. The results of this work show that clay can have satisfactory air flow for SVE, particularly with the increased permeability due to organic solvent reactions.

Johnson *et al.* (1990b) present an estimation method to determine the time necessary to reach steady-state flow conditions. Their analysis shows that typical times are between 1 day to 1 week. This result is somewhat at odds with observations reported by Massmann (1989), DePaoli *et al.* (1991), Clarke *et al.* (1992), Komex (1994c), Massmann and Maddan (1994), and Kremesec (1995). These other workers have all found pressure equilibrium times on the order of hours during SVE.

An impermeable cover at the ground surface may reduce the amount of short circuiting and increase the volume of the subsurface that will be flushed by uncontaminated air, as shown in Figure 1.3. Such barriers to flow might include materials existing at the site, such as asphalt, concrete or buildings; or engineered materials constructed with the SVE system, such as high density polyethylene liner. The use of a surface barrier to encourage horizontal flow of air in the unsaturated zone has been discussed at length by Gannon *et al.* (1989), DePaoli *et al.* (1991), Goldfarb *et al.* (1994) and Mohr and Merz (1995).

Mohr and Merz (1995) simulated the measured air flow at 21 sites with asphalt paving. They concluded that the best match between field and model pressures occurred when the surface boundary condition had no barrier to flow. The only sites which had a good fit when a barrier was simulated at the surface were sites with a low-permeability geological layer at the ground surface. Mohr and Merz (1995) concluded that asphalt was a poor barrier to air flow at the ground surface and that surface geology, rather than engineered barriers, may have greater influence over the amount of vertical leakage.

Beckett and Huntley (1994) state that vertical leakage can readily occur through cracks and seams in asphalt, concrete, gravel-filled utility trenches, and tank cavities. Similar to the findings of Mohr and Merz (1995) regarding surface barriers, Beckett and Huntley (1994) also concluded that simulations of SVE using a confined model yield inconsistent results. They argue that from a practical standpoint, accounting for vertical leakage greatly increased the estimates of cleanup time compared to predictions from models with impermeable boundaries.

Even though vertical wells have traditionally been installed for SVE systems, the oil, river crossing and utility industries have been drilling horizontal holes for the past 70 years. It is only recently that horizontal wells have been applied to the remediation of contaminated soils and groundwater (Morgan, 1992; Wilson and Kaback, 1993). The first directionally drilled environmental horizontal well was installed in 1988 at the Savannah River Site (Kaback *et al.*, 1991; Wilson and Kaback, 1993).

A survey completed by Wilson and Kaback (1993) found that over 100 directionally drilled environmental horizontal wells had been installed in the United States up to 1993. Of these, one-quarter were utilized for groundwater remediation, one-quarter for SVE and one-half for "other" environmental purposes. Over 80% of these wells were installed by small to medium drilling rigs to depths of less than 8 m. The SVE horizontal wells were typically 20 to 130 m long, with an inside diameter of 0.05 to 0.15 m (2 to 6 in). They had been installed in geologic deposits ranging from sand and sandstone to clay. One of the primary reasons reported for installing horizontal SVE wells was to avoid surface disturbance.

An important consideration in determining whether horizontal or vertical wells should be installed at a site is the cost of installing, operating and maintaining the

SVE system. The cost of installation is highly dependent on the subsurface geology, drilling method, well materials utilized and the guidance system used to track to drilling progress, as well the number, length and depth of the well(s) (Wilson and Kaback, 1993; Wilson and Losonsky, 1995).

The costs associated with directionally drilled horizontal and vertical environmental wells were compared by Wilson and Losonsky (1995). Their example considered five vertical wells with 3 m screens versus one directionally drilled horizontal well with a 60 m screen. Although the installation costs for both scenarios were similar, approximately \$115 000, the difference in yearly operational costs was substantial: \$54 000 for the vertical wells compared to only \$17 000 for the horizontal well. A ten-year estimate of the cost of installing and operating 5 vertical wells was almost \$650 000 compared to only \$280 000 for the single horizontal well. Wilson and Losonsky (1995) report that a directionally drilled horizontal environmental well costs between \$50 to \$300/ft to install. This is within the range given by Hardy (1997).

The method of installing horizontal wells can vary greatly from that of vertical wells. Details regarding installation methods and materials used can be found in Dickinson *et al.* (1986), Karlsson and Bitto (1990), Kaback *et al.* (1991), Morgan (1992), Wilson and Kaback (1993), and Russell (1996).

At a site described by Kremesec *et al.* (1995), horizontal wells for a SVE system were chosen over vertical wells because of the decreased surface disturbance. A 100 m long horizontal well was installed in medium sands with an estimated conductivity of 3.2×10^{-4} m/s at a depth of 2.5 m. AIR3D (Joss and Baehr, 1995) was used to confirm these conductivity values. The pressure in the 0.1 m diameter well was observed to decrease from a pressure drawdown of 6.4 %atm at the inlet to 0.8 %atm at the end of the 100 m long well. It was suggested that one method to alleviate pressure losses in long horizontal wells would be to increase the pipe diameter (Bass, 1994; Battaglia and Morgan, 1994; Kremesec *et al.*, 1995). The flow was also observed to be non-uniform, with only 16% of the flow entering the distal half of the horizontal well when the extraction flowrate was 0.3 m^3/s. These observations were successfully simulated using AIR3D. Model results showed a shorter horizontal well exhibiting much lower pressure loss along the well. Kremesec *et al.* (1995) concluded that the choice of whether to use horizontal or vertical wells should depend primarily on the surface accessibility issue.

A well documented study of SVE in conjunction with a bioremediation and heat injection system installed to remediate hydrocarbons at the Hill AFB in Utah was completed by DePaoli *et al.* (1991). The subsurface geology at the site consisted of sand interbedded with clay lenses. Hydrocarbon contamination was found to a depth of 15 m. Six 0.1 m (4 in) horizontal wells were installed in an excavated trench at a depth of 6 m with a screened length of 10 m. Concrete was poured above the vents at ground surface to prevent short circuiting. A surface barrier was installed over half the site by placing two polyethylene sheets at ground surface and covering the sheets with a layer of excavated soil. Using the observed pressures surrounding the vent, the two-dimensional radially axisymmetric analytic model FEMAIR was used to estimate a permeability range of 3×10^{-12} to 6×10^{-11} m^2. The modelling results showed that surface barriers assist in creating a larger zone of influence. However, the field observations in the area with no surface barrier had pressure distributions similar to areas with the surface cover, suggesting that the barriers are ineffective barriers to flow. As the SVE system operated, the chemical concentration in the extracted air decreased and composition become less volatile. In zones of higher air flow, higher mass removal of the hydrocarbons was observed; however, the overall removal efficiency calculations for the system was strongly dependent on characterization of the initial hydrocarbon distribution.

Horizontal SVE wells have been used in conjunction with a number of other remediation techniques. For instance, Downs (1996), Wade *et al* (1996), and Basinet and Wollenberg (1997) describe combined air sparging/SVE systems. Additionally, many researchers discuss the combination of bioventing with SVE (Joss and Baehr, 1993; Komex, 1994d; Kremesec *et al.*, 1995; Mohr and Merz, 1995; Rathfelder *et al.*, 1995; Gilmour, 1996; Hardy, 1997)

Kaback *et al.* (1991) describe the installation and use of horizontal wells at the Savannah River U.S Department of Energy Site in South Carolina to remediate contaminated soils and groundwater. Two horizontal wells were installed in sands and sandy clay at this site. A 90 m long well was located below the watertable at a depth of 50 m and a 60 m long well was installed at 20 m depth in the unsaturated zone. The lower well was used to inject air (sparging), while the upper well was used to extract air (SVE).

Johnson *et al.* (1990a) discuss many design, installation, and operational aspects that must be considered in SVE systems. They state that the three most significant factors affecting the efficiency of any soil venting operations are the vapour flowrate, the vapour flowpath relative to the contaminant distribution and the contaminant composition. A typical method of determining the effectiveness of a SVE system is to measure or estimate the radius of influence. Radius of influence, which is most suitable for axisymmetric flow to vertical wells, has a number of different definitions associated with it. It has most commonly been defined as the distance where a defined pressure is measured (Beckett and Huntley, 1994; Johnson and Ettinger, 1994). Literature values of the defined pressure range from 0.1 in (2.5×10^{-3} m) H_2O (Komex, 1994c), to no observed pressure drawdown (Clarke *et al.*, 1992; DiGiulio, 1996). Johnson and Ettinger (1994) outline three methods to estimate the radius of influence: 1) empirical methods based on previous studies; 2) graphical methods based on pressure drawdown versus distance; and 3) semi-analytical determination based on equations (Johnson *et al.*, 1990a).

A limitation to the above definitions of radius of influence is that there is no relevance to the time required for remediation. Consequently, SVE system designs based solely on the radius of influence tend to underpredict the time required for remediation and are only successfully in containing the contaminated vapours (Johnson and Ettinger, 1994). This problem is overcome with alternative definitions by Bass (1993), Beckett and Huntley (1994), Goldfarb *et al.* (1994), Johnson and Ettinger (1994) and Mohr and Merz (1995) in which the effective radius of influence is defined as the distance from the well where a certain flowrate is found. Commonly, this distance is where sufficient air flow exists to remediate the subsurface to acceptable levels within the allowable time. Beckett and Huntley (1994) and Johnson and Ettinger (1994) suggest that the necessary vapour flux be calculated from the time required for cleanup and the number of pore volumes required to remove the contaminant. The number of pore volumes required for a specified cleanup time depends on the geology, vapour velocities, contaminant properties and concentrations. Thus, this concept of pore volume includes the process of chemical partitioning and the removal of the contaminants, which may be limited by equilibrium partitioning.

Models for soil vapour extraction can be divided into three categories: 1) analytic models; 2) air flow models; and 3) transport models. Because this work focuses on the hydraulics of air flow, transport models are not discussed here. An overview of utilizing models to simulate flow and transport of vapours during SVE is presented by Jordan *et al.* (1995).

Many of the analytical models available for describing air flow during SVE are applicable only to a single vertical well (Massmann, 1989; Johnson *et al.*, 1990a; Marley *et al.*, 1990; McWhorter, 1990; Baehr and Hult, 1991; Shan and Falta, 1992; Bass, 1993; Beckett and Huntley, 1994; Mohr and Merz, 1995). HWELL, an analytical model describing steady-state or transient water flow to a horizontal well in a confined anisotropic aquifer was developed by Beljin and Losonsky (1992). Falta (1995) presents an analytical solution describing steady-state or transient gas flow to a single horizontal well or parallel, stacked pairs of horizontal wells in anisotropic, homogeneous porous media. End effects were ignored by assuming two-dimensional flow. Of particular note was that air flow to horizontal wells is highly influenced by anisotropic permeabilities.

Two numerical models that simulate transient or steady-state three-dimensional compressible air flow to horizontal wells are AIR3D (Joss and Baehr, 1995) and GAS3D (Sepehr and Samani, 1993). AIR3D has been coupled with an optimizing program by Welty *et al.* (1996) and Sawyer and Kamakoti (1998).

Chapter 2

Theory

2.1 Conceptual Model

The vadose zone can be defined as the zone of soil in the subsurface that possesses fluid(s) at negative pressures and air at atmospheric pressure. The pressure difference, caused by surface tension along the interface between the two fluids or the fluid and the air, is known as the capillary pressure. This phenomenon, along with the molecular attraction between the fluids and the soil particles, permits water and NAPL to remain in the pores spaces in the vadose zone. The capillary pressure between the fluids is a function of the pore geometry, the interfacial tension of the fluids, and the amount of each fluid present (Fetter, 1993).

As illustrated in Figure 2.1, the unsaturated zone is comprised of two zones: 1) the Pendular Zone, where water is at irreducible water saturation; and 2) the Funicular Zone, where the water content increases from the irreducible saturation to about 100% water saturation (Freeze and Cherry, 1979; Abdul, 1988; Fetter, 1993). The irreducible water content varies depending on the soil texture, ranging from 10% of the porosity for sands to approximately 40% for clays. The capillary fringe is defined as the porous media below the Funicular Zone where the soil is close to 100% saturated but still exhibits negative water pressure (Abdul, 1988). The saturated zone includes all porous media below the Funicular Zone where the water saturation is close to 100% (Abdul, 1988). The definitions of the vadose zone and unsaturated

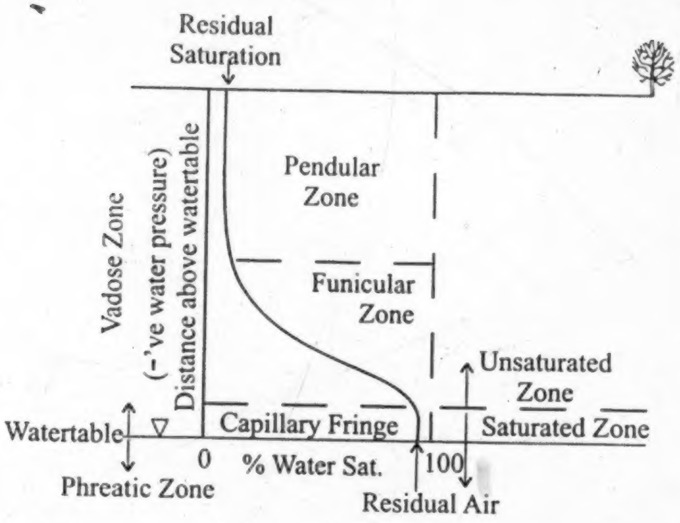
Residual Saturation
Vadose Zone
(-'ve water pressure)
Distance above watertable
Pendular Zone
Funicular Zone
Unsaturated Zone
Capillary Fringe
Saturated Zone
Watertable
Phreatic Zone
0
% Water Sat.
100
Residual Air

Figure 2.1: Conceptual model of the unsaturated and saturated zones. (modified from Abdul (1988))

zone differ in that the vadose zone is defined to include all porous media from the ground surface to the bottom of the capillary fringe, with all water in the porous medium exhibiting negative pressures, while the unsaturated zone only extends to the top of the capillary fringe, with all water saturations being less than 100% (Fetter, 1993; Freeze and Cherry, 1979). In examining air flow, the unsaturated zone is the zone of interest because it contains porous media with an appreciable air content.

The height of the capillary fringe depends on the largest pore diameter of the soil, the interfacial tension between the two fluids and the contact angle between the two fluids (Fetter, 1994). Experimental observations in unconsolidated geologic material with a porosity of 41% yielded capillary fringe heights of between 2.5 cm for a fine gravel with a grain size of 2 to 5 mm to greater than 2 m for a fine silt with grain sizes of between 0.02 to 0.05 mm (Fetter, 1994). In the unsaturated zone, the water phase is usually the wetting phase (i.e., the contact angle is less than 90°), meaning it has a tendency to coat the soil grains and occupy the smaller pore throats, while the air is normally the non-wetting phase and tends to occupy the pore voids. In a three-phase system with air, water and oil, the oil is generally non-wetting with respect to the water and wetting with respect to the air. Thus, water tends to coat the soil grains and oil exists between the water and air (Fetter, 1993). Even in the Pendular Zone, with only residual moisture content remaining, water will tend to form a fine layer on the soil grains (Fetter, 1994).

LNAPL released into the unsaturated zone migrates downwards and laterally due to gravity and capillary forces, through preferred flowpaths in the vadose zone. Lateral movement may arise due to the LNAPL pressures being insufficient to displace the pore water in areas of greater saturation. As the LNAPL moves downwards it displaces water present in the pore spaces. Residual LNAPL remains immobile in the vadose zone due to capillary forces. If the free phase LNAPL reaches the saturated zone, a capillary oil fringe and an oil pool under tension may develop on the capillary fringe and water in the capillary fringe will be replaced with LNAPL. If enough LNAPL is present, the LNAPL will begin to exhibit positive pressures and, if the porous media is very conductive, the water capillary fringe will disappear, the pool will rest on top of the watertable and may even displace water on top of the watertable. Such changes were observed by Abdul (1988) in a column experiment with laboratory sand and diesel.

Changing watertable elevations, due to seasonal watertable fluctuations or groundwater extraction, may result in the smearing of an oil pool lying near the watertable, as illustrated in Figure 2.2. As the watertable drops, the oil pool follows likewise, with LNAPL migrating into, and remaining in, the former saturated zone (Figure 2.2(b)). When the watertable rises (Figure 2.2(c)), some LNAPL may remain behind as residual and, depending on the velocities of the watertable rise and oil pool rise, mobile free phase LNAPL may still exist in the saturated zone (Fetter, 1993). The distributions of LNAPL and water above the watertable will be different for a dropping watertable, as drainage conditions exist, compared to a rising watertable, where imbibition conditions occur. The residual remaining in the saturated zone can dissolve into the aqueous phase, providing a source of groundwater contamination.

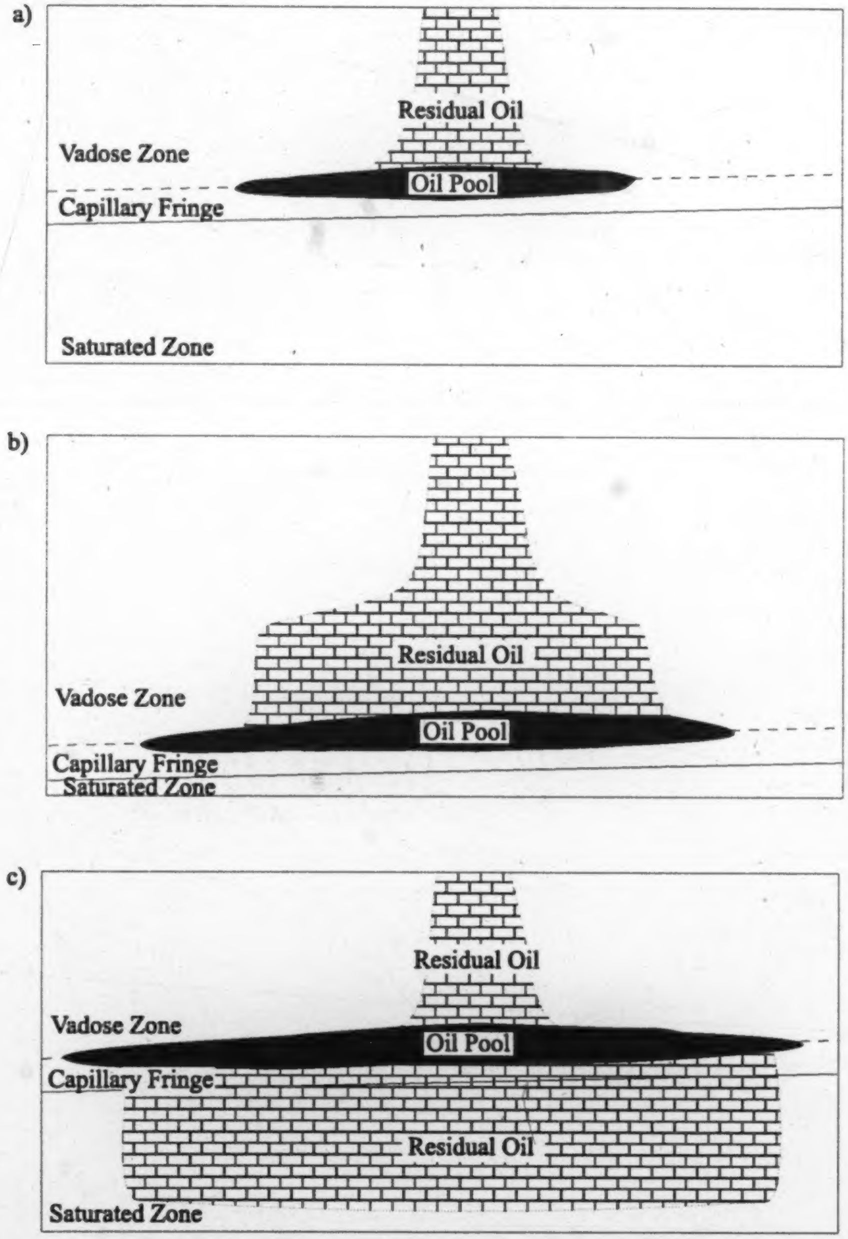
a)
Residual Oil
Vadose Zone
Oil Pool
Capillary Fringe
Saturated Zone
b)
Residual Oil
Vadose Zone
Oil Pool
Capillary Fringe
Saturated Zone
c)
Residual Oil
Vadose Zone
Oil Pool
Capillary Fringe
Residual Oil
Saturated Zone

Figure 2.2: Conceptual model of oil and water distributions during watertable fluctuations: (a) initial conditions, (b) dropping watertable, and (c) rising watertable. (modified from Fetter, 1993)

The residual remaining in the vadose zone and any pools of LNAPL present provide a source of contaminated soil vapour as illustrated in Figure 1.3. Once the contaminant has partitioned into the vapour phase, diffusive transport may rapidly transport the contaminated vapour throughout the system. Generally air diffusion coefficients are on the order of 10^{-5} m^2/s, 4 to 5 orders of magnitude greater than aqueous diffusion coefficients (Mendoza *et al.*, 1996).

Groundwater can become contaminated through a number of different processes. Soil water in the vadose zone can become contaminated through partitioning from other phases into the water phase. During infiltration and watertable fluctuations, the contaminated water from the vadose zone becomes incorporated into the groundwater. Other sources of groundwater contamination include dissolution of residual present in the saturated zone due to watertable fluctuations as explained previously, dissolution of a LNAPL pool in contact with the watertable and diffusion from the vapour phase into groundwater.

The equilibrium distribution of a constituent i between free phase NAPL to the vapour phase is related to the vapour pressure (V_{p_i}) of the constituent and it's mole fraction (X_i) by the ideal gas law and Raoult's law:

$$C_{g_i} = \frac{V_{p_i}}{RT} X_i \tag{2.1}$$

where C_{g_i} is the gas phase concentration, R is the universal gas constant and T is the fluid temperature (Baehr, 1987). The mole fraction can be found by dividing the number of moles of the particular compound by the total number of moles of the contaminant. Compounds with higher vapour pressures have a greater tendency to volatilize to the vapour phase than those with lower vapour pressures.

The equilibrium water-air partitioning coefficient, Henry's law constant H, is defined as:

$$H = \frac{C_g}{C_w} \tag{2.2}$$

where C_w is the equilibrium water phase concentration (Fetter, 1993). H has the units of $(\frac{mol/m^3\ air}{mol/m^3\ water})$. Both Henry's law constant and the vapour pressure are highly temperature dependent. Chemicals with high H, such as nonaromatic compounds (e.g., cyclohexane, 1-hexene, n-hexane and n-octane), have a tendency to partition into the vapour phase compared to chemicals with low H, such as aromatic compounds (e.g., benzene, toluene, o-xylene and ethylbenzene), which prefer to partition into the water phase (Fetter, 1993). Therefore, chemicals that are more likely to be present in the vapour phase, and thus amenable to SVE, are those with high Henry's law constant and vapour pressures. Table 2.1 presents Henry's law constants, vapour pressures and other chemical properties for selected organic chemicals, ranging from C_5 to C_{20} compounds. During SVE the compounds with high H and V_p that have a greater affinity for the vapour phase will be removed first, changing the NAPL composition. Later in time, once the initial lighter compounds have been preferentially removed, the mole fractions of heavier compounds increase and the concentrations of the heavier compounds also increase, and subsequently may be removed by the SVE later in time.

A SVE system typically consists of an extraction well installed in the unsaturated zone, connected to a blower which removes air from the subsurface, creating a pressure drawdown in the extraction well, as shown in Figure 1.3. The resulting pressure gradients force air in the unsaturated zone to flow towards the extraction well. In this way, extraction wells remove contaminated vapours from the unsaturated zone. This decreases the concentration of the vapour phase and creates concentration gradients between the vapour phase and the other phases. The configuration of the extraction well(s) and the subsurface geology will determine the air flowpath to the extraction well(s). Depending on local regulations and vapour concentrations, the released vapour may either be released to the atmosphere or passed through a treatment system.

2.2 Mathematical Equations for Flow

The continuity equation states that the amount of fluid entering a representative elemental volume (REV) minus the amount leaving the REV must equal the change

Compound	Formula	M_w (g/mol)	V_p (kPa)	C_g (mol/m^3)	H (-)	S (mol/m^3)	ρ (g/cm^3)
benzene	C_6H_6	78.1	1.27×10^1	5.13×10^0	2.24×10^{-1}	2.29×10^1	0.879
pentane	C_5H_{12}	72.2	6.84×10^1	2.76×10^1	4.88×10^1	5.65×10^{-1}	0.626
octane	C_8H_{18}	114.2	1.88×10^0	7.59×10^{-1}	1.27×10^2	5.97×10^{-3}	0.700
dodecane	$C_{12}H_{26}$	170.3	1.57×10^{-2}	6.43×10^{-3}	3.17×10^2	2.00×10^{-5}	0.766
eicosane	$C_{20}H_{42}$	282.6	2.18×10^{-7}	8.80×10^{-8}	8.00×10^1	1.10×10^{-9}	0.788

Table 2.1: Equilibrium partitioning coefficients and other properties of selected hydrocarbons at 25°C, where M_w is the molecular weight, V_p is the vapour pressure, C_g is the saturated concentration in air, H is Henry's law constant, S is the aqueous solubility and ρ is the NAPL density (Eastcott *et al.*, 1988)

in storage of the REV and is given by:

$$-\nabla(\rho q) = \frac{\partial(\theta\rho)}{\partial t} \tag{2.3}$$

where ρ is the fluid density, q is the specific discharge, and θ is the air-filled porosity (Freeze and Cherry, 1979). By assuming that the air-filled porosity is uniform and constant with time, (2.3) reduces to:

$$-\nabla(\rho q) = \theta\frac{\partial\rho}{\partial t} \tag{2.4}$$

For an ideal gas, the relationship between the density, ρ, and fluid pressure, P, is described by the ideal gas law:

$$\rho = \frac{M_w P}{RT} \tag{2.5}$$

where M_w is the effective molecular weight, R is the universal gas constant, and T is the temperature. For an isothermal system, the right hand side of the continuity equation (2.4) may be written in terms of pressure, rather than density, by substituting (2.5) into (2.4) and multiplying both sides by g to obtain:

$$-\nabla(\rho g q) = S_g\frac{\partial P}{\partial t} \tag{2.6}$$

The pneumatic specific storage term, S_g, is equal to:

$$S_g = \frac{\theta g M_w}{RT} = \rho g(\gamma + \theta\beta) \tag{2.7}$$

where γ is the porous media compressibility and β is the fluid compressibility (Freeze and Cherry, 1979; Massmann, 1989; Mendoza, 1992). The compressibility of the porous media can be assumed negligible compared to the compressibility of gas, therefore $S_g = \rho g\theta\beta$.

The specific discharge term, q, must be solved for in (2.6) and this is accomplished with Darcy's law. For SVE, the flow of air is primarily due to pressure gradients, therefore diffusional flow is considered negligible and not accounted for. Air flow due to barometric fluctuations, watertable fluctuations, infiltration, temperature gradients and wind gusts is neglected in this study.

Darcy's law for groundwater assumes that the velocity of water along the pore walls is equal to zero, and this flow is referred to as viscous or pressure flow. For the flow of gases, the velocity may be greater than that predicted by Darcy's law because the velocity along the pore walls may be nonzero. This slip flow phenomenon is a result of the mean-path of gas molecules being similar to common pore radii and is a function of pore radius and gas pressure (Massmann, 1989). For an average pore radius of 10^{-5} mm, the ratio of pressure flow to slip flow is approximately 0.3 compared to a ratio of 200 for a pore radius of 10^{-2} mm. Massmann (1989) concludes that for porous media in the unsaturated zone with a pore radius of that of sand and gravels or larger, viscous flow dominates over slip flow and therefore, for those materials, Darcy's law for the motion of groundwater flow can be assumed applicable. McWhorter (1990) also concludes that gas slippage is only significant during high extraction or injection rates in low permeability materials. Darcy's law also requires the flow of fluid to be laminar. Calculations by Beckett and Huntley (1994) demonstrate that air flow velocities outside the wellbore in very coarse-grained sands are still limited to the lower limit of turbulent flow.

Darcy's law states that the specific discharge of a fluid, q, is proportional to the gradient of the potential, $\nabla\Phi$, by:

$$q = -k\frac{\rho}{\mu}\nabla\Phi \tag{2.8}$$

where k is the permeability of the soil, μ is the fluid viscosity, and Φ is the fluid potential (Freeze and Cherry, 1979). For the system considered here, there may be two important components to the fluid potential: gravitational and pressure potential. The fluid potential for a compressible fluid is equal to (Hubbert, 1940; Massmann, 1989):

$$\Phi = gz + \int_{P_o}^{P} \frac{dP}{\rho} \tag{2.9}$$

where g is the gravitational acceleration, z is the elevation, and P_o is a reference gas pressure. Assuming that the system is isothermal and that the dominant potential is the pressure potential, and applying the ideal gas law, (2.9) becomes:

$$\Phi = \frac{RT}{M_w} \int_{P_o}^{P} \frac{dP}{P} \tag{2.10}$$

and the gradient of the fluid potential is:

$$\nabla\Phi = \frac{1}{\rho}\nabla P \tag{2.11}$$

Substituting (2.11) into (2.8) yields:

$$q = -\frac{k}{\mu}\nabla P \tag{2.12}$$

Finally, Darcy's law (2.12) is combined with the continuity equation (2.6) to describe the transient mass flow of gases in the unsaturated zone:

$$\nabla\left(k\frac{\rho g}{\mu}\nabla P\right) = S_g\frac{\partial P}{\partial t} \tag{2.13}$$

which is similar to the transient flow of groundwater:

$$\nabla(K\nabla h) = S_s\frac{\partial h}{\partial t} \tag{2.14}$$

where S_s is the aqueous specific storage, h is the aqueous head potential and K is the hydraulic conductivity (Freeze and Cherry, 1979). The main difference between the groundwater flow equation and gas flow equation is the density of the gas in (2.13) is dependent on the pressure of the gas, and therefore the gas flow equation is non-linear.

The effective permeability, k, is equal to the product of the intrinsic, k^i, and relative, k^*, permeabilities. The relative permeability, a function of the effective air-filled porosity and pore-size distribution index, is commonly calculated using the Brooks-Corey equation (Fetter, 1993). For both sites to be modelled in this study, it was assumed that the moisture conditions and air-filled porosity were under steady-state conditions at field capacity. Therefore, the relative permeability was equal to one, and the effective permeability is taken as being equal to the intrinsic permeability.

2.2.1 Incompressible Flow

The transient mass flow equation (2.13) is linear if the dependence of density on pressure is neglected. Assuming that density of the fluid is the initial gas density, ρ_o, then (2.13) becomes:

$$\nabla(k\frac{\rho_o g}{\mu}\nabla P) = S_g\frac{\partial P}{\partial t} \tag{2.15}$$

Since (2.15) is linear, it can be solved with existing groundwater models. An analytical solution to (2.13) was developed by Kidder (1957), assuming one-dimensional flow in a homogeneous system. The results showed differences between the exact and a linear approximate solution of less than 1% for drawdowns under 20 %atm, increasing to close to 30% when the drawdown was increased to 80 %atm. Massmann (1989) recommends a drawdown of 50 %atm as the upper limit to apply groundwater flow equations to describe air flow. Most SVE systems drawdowns are less than 20 %atm, therefore (2.15) can be applied to solve for air flow during SVE in the unsaturated zone.

VapourT, a two-dimensional FEM, utilizes this method of modelling gas flow (Mendoza, 1992). Compressibility of the gas is still incorporated into the flow equation through S_g, as long as transient flow is modelled. VapourT simulates gas flow in terms of heads, with:

$$h^* = \frac{P}{\rho_o g} + z \tag{2.16}$$

where h^* is the equivalent head of the gas mixture. If elevation potential is assumed negligible compared to the pressure potential, then $z = 0$. By substituting pressures with heads, (2.15) becomes:

$$\nabla\left(k\frac{\rho_o g}{\mu}\nabla h^*\right) = S_{2D}\frac{\partial h^*}{\partial t} \tag{2.17}$$

where $S_{2D} = (\theta\rho_o g\beta)$.

In two-dimensional cartesian coordinates, the gas flow equation is:

$$\frac{\partial}{\partial x}\left[k^* k^i_{xx}\frac{\rho_o g}{\mu}\frac{\partial h^*}{\partial x}\right] + \frac{\partial}{\partial z}\left[k^* k^i_{zz}\frac{\rho_o g}{\mu}\frac{\partial h^*}{\partial z}\right] + Q = S_{2D}\frac{\partial h^*}{\partial t} \tag{2.18}$$

where k^* is the relative permeability, k^i_{xx} and k^i_{zz} are the intrinsic permeabilities, assuming that the principle directions of permeability are aligned with the coordinate axes, and Q is the source term (Mendoza, 1992).

Alternatively, (2.18) can be expressed in two-dimensional axisymmetric coordinates as:

$$\frac{1}{r}\frac{\partial}{\partial r}\left[rk^*k^i_{rr}\frac{\rho_o g}{\mu}\frac{\partial h^*}{\partial r}\right]+\frac{1}{r}\frac{\partial}{\partial z}\left[rk^*k^i_{zz}\frac{\rho_o g}{\mu}\frac{\partial h^*}{\partial z}\right]+Q=S_{2D}\frac{\partial h^*}{\partial t} \tag{2.19}$$

where r is the radial coordinate direction.

2.2.2 Compressible Flow

Compressible flow is modelled by incorporating a varying density with change in pressure on the left hand side of (2.13). Substituting density with pressure using the ideal gas law in (2.13) yields (Joss and Baehr, 1995):

$$\nabla\left(k\frac{gM_wP}{\mu RT}\nabla P\right)=S_g\frac{\partial P}{\partial t} \tag{2.20}$$

This equation is linearized by using a change of variable where $\sigma = P^2$, and making two substitutions:

$$(P\nabla P)=\frac{1}{2}\nabla\sigma \tag{2.21}$$

and

$$\frac{\partial P}{\partial t}=\frac{1}{2P}\frac{\partial\sigma}{\partial t} \tag{2.22}$$

Substituting (2.21), (2.22) and σ into (2.20) yields:

$$\nabla\left(k\frac{gM_w}{\mu RT}\nabla\sigma\right)=\frac{S_g}{P}\frac{\partial\sigma}{\partial t} \tag{2.23}$$

Multiplying (2.23) by $(\mu RT/gM_w)$, (2.23) reduces to (Joss and Baehr, 1995):

$$\nabla(k\nabla\sigma)=S_{3D}\frac{\partial\sigma}{\partial t} \tag{2.24}$$

where $S_{3D} = \theta\mu/P$

A comparison between the exact solution to (2.13) and a non-linear approximate solution by Kidder (1957) yielded smaller differences than with the linear approximation, with differences less than 1% for pressure drawdowns less than 20 %atm and less than 5% for pressure drawdowns of 80 %atm (Massmann, 1989). To apply the groundwater flow model, such as MODFLOW (McDonald and Harbaugh, 1988), to air flow, h in (2.14) is replaced with P^2.

AIR3D (Joss and Baehr, 1995) uses MODFLOW (McDonald and Harbaugh, 1988), a three-dimensional finite-difference groundwater flow model, to solve (2.24). In three-dimensional cartesian coordinates, with the coordinates aligned with the major axes of the permeability tensor, (2.24) is expressed as:

$$\frac{\partial}{\partial x}\left(k_{xx}\frac{\partial \sigma}{\partial x}\right) + \frac{\partial}{\partial y}\left(k_{yy}\frac{\partial \sigma}{\partial y}\right) + \frac{\partial}{\partial z}\left(k_{zz}\frac{\partial \sigma}{\partial z}\right) - W = S_{3D}\frac{\partial \sigma}{\partial t} \qquad (2.25)$$

where k_{xx}, k_{yy} and k_{zz} are the effective permeabilities, and W is the sink term.

2.3 Boundary Conditions

To solve a numerical model, appropriate boundary conditions must be specified. Either Type I or Type II boundary conditions are applied along domain boundaries in AIR3D and VapourT. Type I boundary conditions, also known as Dirichlet boundaries, are constrained pressure boundaries. Type II boundary conditions, also called Neumann boundaries, are specified flux boundaries.

For VapourT, both Type I and Type II boundary conditions can be specified. Type I is typically applied to the ground surface (i.e., P set to atmospheric pressure), to the extraction well nodes along a boundary representing a well, and may be used for the far lateral boundary (i.e., P set to atmospheric pressure). The extraction well can alternatively be specified as Type II boundary, where the flux is set to the volumetric extraction rate. Type II boundary conditions are also utilized to simulate no-flow or impermeable boundaries, such as at the watertable, far lateral boundaries or symmetry boundaries, by setting the flux to zero,.

AIR3D permits the user to apply Type I or Type II zero-flux boundary conditions. The default ground surface boundary is assumed to be constrained atmospheric pressure. This is accomplished by adding an additional layer, that is 20% the thickness of the layer below, with all cells set to atmospheric pressure. The watertable boundary is set to Type II zero-flux boundaries. In its original form, the far lateral boundaries were assigned Type I boundary conditions of atmospheric pressure. Modifications to AIR3D allowed Type II zero-flux boundaries to be specified at the lateral boundaries (i.e., far lateral boundaries and symmetry boundaries).

Cartesian coordinates (i.e., (2.18) or (2.25)) are are most suitable for horizontal well configurations, as illustrated in Figures 2.3 and 2.4, with plane A-A′ representing the two-dimensional cartesian coordinates planes simulated. For two-dimensional flow, the horizontal well is portrayed as being infinitely long in the y-direction, thus no effects from the end of the well are simulated. To save computer time and space, a symmetry boundary may be applied, as illustrated in Figures 2.3 and 2.4. This approach is taken for most of the simulations in this study.

The vertical wells are realistically simulated with axisymmetric coordinates simulating radial flow as illustrated in Figures 2.5 and 2.6 by applying (2.19). Alternatively, flow to a vertical well can be modelled in three-dimensions by applying (2.25). Again, to save computer space and time, a symmetry boundary may be applied as illustrated in Figures 2.5 and 2.6. Axisymmetric coordinates can only simulate one vertical well, therefore multiple vertical well systems must be simulated with a three-dimensional model.

2.4 End Effects

Under isotropic conditions, flow to a vertical well is axisymmetric. That is, at equal distances from the well, the magnitude of pressure and flowrate is identical. Unlike a vertical well, flow to a horizontal well is three-dimensional. The influence of the end effects with a horizontal well SVE system will depend on the geological conditions and the SVE design. Three-dimensional analyses are the most appropriate modelling approach, but horizontal wells may also be represented in two-dimensions. As shown in Figure 2.7(a), a short horizontal well may be represented by axisymmetric flow to a vertical well with a vertically short screened interval. Alternatively, a long horizontal well can be represented with two-dimensional flow in cartesian coordinates

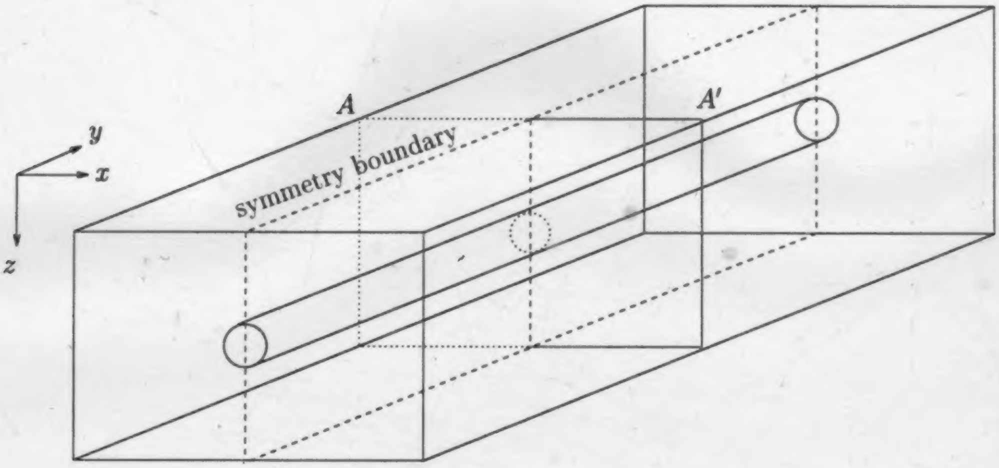
y
x
z
A
A′
symmetry boundary

Figure 2.3: Conceptual model of horizontal well in 2D cartesian coordinates.

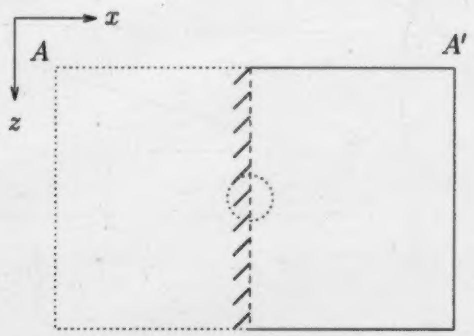

Symmetry Boundary

Figure 2.4: Cross-section A-A′ from Figure 2.3. Two-dimensional cartesian coordinates simulation with symmetry boundary.

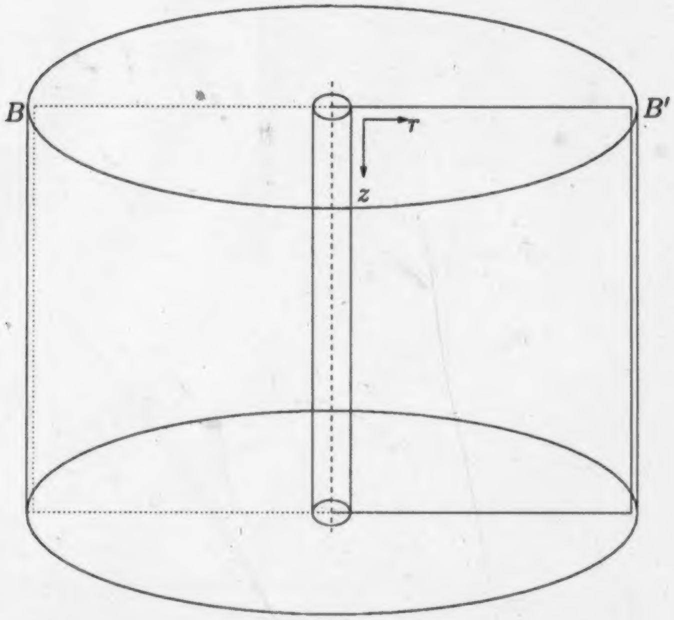

Figure 2.5: Conceptual model of vertical well with axisymmetric coordinates.

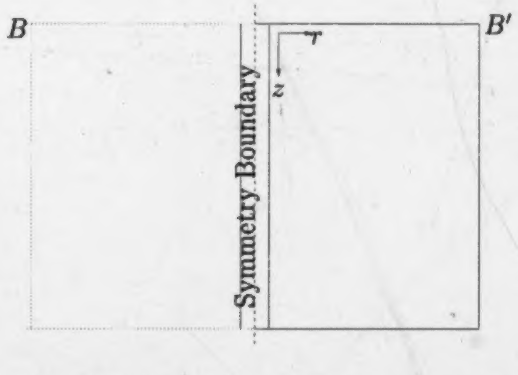
B
B′
r
z
Symmetry Boundary

Figure 2.6: Cross-section B-B′ from Figure 2.5. Two-dimensional axisymmetric coordinates simulation with symmetry boundary.

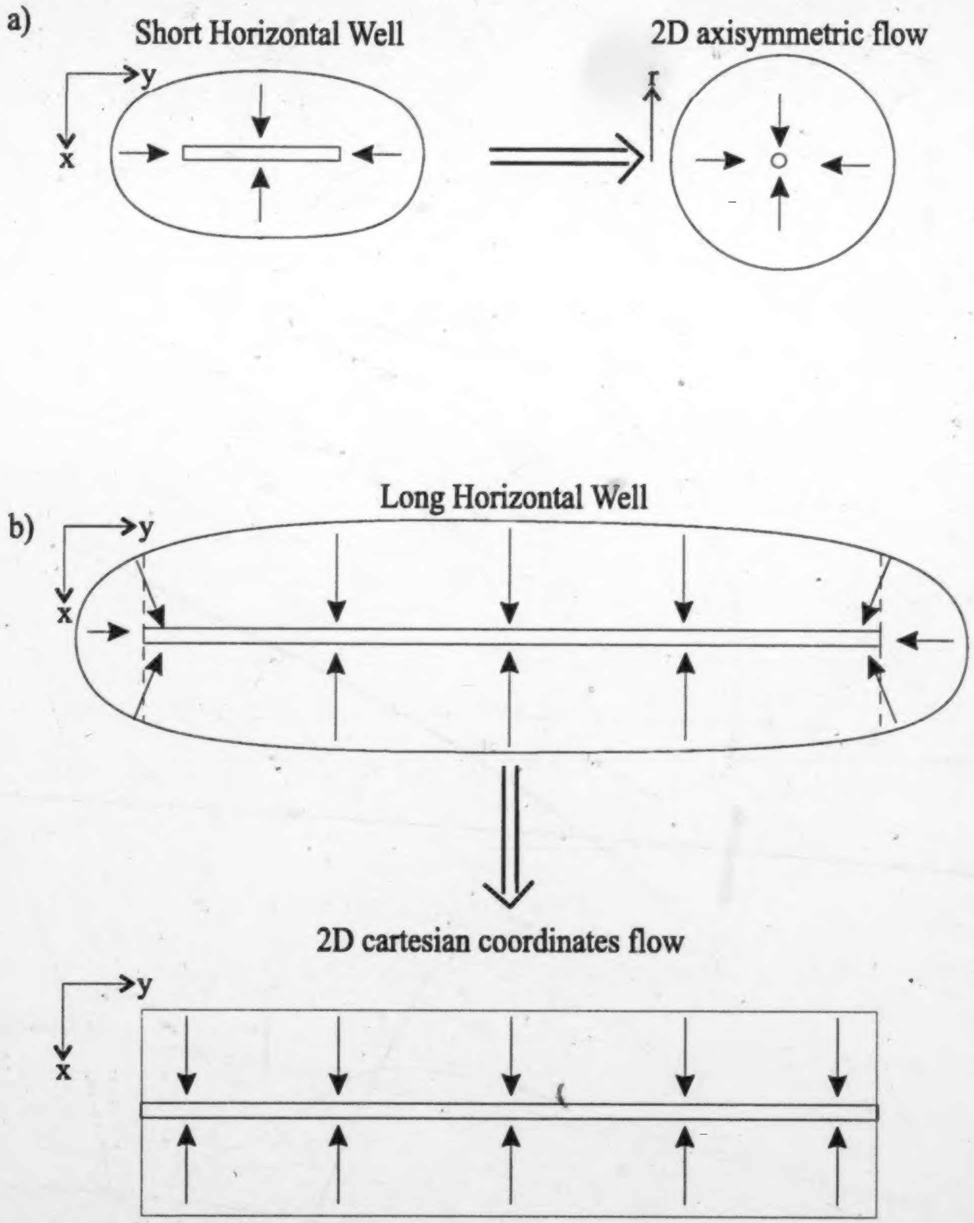
a)
Short Horizontal Well
y
x
2D axisymmetric flow
r
b)
Long Horizontal Well
y
x
2D cartesian coordinates flow
y
x

Figure 2.7: Representation of horizontal well in two-dimensions in layer cross-sections: (a) Short horizontal well with axisymmetric coordinates, and (b) Long horizontal well with two-dimensional cartesian coordinates.

by assuming flow to the ends of the well in the third dimension is negligible, as illustrated in Figure 2.7(b). These methods may be appropriate if the computer limitations and time require a two-dimensional model be utilized.

2.5 Flow Nets

A flow net is a two-dimensional, steady-state representation of potentials consisting of equipotential and flow lines, typically applied to groundwater systems (Freeze and Cherry, 1979). Flow net theory can be used to predict pressure distributions and changes in pressure distribution with changing permeability in pneumatic systems if incompressible conditions are assumed. An example applied to the flow of gas is presented by Falta (1995). The same assumptions and rules for flow net construction for groundwater flow in an aquifer can be applied to air flow in the unsaturated zone, with pressure potential replacing head potential and permeability replacing hydraulic conductivity. For a homogeneous, isotropic system, the pressure distribution in the unsaturated zone is solely dependent on the boundary conditions. The flowrate is dependent on the permeability and the pressure distribution.

Once the pressure distributions have been established, the change in the distribution due to a change in permeability can be estimated. An increase or decrease in the x- and z-permeability for an isotropic, homogeneous system will have no effect on the pressure distribution, only on the flowrate. This is also valid for an isotropic, heterogeneous system where all the permeabilities are changed the same magnitude. For an anisotropic, homogeneous domain, a transformation must be completed to contract/expand the system in the x- or z-direction with the following relationships (Freeze and Cherry, 1979):

$$X_{trans} = x_{original} \quad \mathit{and} \quad Z_{trans} = z_{original}\frac{\sqrt{k_x}}{\sqrt{k_z}} \tag{2.26}$$

or

$$Z_{trans} = z_{original} \quad \mathit{and} \quad X_{trans} = x_{original}\frac{\sqrt{k_z}}{\sqrt{k_x}} \tag{2.27}$$

Following the transformation, the transformed flow net must be inverted back to the original domain size.

An example of the transformations for an anisotropic system, where k_z has been decreased to one-half of k_x, is shown in Figure 2.8. The top boundary and far right boundary were assumed to be at atmospheric pressure, the watertable was set to be a zero-flux boundary and the well was assigned a constant pressure of P_{well} (Figure 2.8(a)). Using (2.26), the vertical scale was expanded by $\sqrt{2}$, or 1.4, and the new flow net was drawn for $k_x = 2k_z$. Figure 2.8(b) shows the equipotential for pressure P_i. The transformed flow net was inverted back to the original domain size (Figure 2.8(c)). The solid line shown on Figure 2.8(c) represents the equipotential, P_i, for the case in which $k_x = k_z$.

If the original $k_x = k_z$ is available, resulting flownets can be drawn for varying the permeability with:

$$Z_{inv} = z_{trans} \quad and \quad X_{inv} = x_{trans}\frac{\sqrt{k_x}}{\sqrt{k_z}} \tag{2.28}$$

in which every x-dimension of the pressure contour is multiplied by:

$$\frac{\sqrt{k_x}}{\sqrt{k_z}} \tag{2.29}$$

These relationships will be used in later analyses.

2.6 Summary

The equations for incompressible and compressible air flow in the unsaturated zone have been developed in this Chapter. The application of these equations and the boundary conditions will be examined further in the Numerical Model Chapter, along with the results of a comparison between the incompressible and compressible flow solution.

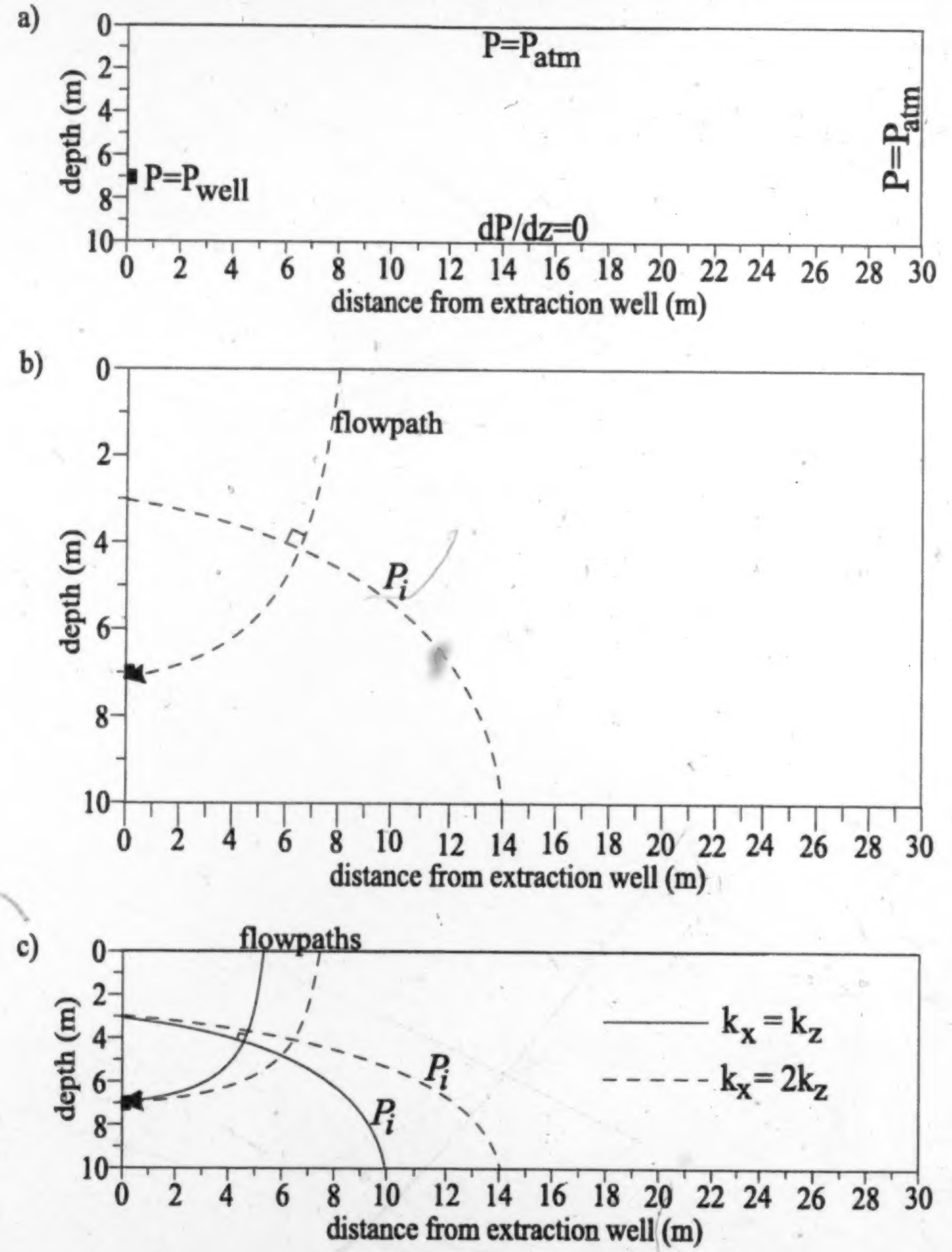
a)
P=P$_{atm}$
P=P$_{well}$
P=P$_{atm}$
dP/dz=0
depth (m)
distance from extraction well (m)
b)
flowpath
P_i
depth (m)
distance from extraction well (m)
c)
flowpaths
P_i
P_i
$k_x = k_z$
$k_x = 2k_z$
depth (m)
distance from extraction well (m)
0
2
4
6
8
10
12
14
16
18
20
22
24
26
28
30

Figure 2.8: Conceptual model of flow net transformation theory: (a) Boundary conditions, (b) Transformed Grid, and (c) Inverted Grid. Solid line represents $k_x = k_z$, and dotted line represents $k_x = 2k_z$

Chapter 3

Numerical Models

A description of the two numerical models utilized for modelling air flow under SVE conditions is discussed in this Chapter. An analysis of the differences between the finite-element model (FEM) and finite-difference model (FDM) models is included, along with example simulations to illustrate the potential difference between the models.

3.1 Overview of Models

Two numerical models were utilized to simulate the advective flow of air in the subsurface during SVE: VapourT and AIR3D. Although both models are capable of modelling transient flow, only steady-state conditions were simulated.

The first numerical model used for SVE evaluation is VapourT (Mendoza, 1992). VapourT is a two-dimensional, finite-element model (FEM) formulated to use either axisymmetric or two-dimensional cartesian coordinates. The model simulates steady-state or transient flow and transport of vapours. It was originally designed to simulate passive vapour migration of a gas, but may be used to simulate SVE conditions if the pressure drawdowns are small, less than 50 %atm (Massmann, 1989). For steady-state flow, the gas is assumed incompressible as explained in Section 2.2.1. Compressibility is incorporated into the transient solutions through the specific storage term in (2.7). VapourT, programmed in Fortran-77, was run on an IBM RS/6000 workstation.

The second numerical model, AIR3D (Joss and Baehr, 1995), simulates steady-state or transient flow of compressible air. It is comprised of three programs: Preair, MODFLOW (McDonald and Harbaugh, 1988) and Postair. Preair converts air flow input data into the format required for MODFLOW's groundwater flow equations. Hydraulic head is replaced with P^2; hydraulic conductivity with permeability; and hydraulic specific storage, S_s, with pneumatic specific storage, S_{3D}. The flow program that solves the partial differential equations is MODFLOW, a three-dimensional finite-difference model (FDM) originally designed to simulate groundwater flow in the saturated zone (McDonald and Harbaugh, 1988). Postair converts the MODFLOW output back into air-phase values with the following relationships:

$$P = \sqrt{h} = \sqrt{\sigma} \tag{3.1}$$

and

$$Q_{air} = Q_{mod}\left(\frac{1}{2\mu P^{\frac{1}{2}}}\right) \tag{3.2}$$

where h is the hydraulic head, σ is a change of variable, P is the pressure, Q_{air} is the flowrate output from AIR3D, Q_{mod} is the flowrate output from MODFLOW and μ is the air viscosity (Joss and Baehr, 1995). Preair, MODFLOW and Postair are all coded in Fortran-77 and were run on an IBM RS/6000 workstation and a personal computer.

3.1.1 Grid Design

A significant difference between the FEM and FDM is the distinct methods of grid design. For both methods, the system domain is divided up into a number of elements/cells. Each element/cell has a number of nodes associated with it.

In the FDM model (AIR3D), the three-dimensional grid is divided into a number of layers (nz), rows (nx) and columns (ny), with the total number of cells equal to $nz \times nx \times ny$. The discretizations in the x-, y- and z-directions are Δx, Δy and Δz, respectively. Node i is located in the centre of a rectangular grid cell (Figure 3.1).

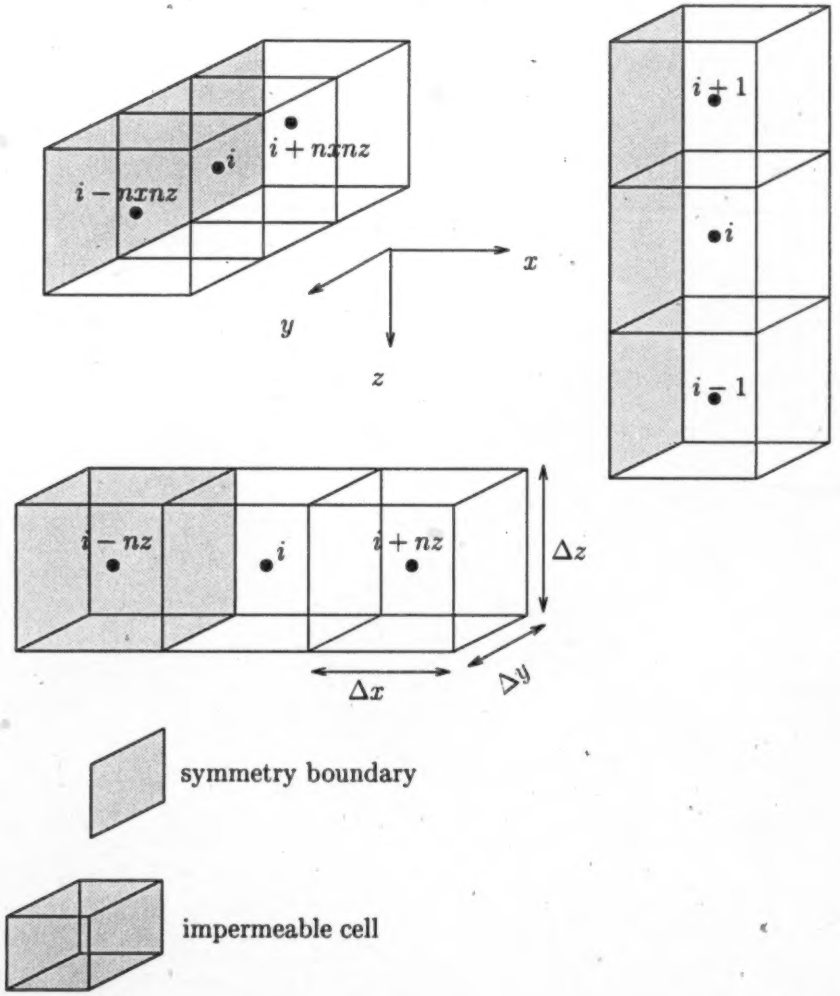
$i - nxnz$
i
$i + nxnz$
x
y
z
$i + 1$
i
$i - 1$
$i - nz$
i
$i + nz$
Δz
Δx
Δy
symmetry boundary
impermeable cell

Figure 3.1: Nodal connectivity for the FDM. i = node number, nz = number of horizontal layers, nx = number of vertical columns/rows, Δz = vertical discretization, Δx and Δy = horizontal discretization

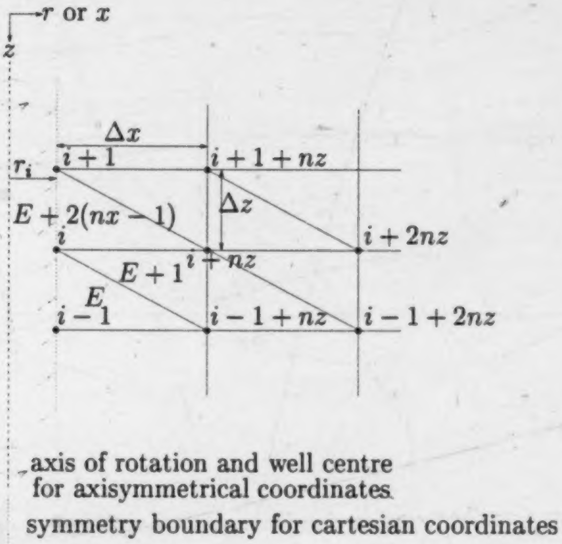

axis of rotation and well centre
for axisymmetrical coordinates
symmetry boundary for cartesian coordinates

Figure 3.2: Nodal connectivity for the node i in the FEM. E = element number, i = node number, nz = number of nodes in the vertical directions, nx = number of nodes in the horizontal direction, Δz = vertical discretization, Δx = horizontal discretization

This method is known as block-centred formulation. At each node, a difference equation is written, relating the pressure values at that node to the 6 neighboring nodes. In Figure 3.1, node i is connected to nodes $i+1$, $i-1$, $i+nz$, $i-nz$, $i+nxnz$ and $i-nxnz$, and is assigned a row, column and layer number. The resulting set of algebraic equations are then solved iteratively with the Strongly Implicit Matrix Solver (SIP) (McDonald and Harbaugh, 1988). The calculated pressure values are representative of the centre of the cell, while flux calculations are completed at the boundaries between two cells.

In contrast to the FDM, the elements in a FEM can be triangular or quadrilateral in shape, which allows irregularly shaped grids to be constructed. With VapourT, the grid is discretized into layers and columns, creating triangular cells, with the number of nodes in the vertical direction equal to nz and the number of nodes in the horizontal direction equal to nx, as illustrated in Figure 3.2. The discretizations in the x- and z-directions are Δx and Δz. Each element has three nodes associated with it. For example, in Figure 3.2, element E has nodes i, $i-1$ and $i-1+nz$. Moreover, each node has a connectivity of 6 neighboring nodes, with node $i+nz$ connected to i, $i+1$, $i-1$, $i+1+nz$, $i+2nz$, $i-1+2nz$ and $i-1+nz$. In VapourT, the nodes are assigned a number, 1 to nn (number of nodes), with node one located in the lower left-hand corner, increasing upwards, and node nn located in the upper right-hand corner. Elements are numbered 1 to ne (number of elements), increasing across rather than upwards. The total number of elements is $ne = 2(nx-1)(nz-1)$ while the total number of nodes is $nn = (nx \times nz)$. Although a head is calculated at every node in the domain, similar to the FDM, interpolation functions are used to assign a head at every point with the FEM. The differential flow equations are solved with Galerkin's method (Wang and Anderson, 1982; Mendoza and Frind, 1990) and the ORTHOFEM solver (Mendoza *et al.*, 1994).

To minimize numerical error in the FDM, it is recommended that the grid spacing increase by no more than 1.5 times larger than the previous cell in a finite-difference grid (Anderson and Woessner, 1992). This is because of the large error associated with the second derivative of (2.24) when an irregular grid is applied (Anderson and Woessner, 1992). When designing a finite-element grid, the aspect ratio, which is defined as the ratio of the maximum to minimum element dimensions, should be less than 5 (Anderson and Woessner, 1992), although values up to 100 are acceptable (*pers. com.*, Mendoza, 1999). It is particularly important to follow these rules in zones where the pressure gradients are the largest (i.e., in the vicinity of the well); elsewhere, these restrictions may be relaxed. Simulation results are shown later to estimate the sensitivity of the flow solution to varying grid spacing.

3.1.2 Fluid Balance and Fate

Fluid balance calculations are conducted to: 1) determine the amount of air entering and exiting the system; 2) determine the fate of air within the domain; and 3) confirm that conservation of mass has been honoured.

For both programs, the flux of air across all external boundaries, including the lateral, watertable and ground surface boundaries and extraction wells, is calculated. For steady-state simulations, the net flux should equal zero. Fluid balance calculations are conducted in both programs to estimate the fluid balance error. AIR3D calculates this as a normalized fluid balance, equal to the difference in fluid flux entering and exiting the system, divided by the total flux. VapourT's fluid balance calculation is the total fluid flux divided by the positive fluid flux (e.g., total flux of air entering the domain). These two fluid balance definitions are not identical and thus cannot be directly compared. They are only used as a balance, code and discretization check within each individual program.

The summaries of all flow across boundaries can also be used to determine the fate of the air within the system and to verify that the grid is of suitable dimensions. To satisfy boundary conditions, it is necessary to place the lateral boundaries at a far enough distance so that less than 5% of the recharge entered from the lateral boundaries, with the remaining 95% entering from the atmospheric layer (Joss and Baehr, 1995).

3.2 Well Representation

As discussed in Chapter 2, the only method of representing an extraction well in AIR3D is by applying a constrained pressure to the extraction well cells. The pressure can then be adjusted to obtain the volumetric flowrate or velocity measured in the field. In VapourT, either a constrained pressure or a constrained flux boundary condition can be applied at the extraction well. Pressure distributions in the extraction well created by a constrained flux in VapourT exhibited larger pressures halfway along the screened portion of the vertical extraction well (Gilmour, 1996). Screen lengths of horizontal wells used for SVE can be much longer than conventional SVE vertical wells, and it is anticipated that the pressure losses along the horizontal well will be more significant due to friction and turbulent flow (White, 1986). Pressure loss is dependent on the soil permeability, size of perforations, roughness of the pipe, and the length and diameter of the well (Bass, 1994).

An alternative method of simulating the pressure loss along a horizontal extraction well was developed using pipe flow theory reported by White (1986). This method involves setting the first cell of the extraction well to a constrained pressure and assigning a representative permeability to the remaining cells of the extraction well. It does not explicitly account for pressure losses due to pipe perforations.

Velocity, v, based on Darcy's law from (2.17) is:

$$v = k\frac{\rho g}{\mu}\frac{\Delta h^*}{\Delta L} \tag{3.3}$$

where k is the permeability, ρ is the fluid density, g is the gravitational constant, μ is the viscosity and $(\Delta h^*/\Delta L)$ is the equivalent head potential gradient. The Darcy-Weisbach equation that describes the relationship between head loss, Δh_f, for turbulent or laminar flow in a pipe and the fluid velocity in a pipe, is (White, 1986):

$$v = \frac{2dg}{fv}\frac{\Delta h_f}{\Delta L} \tag{3.4}$$

where d is the diameter of the pipe, f is the friction factor, and ΔL is the length of the pipe.

The friction factor, f, of a pipe can be found using the Moody Chart for pipe friction (White, 1986). The Moody Chart requires the Reynolds number, R_e:

$$R_e = \frac{vd}{\nu} = \frac{vd\rho}{\mu} \tag{3.5}$$

where ν is the dynamic viscosity; and the Relative Roughness, (R_r):

$$R_r = \frac{\epsilon}{d} \tag{3.6}$$

where ϵ is the average pipe roughness, an empirical value.

Assuming that the fluid is incompressible, (3.3) and (3.4) can be equated to find the effective permeability of the pipe for turbulent flow (k_t):

$$k_t = \frac{2d\mu}{fv\rho} \tag{3.7}$$

Multiplying (3.7) by (d/d) and substituting (3.5) yields:

$$k_t = \frac{2d^2}{fR_e} \tag{3.8}$$

Parameter	Value	Units
d	0.1	m
v	25	m/s
Q	20	m^3/s
ν	1.5×10^{-5}	m^2/s
R_e	1.6×10^{5}	-
ϵ	4.6×10^{-5}	m
R_r	4.6×10^{-4}	-
$f(R_e, R_r)$	0.2	-
k_t	6.3×10^{-6}	m^2
k_l	3.1×10^{-4}	m^2

Table 3.1: Parameters used for pipe permeability analysis.

For reference, the permeability of a pipe with laminar flow (k_l) is (White, 1986):

$$k_l = \frac{d^2}{32} \tag{3.9}$$

For a given volumetric flowrate, and therefore known average velocity in the well, an effective k value may be determined. Table 3.1 lists the some typical parameters and calculated pipe permeabilities. As the velocity decreases along the well, the permeability along the pipe will increase.

In summary, an alternative method of representing an extraction well to account for pressure losses along the pipe is to assign a permeability in the extraction well cells and assign a constrained pressure at only the first extraction cell node. For the two sites to be modelled in the Case Studies and Sensitivity Analysis Chapters, insufficient information was available on the velocities along the well, and only one permeability is applied. This method is compared to the AIR3D default settings for the extraction well in Chapter 5.

3.3 Well Flux Calculations

Differences between the FEM and FDM solutions may occur because of differences in how the well fluxes are calculated and due to the formulations of the equations.

To illustrate how these differences between models arise and how they depend on discretization, the methods of calculating the flowrate at the extraction well for the FEM and FDM are presented. Although this analysis is valid for any node within the domain, it is outlined and illustrated for a single extraction node and is solved for the set of discretized equations :

$$[H]\{h\} = \{F\} \tag{3.10}$$

where $[H]$ is the conductance matrix, $\{h\}$ is the (pressure) head vector and $\{F\}$ is the volumetric flux vecto[illegible]Wang and Anderson, 1982).

Once the pressures have been calculated for the system, the flowrate can be back-calculated. For a node representing a well in a FEM domain with axisymmetric coordinates (Figure 3.2), the volumetric flowrate at that node (F_i), assuming incompressible conditions, is equal to:

$$\begin{aligned} F_i = \pi[(2r_i + \Delta x)\frac{k_x}{\mu}\frac{\Delta z}{\Delta x}(P_i - P_{i+nz}) + (r_i + \frac{1}{3}\Delta x)\frac{k_z}{\mu}\frac{\Delta x}{\Delta z}(P_i - P_{i-1}) \\ +(r_i + \frac{1}{3}\Delta x)\frac{k_z}{\mu}\frac{\Delta x}{\Delta z}(P_i - P_{i+1})] \end{aligned} \tag{3.11}$$

where x and z are the horizontal and vertical coordinate directions, Δx and Δz are the horizontal and vertical discretizations, k_x and k_z are the permeabilities in the x- and z-directions, P_i is the pressure in cell i, and r_i is the well radius (Wang and Anderson, 1982). By setting $r_i = 0$, (3.11) reduces to:

$$F_i = \frac{1}{\mu}[k_x\pi\Delta z(P_i - P_{i+nz}) + k_z\frac{\pi}{3}\frac{\Delta x^2}{\Delta z}(2P_i - P_{i+1} - P_{i-1})] \tag{3.12}$$

A similar analysis is conducted for the FDM. Even though the FDM model selected for modelling in this study assumed compressible flow, the analysis presented here assumes incompressible flow for comparison purposes. The extraction pressure, P_i at node i, represents the pressure at the centre of a rectangular block. The equation for the flowrate at an extraction well for an individual node in the FDM, as illustrated in Figure 3.1, is (Wang and Anderson, 1982):

$$F_i = \frac{k_x}{\mu}\frac{\Delta z\Delta y}{\Delta x}(2P_i - P_{i+nz} - P_{i-nz}) + \frac{k_y}{\mu}\frac{\Delta x\Delta z}{\Delta y}(2P_i - P_{i+nx\cdot nz} - P_{i-nx\cdot nz})$$

$$+\frac{k_z}{\mu}\frac{\Delta x\Delta y}{\Delta z}(2P_i - P_{i+1} - P_{i-1})] \tag{3.13}$$

For axisymmetric flow with the three-dimensional FDM method, it is assumed that $\Delta x = \Delta y$, $k_x = k_y$, and $P_{i+nz} = P_{i-nz} = P_{i+nx \cdot nz} = P_{i-nx \cdot nz}$. Therefore, the flowrate to an extraction cell in the FDM reduces to:

$$F_i = \frac{1}{\mu}[k_x 4\Delta z(P_i - P_{i+nz}) + k_z\frac{\Delta x^2}{\Delta z}(2P_i - P_{i+1} - P_{i-1})] \tag{3.14}$$

If the flux equations for the FEM (3.12) and FDM (3.14) are equated, the following relationships may be determined:

$$\pi\Delta z_{FEM} = 4\Delta z_{FDM} \tag{3.15}$$

and

$$\frac{\pi}{3}\frac{\Delta x^2_{FEM}}{\Delta z_{FEM}} = \frac{\Delta x^2_{FDM}}{\Delta z_{FDM}} \tag{3.16}$$

Thus, for identical grid discretizations, the FEM and the FDM will yield different results: either the pressure distributions or the fluxes may be the same, but not both. Note however, that as Δx and Δz approach zero, the solutions will converge. This analysis demonstrates the approximate nature of numerical solution methods and underlines the necessity of fine grid discretization adjacent to extraction wells.

3.4 Example Simulations

In the following Chapters, VapourT and AIR3D are utilized to simulate air flow under SVE conditions. Since some of the results from the two-dimensional FEM will be compared to the three-dimensional FDM, it was necessary to establish the differences between the two models. A one-dimensional flow scenario was simulated to illustrate the impact of compressibility effects. Differences in the flowrates and pressure distributions from the two models were compared using a two-dimensional vertical well scenario.

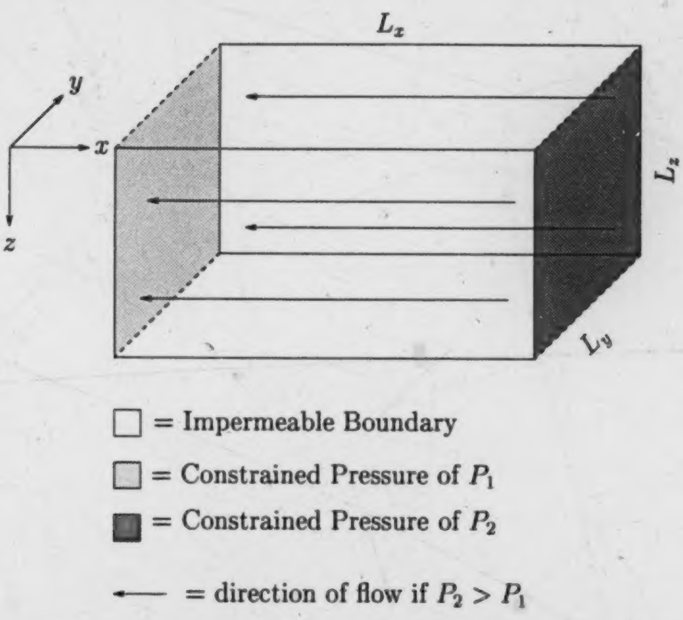
L_x
y
x
z
L_z
L_y
☐ = Impermeable Boundary
▨ = Constrained Pressure of P_1
■ = Constrained Pressure of P_2
← = direction of flow if $P_2 > P_1$

Figure 3.3: Conceptual model of 1D flow analysis.

3.4.1 One-Dimensional Flow Analysis

Due to its relative simplicity, a one-dimensional flow scenario was first chosen to compare the effects of incompressible and compressible flow between AIR3D and VapourT. Figure 3.3 illustrates a generic conceptual model of an one-dimensional flow system. In VapourT, one-dimensional flow was accomplished by setting the top and bottom boundaries to Type II impermeable boundaries, while the left boundary nodes were set to a constrained pressure of P_1, and the right boundary nodes to a constrained pressure of P_2. With AIR3D, the top and bottom layers and the two $x \cdot z$ lateral boundaries were constrained to impermeable boundary conditions. The two $y \cdot z$ lateral boundaries were set to constrained pressures of P_1 and P_2, creating a defined pressure gradient between these two boundaries.

The grids utilized in VapourT and AIR3D are shown in Figures 3.4 and 3.5, respectively. The grid discretization in the vertical direction was 0.5 m. In the horizontal direction, the left and right boundaries with the constrained pressures had a cell width of 0.1 m, with subsequent cell widths increasing by a factor of 1.5.

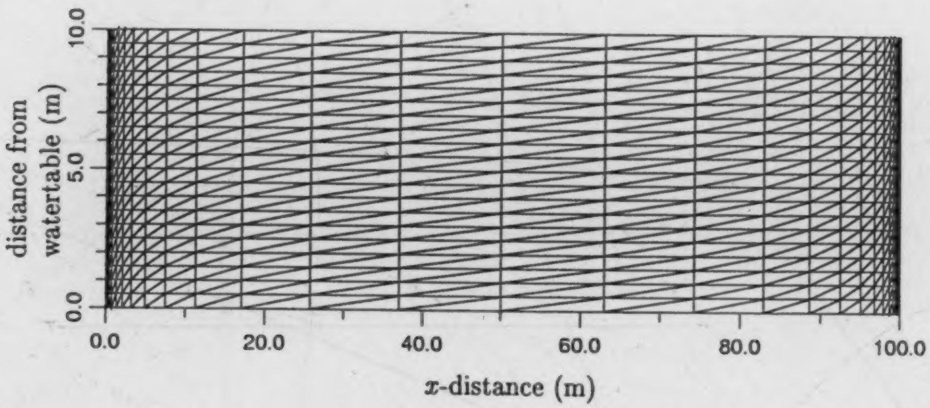
distance from
watertable (m)
0.0
5.0
10.0
0.0
20.0
40.0
60.0
80.0
100.0
x-distance (m)

Figure 3.4: VapourT grid for 1D simulation

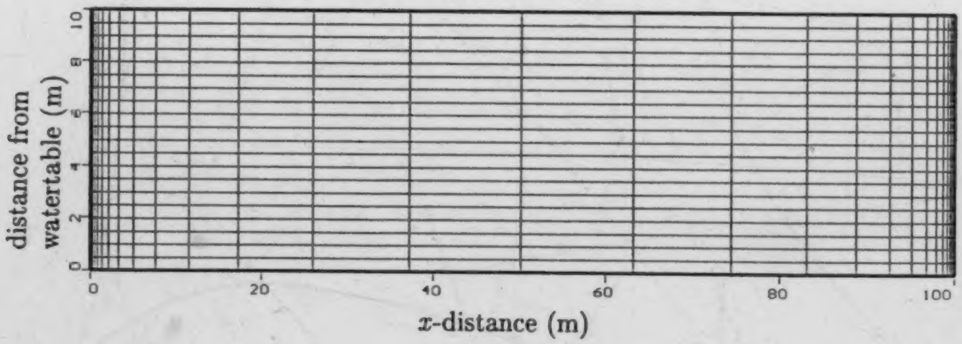
distance from
watertable (m)
0
2
4
6
8
10
0
20
40
60
80
100
x-distance (m)

Figure 3.5: AIR3D grid for 1D simulation

Parameter	Value	Units
L_x	100	m
L_y, L_z	10	m
P_1	variable	%atm
P_2	100	%atm
k	1.0×10^{-10}	m^2
μ	1.76×10^{-5}	kg/m·s

Table 3.2: Parameters used for 1D flow analysis.

Simulations were completed in both models with all parameters and boundary conditions held constant with P_1 varied. The input parameters are listed in Table 3.2.

Based on Darcy's law for steady-state flow, the volumetric flowrate for an incompressible flow (Q_I) in terms of pressure for the above boundary conditions is:

$$Q_I = -A\frac{k}{\mu}\frac{\Delta P}{\Delta L_x} \tag{3.17}$$

where k is the permeability, μ is the fluid viscosity, $A = L_y \times L_z$, $\Delta L = L_2$ - L_1 and $\Delta P = P_2$ - P_1. The volumetric flowrate for a compressible fluid (Q_C) is:

$$Q_C = -A\frac{k}{\mu}\frac{M_w P_{atm}}{RT\rho_{well}}\frac{\Delta P}{\Delta L_x} \tag{3.18}$$

(Joss and Baehr, 1995), where M_w is the molecular weight, R is the universal gas constant, T is the temperature and ρ is the fluid density.

Table 3.3 displays the calculated volumetric flowrate at different pressure drawdowns for VapourT and AIR3D. As the drawdown increased, the difference in the volumetric flowrate between VapourT and AIR3D increased due to compressibility effects, as illustrated in Figure 3.6.

Based on (3.17), the calculated volumetric flowrate increased linearly with increasing pressure. However, in (3.18) the volumetric flowrate increased by the pressure drawdown squared based on the compressible solution. As depicted in Figure 3.6, the incompressible flow analysis underpredicted the flowrate. At a pressure drawdown of 20 %atm, the difference between the flowrate in the two models was 6%.

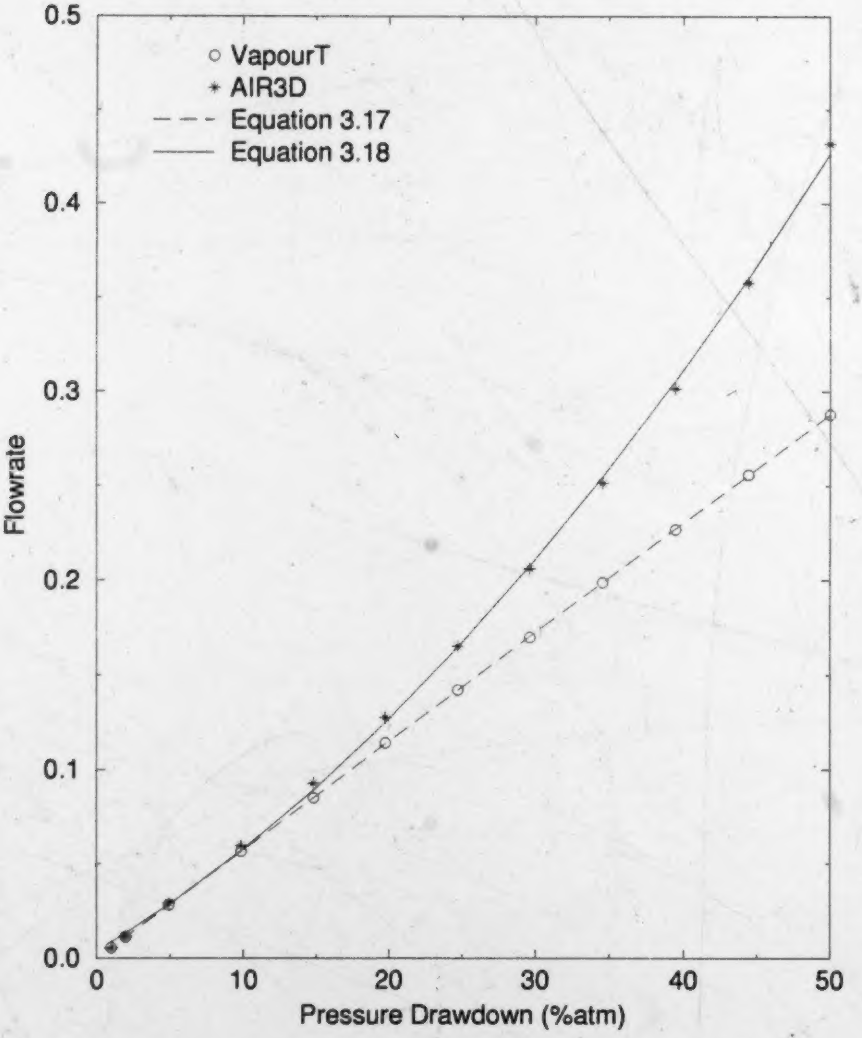

Figure 3.6: Pressure drawdown versus volumetric flowrate for one-dimensional incompressible and compressible flow analysis; units for volumetric flowrate are m^3/s.

Pressure Drawdown (%atm)	VapourT Q_I (m^3/s)	AIR3D Q_C (m^3/s)	Difference %
1	5.7×10^{-3}	5.7×10^{-3}	0.3
5	2.8×10^{-2}	2.9×10^{-2}	1.3
10	5.7×10^{-2}	6.0×10^{-2}	2.7
20	1.1×10^{-1}	1.3×10^{-1}	5.6
50	2.9×10^{-1}	4.3×10^{-1}	19.6

Table 3.3: Volumetric flowrates for 1D flow analysis.

This difference increases to 20 % when the pressure difference is 50 %atm. For typical SVE systems, a maximum pressure drawdown of 50 %atm was suggested by Massmann (1989) for groundwater equations to apply gas flow. As expected for one-dimensional flow simulations, the pressure contours were vertical throughout the section (i.e., no component of z-direction flow).

3.4.2 Two-Dimensional Flow to a Single Vertical Well

A comparison of the results between AIR3D, VapourT and an analytical model was conducted. This allowed the sensitivity of the grid design on the flow results to be determined.

The conceptual model and problem simulated were similar to the example outlined in the AIR3D manual involving axisymmetric flow to a single vertical well (Joss and Baehr, 1995). This example was an excellent problem for comparing the FEM and FDM because the flow solution expected would be difficult to solve numerically: flow converges to a point and there are large changes in spatial gradients throughout the system. In additional, an analytical solution to the problem is included in the AIR3D manual.

The initial grid structure and boundary conditions for both models are shown in Figure 3.7. The problem involves a single vertical extraction well placed in the middle of the domain with a well radius of 0.1 m and a total length of 1.6 m. The

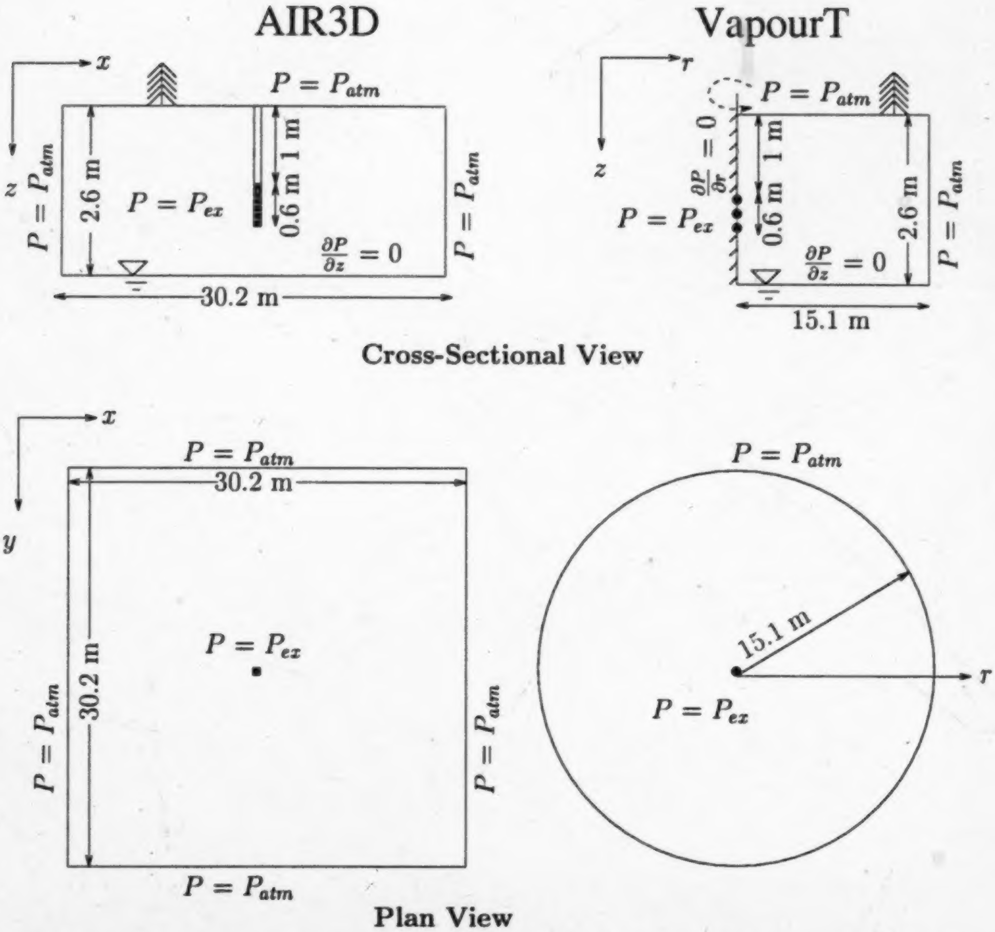
AIR3D

VapourT

Cross-Sectional View

Plan View

x
z
y
r
$P = P_{atm}$
$P = P_{ex}$
$\frac{\partial P}{\partial z} = 0$
$\frac{\partial P}{\partial r} = 0$
2.6 m
1 m
0.6 m
30.2 m
15.1 m

Figure 3.7: Boundary conditions and dimensions for the FDM (AIR3D) and FEM (VapourT) example problem, cross-sectional and plan views. The diagrams are not to scale.

well was screened between 1.0 and 1.6 m depth. The ground surface boundary was set to atmospheric pressure while the lateral boundaries were placed at a distance of 15.1 m from the well. The lateral dimensions were sufficiently large that greater than 99% of the air entering the system did so from the atmosphere. Figures 3.8 and 3.9 illustrate the initial grids utilized in VapourT and AIR3D respectively. Moving away from the well, there were 5 columns for each grid spacing of 0.2, 0.4, 0.8 and 1.6 m in the x-direction. The grid discretization in the z-direction was 0.2 m. For VapourT (Figure 3.8), the left boundary was the axis of rotation and the top and bottom layer thicknesses were set to 0.1 m in order for the nodes of the FEM to be at the same location as the cell centres in the FDM grid. The well was assigned a pressure drawdown of 10 %atm. In concordance with Joss and Baehr (1995), the air permeability in the x-direction was 1.0×10^{-12} m^2, half the magnitude of the z-direction air permeability.

The calculated extraction flowrate out of the vertical well for VapourT was 0.70×10^{-3} m^3/s and 1.70×10^{-3} m^3/s for a well radius of 0 and 0.1 m respectively and 1.03×10^{-3} m^3/s for AIR3D. The extraction rate calculated for the analytical model was 1.70×10^{-3} m^3/s. The pressure distributions for the two models are shown in Figures 3.10, 3.11 and 3.12. Both the flowrate calculations and pressure distributions verify that the pressure drawdowns in AIR3D are greater than the pressure drawdowns in VapourT. The differences between the flowrates and pressure distributions between AIR3D and VapourT can be attributed to the coarseness of the grid utilized, compressibility effects and due to different volumes between a cubic and cylindrical grid domain. These factors are explored further below.

Explanation of Additional Simulations

Additional simulations were performed to determine the dependency of flowrate on grid discretization in both programs. The grid discretization was decreased to 0.025 m for the first column/row/layer and each subsequent column/row/layer increased, moving away from the well, by a discretization factor (f_{inc}) of 1.2, 1.5 or 2.0 times

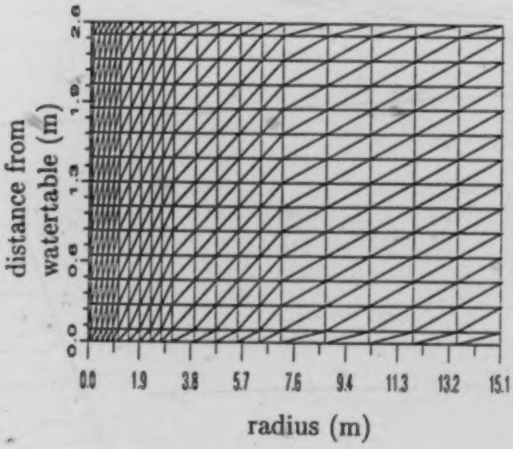
distance from
watertable (m)
0.0
0.6
1.3
1.9
2.6
0.0
1.9
3.8
5.7
7.6
9.4
11.3
13.2
15.1
radius (m)

Figure 3.8: Initial grid for VapourT simulations.

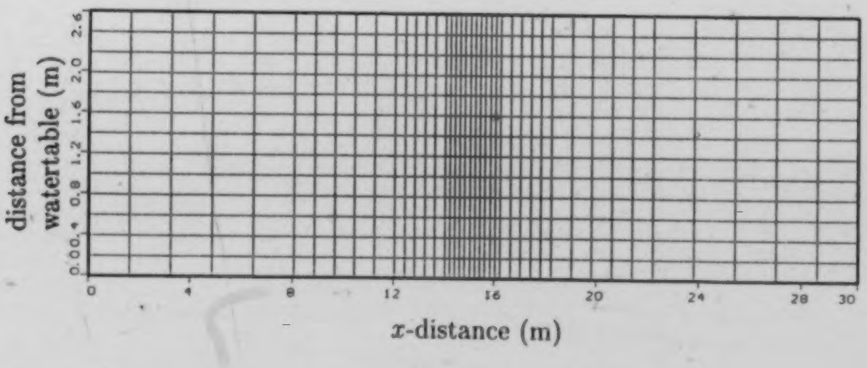
distance from
watertable (m)
0.0
0.4
0.8
1.2
1.6
2.0
2.6
0
4
8
12
16
20
24
28
30
x-distance (m)

Figure 3.9: Initial grid for AIR3D simulations.

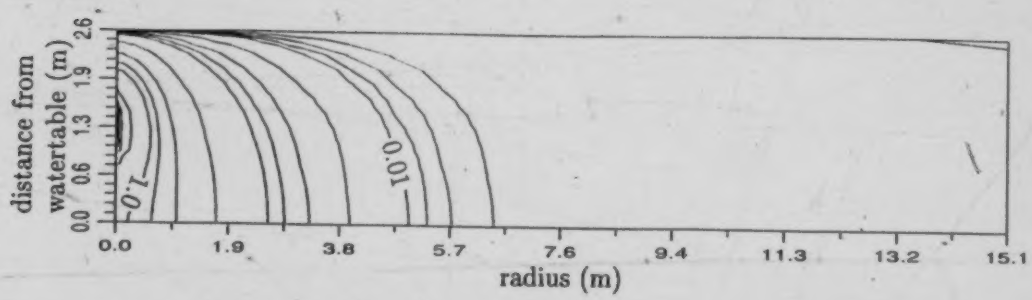

Figure 3.10: Pressure drawdown distribution for VapourT vertical well simulation, r_i = 0 m. Contour interval (%atm): 0 to 0.01 by 0.0025; 0.01 to 0.1 by 0.025; 0.1 to 1.0 by 0.25; and 1.0 to 10 by 2.5

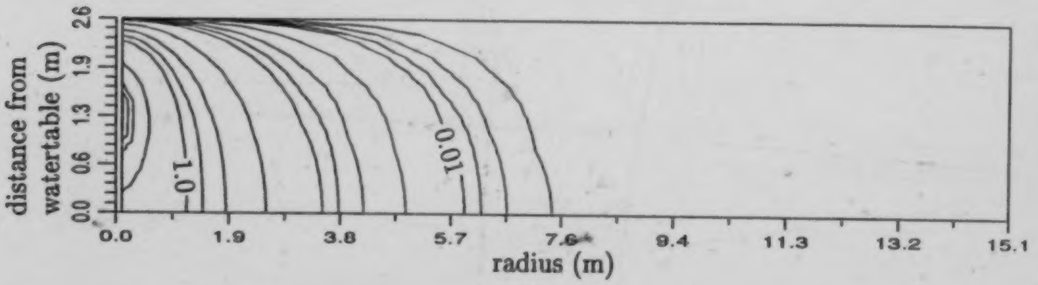

Figure 3.11: Pressure drawdown distribution for VapourT vertical well simulation, r_i = 0.1 m. Contour interval (%atm): 0 to 0.01 by 0.0025; 0.01 to 0.1 by 0.025; 0.1 to 1.0 by 0.25; and 1.0 to 10 by 2.5

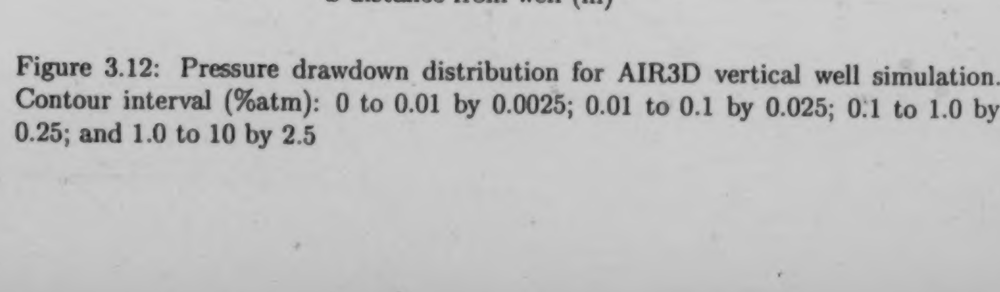

Figure 3.12: Pressure drawdown distribution for AIR3D vertical well simulation. Contour interval (%atm): 0 to 0.01 by 0.0025; 0.01 to 0.1 by 0.025; 0.1 to 1.0 by 0.25; and 1.0 to 10 by 2.5

the previous spacing. In VapourT, the number of triangular elements for the original grid increased from 588 to 858 for f_{inc} of 2.0, 1332 for f_{inc} of 1.5, and 2820 for f_{inc} of 1.2. In AIR3D, the original number of cells increased from 21 853 to 25 688 for f_{inc} of 2.0, 54 432 for f_{inc} of 1.5, and 190 800 for f_{inc} of 1.2.

In VapourT, the extraction well radius (r_i) may be specified to be zero, in which case the extraction well nodes fall along the axis of rotation. Alternatively, the well radius may be offset from the axis of rotation as illustrated in Figure 3.2. Previous vertical well simulations by Gilmour (1996) concluded that setting the well radius to equal zero resulted in model pressure drawdowns that underpredicted observed field pressures. The analysis by Gilmour (1996) also compared the differences in the pressure distributions when the vertical well was assigned a constrained flux instead of a constrained pressure. It was concluded that there was little difference in the distribution, except very close to the extraction well. The effects of the well radius and type of constrained boundary in the well are analyzed here.

With the three-dimensional domain in AIR3D, the memory requirements could quickly increase beyond the capacity of the computers utilized; therefore modelling a half or quarter grid instead of a full grid was investigated. For axisymmetric flow to a single vertical well in a full three-dimensional FDM, the flowpaths are nearly identical for any cross-section in any xz/yz plane through the extraction well. Therefore it is possible to simulate the same problem in AIR3D with only a half or quarter grid by applying symmetry boundaries, as illustrated in Figure 3.13. A symmetry boundary is an impermeable boundary and the pressure distribution on the other side of the symmetry boundary should be a mirror image. A plan view of a quarter grid is illustrated in Figure A.1 in Appendix A.

A difference in the flowrate calculations between full grids and partial grids can occur due to the location where the flowrate is calculated. With the full grid (Figure A.2 in Appendix A), the flowrate is calculated half-way between nodes 1 and 2, which is 0.1 m from the extraction well. With the quarter grid (Figure A.1 in Appendix A), the size of the extraction cell was one-quarter of that of the full grid,

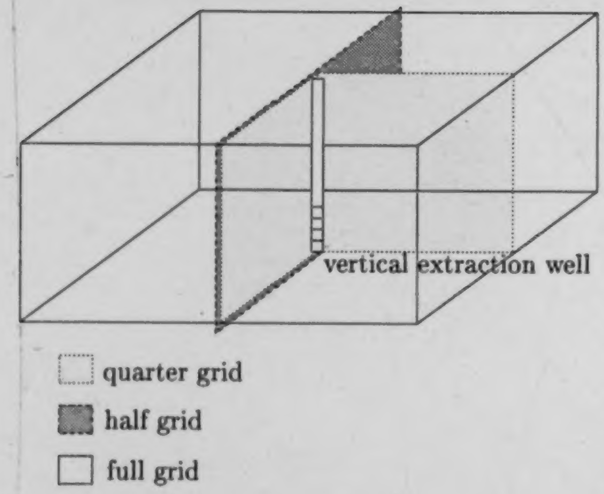

Figure 3.13: Illustration of full, half and quarter grids in AIR3D.

and the flowrate was calculated at a location of 0.05 m from the extraction well. This caused Δx in (3.14) to change and therefore the calculated flowrates were not the same.

One final aspect investigated was the effect of flow in the cells directly above the vertical extraction well. In the VapourT, flow occurs in the nodes above the vertical well. In AIR3D it is possible to specify whether the cells above the constrained pressure cells of the extraction well allow flow or not.

Simulations for the vertical well are outlined in Tables 3.4 and 3.5 and illustrated in Figures A.1 to A.7 in Appendix A. For convenience, all simulations have been assigned an ID and symbol. The prefix 'v' signifies VapourT simulations, while 'a' indicates AIR3D simulations. The VapourT simulations were divided into two base cases: Base Case 1 (v1), with the initial coarse grid, and Base Case 2 (v2), with a finer grid discretization. Similarly, the AIR3D simulations were separated into Base Case 3 (a3) and Base Case 4 (a4) for the initial and fine grid discretizations respectively. Within each Base Case, additional simulations were conducted to observe changes in the pressure distributions and flowrates due to other factors.

VapourT Simulations	Symbol	ID	Flowrate ($\times 10^{-3}$ m^3/s)	Figure
Set 1 Base Case:				
initial grid, $r_i = 0$ m	—	v1	0.72	A.3
$r_i = 0.1$ m	□	v1_r	1.70	A.5
Set 2 Base Case:				
fine grid, $f_{inc} = 1.2$, $r_i = 0$m	━	v2	1.72	A.6
$r_i = 0.1$ m	■	v2_r	1.56	A.7
increase domain volume to equal AIR3D domain volume	▶	v2_{vol}	1.76	A.6
constrained flux	◆	v2_{flux}	1.70	A.6
$f_{inc} = 1.5$	na	v$2_{f1.5}$	1.76	A.6
$f_{inc} = 2.0$	●	v2_{f2}	1.84	A.6

Table 3.4: VapourT simulations

AIR3D Simulations	Symbol	ID	Flowrate ($\times 10^{-3}$ m^3/s)	Figure
Set 3 Base Case				
initial full grid, no flow	– – –	a3	1.03	A.2
quarter grid	×	a3_q	1.22	A.1
full grid, flow above well	+	a3_{fl}	1.14	A.2
Set 4 Base Case:				
fine grid, $f_{inc} = 1.2$, full grid, no flow	━ ━ ━	a4	1.71	A.4
quarter grid	×	a4_q	1.75	
full grid, flow above well	+	a4_{fl}	1.84	
$f_{inc} = 1.5$	na	a$4_{f1.5}$	1.68	
$f_{inc} = 2.0$	○	a4_{f2}	1.61	

Table 3.5: AIR3D simulations

For VapourT, the effect of the well radius was examined in $v1_r$ and $v2_r$, along with the consequences of adjusting the discretization factor from 1.2 (v2) to 1.5 and 2.0 ($v2_{f1.5}$ and $v2_{f2}$, respectively). An additional simulation, $v2_{vol}$, examined the impact of increasing the grid dimensions so the cylindrical volume of VapourT equals the cubic domain of AIR3D. Base Case 2 was also compared to a simulation where the well was represented by a constrained flux rather than a constrained pressure ($v2_{flux}$).

The AIR3D simulations analyzed the effect of flow above the well in the initial grid simulations ($a3_{fl}$) and with fine discretization ($a4_{fl}$). Reducing the size of the grid domain to a quarter grid was also studied with the initial ($a3_q$) and fine grid ($a4_q$). Similar to the VapourT simulations, the discretization factor was changed to 1.5 ($a4_{f1.5}$) and 2.0 ($a4_{f2}$) to examine the effect of grid discretization on the flow solution.

Results

The calculated extraction flowrates for VapourT and AIR3D, are listed in Tables 3.4 and 3.5, range from 0.70×10^{-3} m^3/s to 1.84×10^{-3} m^3/s. Figure 3.14 shows the pressure drawdown curves at the elevation of the extraction well (1.3 m depth), while Figure 3.15 displays pressures at a depth of 0.5 m.

The pressure drawdowns were also compared to an analytical solution that solves axisymmetric steady-state flow to a single vertical well with the ground surface at atmospheric pressure and an infinite lateral domain (Joss and Baehr, 1995). The analytical solution provides the steady-state pressure distributions for a given extraction flowrate. The pressure distribution for the analytical solution with an extraction flowrate of 1.70×10^{-3} m^3/s is shown on Figure 3.16, along with selected VapourT and AIR3D fine discretization simulations. The pressure distributions from VapourT and AIR3D are nearly identical to that of analytical model.

Generally, all simulations provided a good estimate of the pressure drawdown and flowrates. The initial grid discretization given in the AIR3D example (i.e., a3) (Joss

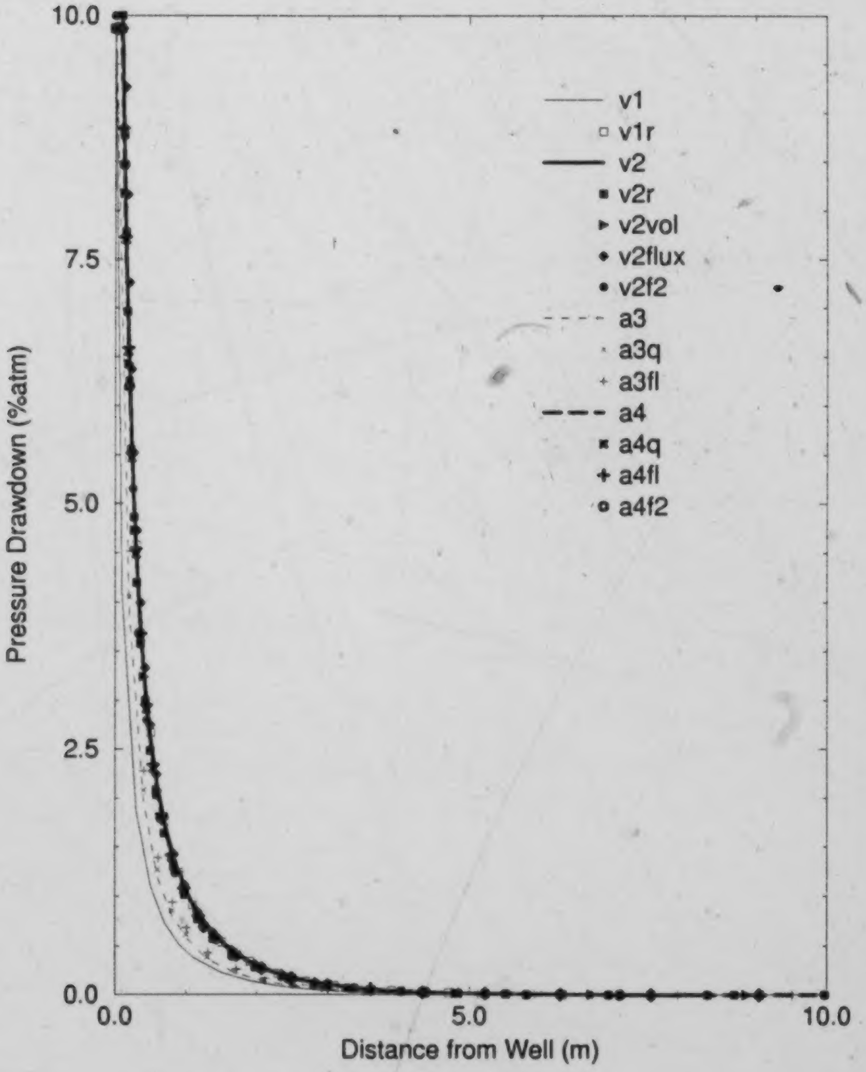

Figure 3.14: Pressure drawdown at vertical extraction well elevation.

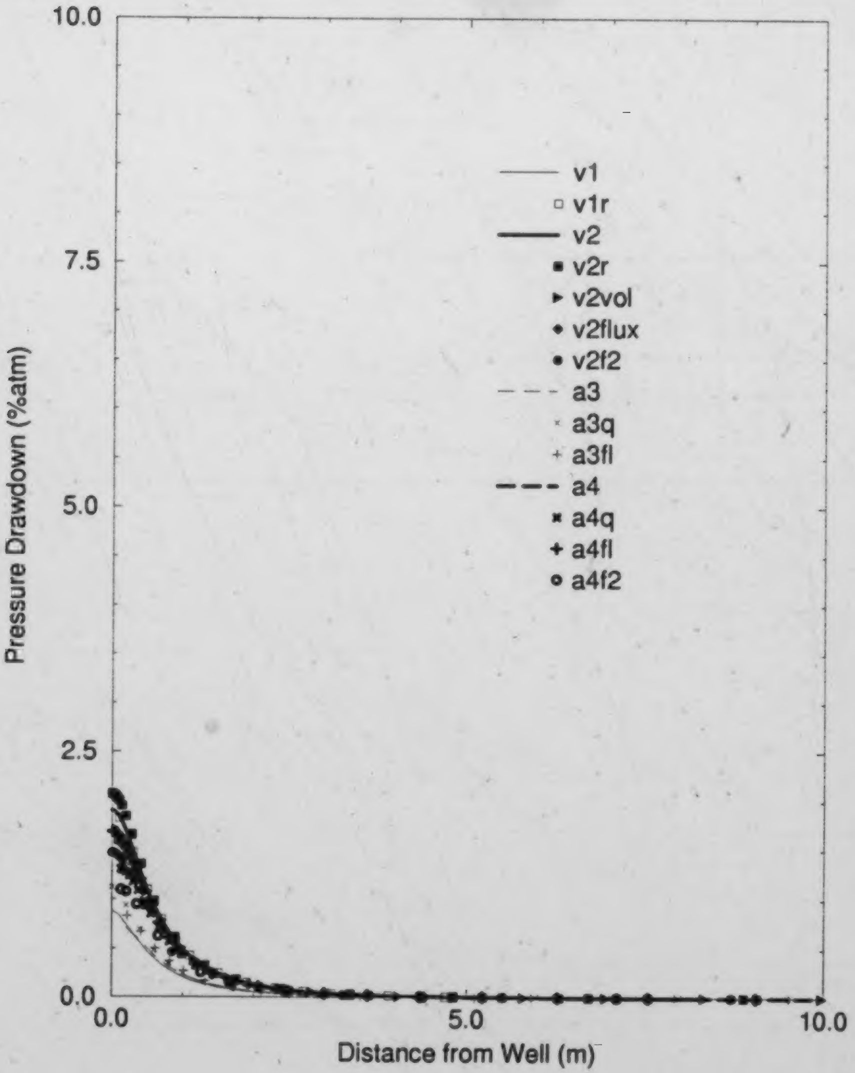

Figure 3.15: Pressure drawdown at 0.5 m depth.

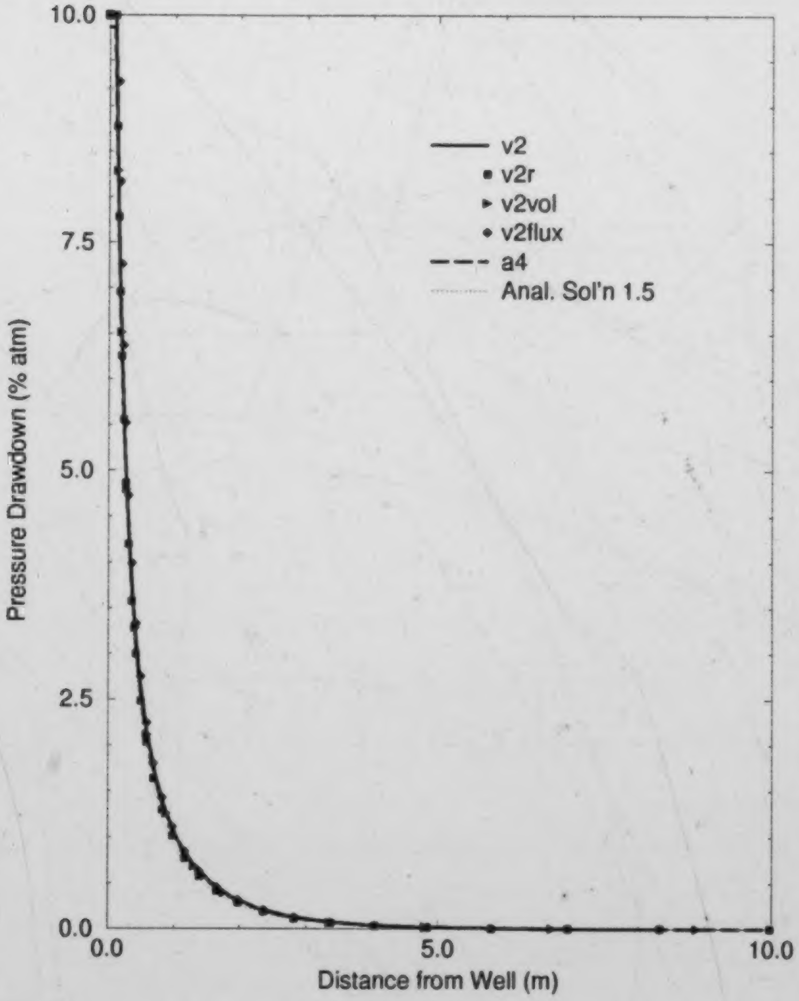

Figure 3.16: Comparison with analytical solution at vertical extraction well elevation.

and Baehr, 1995) yielded lower flowrates and pressure drawdowns than predicted by the analytical model. When the discretization factor was less than 2.0, the pressure distributions between VapourT and AIR3D were very similar and the difference between the flowrates was less than 10%.

3.5 Summary

A one-dimensional flow analysis was conducted to illustrate the effects of incompressible and compressible flow. The VapourT and AIR3D simulations began to exhibit variance greater than 5% in the pressure distributions when the pressure drawdown was greater than 20 %atm. The aim of the vertical simulations was to determine the most appropriate grid discretization and design for the comparison of the two-dimensional FEM simulations and the three-dimensional FDM simulations based on acceptable differences between pressure distributions and the calculated well fluxes. A quarter grid designed in AIR3D with the cell containing the well being equal to the well radius, and the size of the next cell increased by no more than a factor of 2.0, produced results that agreed with an analytical model. The most suitable grid design in VapourT was to set the well radius in the model to the field well radius. These methods satisfy the flux accuracy without exceeding memory limits.

Chapter 4

Case Studies

Air flow to vertical and horizontal soil-vacuum extraction (SVE) wells at two sites is discussed in this Chapter. These SVE systems were installed at gas plants near Strachan, Alberta, and a second site referred to as Site B, by Komex International Ltd. (Komex). Using geologic and hydrogeologic properties obtained through field activities by Komex, simulations of two-and three-dimensional air flow to vertical and horizontal extraction systems were analyzed.

4.1 Strachan

Strachan is the Gulf Canada Resources Limited Strachan Sour Gas Plant, a natural gas processing plant located approximately 150 km north-west of Calgary. This site was selected by the Canadian Association of Petroleum Producers (CAPP) as a research and demonstration project for studying different remediation techniques at gas plants in Alberta (Armstrong *et al.*, 1995). Site investigations were conducted by Komex to delineate soil and groundwater contamination and to evaluate a number of remediation techniques. In addition to SVE, bioventing, air sparging, and dual-phase extraction have also been employed. Several summary reports detail the site activities (Komex, 1994a; Komex, 1994b; Komex, 1994d; Komex, 1996). Furthermore, a conference paper on modelling results (Armstrong *et al.*, 1995) and a thesis on bioventing activities (Gilmour, 1996) have been published.

SVE was selected as a remediation technique at Strachan for three reasons: 1) the underlying geology consists of very permeable sand and gravel, conditions which allow for high air flowrates; 2) the contamination at the site is volatile; and 3) a large zone of residual hydrocarbon exists in the unsaturated zone because of watertable fluctuations (Armstrong *et al.*, 1995). One horizontal SVE extraction trench (herein referred to as the horizontal well), five vertical wells, 28 monitoring points, and three oxygen and temperature probes were installed at the site as part of the SVE monitoring and remediation program.

4.1.1 Geology and Hydrogeology

Geophysical seismic refraction surveys were utilized near the location of the horizontal well to determine the thickness of the till because it was necessary to minimize excavation costs by locating the horizontal well in an area with a thin clay unit. The surficial geology of the unsaturated zone in the vicinity of the horizontal well consists of a 2.0 to 2.5 m thick layer of silty clay till overlying approximately 7 m of very-permeable, coarse sand and gravel with cobbles (herein referred to as sand). Bedrock underlies the sand. According to Freeze and Cherry (1979), permeabilities (k) typically range from 10^{-19} m^2 to 10^{-13} m^2 for glacial till, from 10^{-14} m^2 to 10^{-10} m^2 for silty sand, and from 10^{-13} m^2 to 10^{-7} m^2 for sands and gravels. The sand permeability was initially estimated by visual inspection, geophysical testing and tracer tests to be 8×10^{-10} m^2 (Komex, 1994d). Numerical modelling by Gilmour (1996) and Armstrong *et al.* (1995), based on observed pressures during extraction from a single vertical well, resulted in permeability estimates of 6×10^{-12} m^2 for the till, and 2.5×10^{-10} m^2 in the horizontal direction and 1.5×10^{-10} m^2 in the vertical direction for the sand. The clay till overlying the sand is believed to act as an impermeable cover, which limits air flow short-circuiting and water infiltration.

The watertable lies at a depth of 7 to 8 metres, but fluctuates seasonally by up to 3 m (Komex, 1994b). The average groundwater flow velocity is estimated to be 1 m/day towards the south (Gilmour, 1996).

4.1.2 Contamination Characterization

A layer of free-phase liquid gas condensate exists in the subsurface, covering approximately 65 000 m^2 and having a volume of roughly 10 000 m^2 (Armstrong *et al.*, 1995). Past observations have shown up to 1.5 m of free-phase liquid in observation wells. As a result of seasonal watertable fluctuations, it is assumed that there has been vertical smearing of similar magnitude to the watertable fluctuations, leaving residual above the free-phase product in the unsaturated zone.

The composition of the condensate is believed to range from C_5 to C_{22} hydrocarbons with the vapour phase containing primarily cyclic and branched chains (Komex, 1994b). Variation in hydrocarbon composition between that found in the analyses of the soil and vapour samples was observed, with the absence of aromatics and straight chain alkanes in the vapour phase believed to be a result of preferential removal during SVE testing and due to biodegradation. Highest hydrocarbon concentrations were found closest to the capillary fringe in the proximity of the SVE-1 vertical extraction well, shown in Figure 4.1 (Komex, 1994b). A laboratory column test was conducted prior to initiating the SVE system and the results indicated that under the ideal conditions of the laboratory test, SVE would be very efficient in removing the condensate from the site (Komex, 1994d).

4.1.3 Vertical and Horizontal Well Installation and Configuration

The presence of cobbles in the subsurface effectively eliminated directional drilling as a method of installing the horizontal well at Strachan. Instead, the horizontal well was installed by excavating a trench to 0.2 m below the base of the till with a backhoe. A 30 m long 0.075 m (3 in) diameter PVC pipe with slots only on the bottom half was placed in the trench at the top of the sand. A 7.5×10^{-5} m (30 mil) PVC liner was placed on top of the pipe to limit short-circuiting (Komex, 1996). The trench was filled with excavated till and compacted. Three risers pipes were

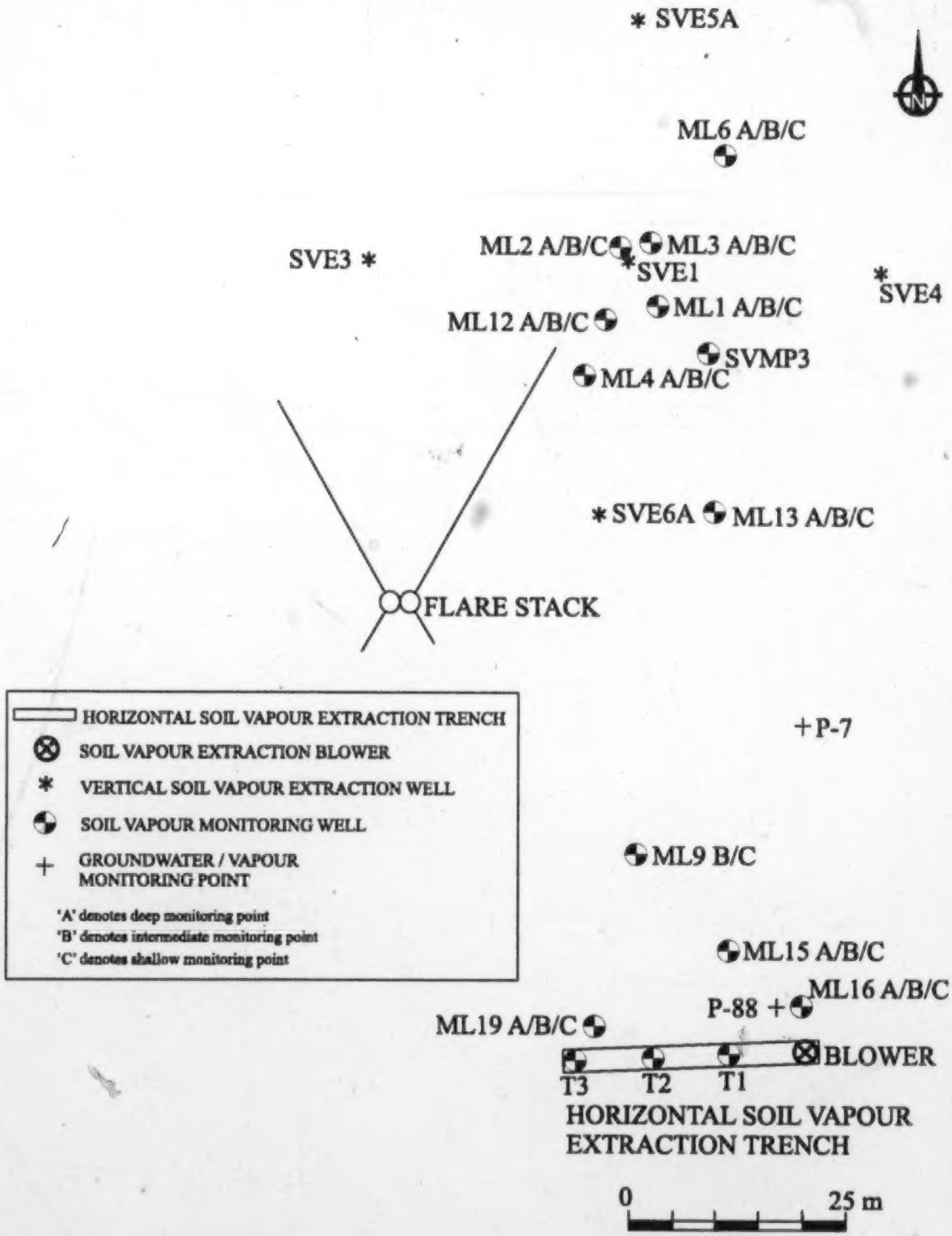
SVE5A
N
ML6 A/B/C
SVE3
ML2 A/B/C
ML3 A/B/C
SVE1
SVE4
ML12 A/B/C
ML1 A/B/C
SVMP3
ML4 A/B/C
SVE6A
ML13 A/B/C
FLARE STACK
HORIZONTAL SOIL VAPOUR EXTRACTION TRENCH
SOIL VAPOUR EXTRACTION BLOWER
VERTICAL SOIL VAPOUR EXTRACTION WELL
SOIL VAPOUR MONITORING WELL
GROUNDWATER / VAPOUR MONITORING POINT
'A' denotes deep monitoring point
'B' denotes intermediate monitoring point
'C' denotes shallow monitoring point
P-7
ML9 B/C
ML15 A/B/C
ML16 A/B/C
P-88
ML19 A/B/C
BLOWER
T3
T2
T1
HORIZONTAL SOIL VAPOUR EXTRACTION TRENCH
0
25 m

Figure 4.1: Site map at Strachan (Komex, 1996).

connected to the trench pipe at 10, 20 and 30 m from the well header to monitor pressures within the trench. The horizontal well was located approximately 70 m to the south of a flare stack and coincided with the known location of the contaminant plume (Komex, 1996). Furthermore, the horizontal well was oriented with the length of the well running perpendicular to the predicted southward migration path of the contaminant plume (Komex, 1996).

A vertical extraction well (SVE-1) was located approximately 96 m from the horizontal well. Four additional vertical extraction wells were located 30 m radially from SVE-1 at 90° intervals. SVE-1 was installed using a Becker Hammer drill rig and was screened between 5.3 and 8.3 m depth (Komex, 1994d; Armstrong *et al.*, 1995). A number of observation wells were used to collect pressure data and hydrocarbon, oxygen and carbon-dioxide concentrations. The locations of vertical and horizontal extraction wells and monitoring wells at the site are illustrated in Figure 4.1.

The 15 HP blower from the vertical SVE system was used with the horizontal well. For the horizontal SVE test, the blower was capable of extracting air at 170 L/s with a corresponding suction of 8.3 kPa (8.4 %atm) (Komex, 1996).

The cost of installing the horizontal well was approximately equivalent to two vertical wells (Komex, 1996). This cost comparison took into account the longer installation time for the horizontal well, 2 days, compared to hours for two vertical wells, and the fact that vertical well installation required more specialized equipment (Komex, 1996). Operational and maintenance costs such as blowers and additional surface piping and headers were not included in the cost comparison.

4.1.4 Previous Field Activities and Modelling Results

Two tests were conducted at Strachan to evaluate the efficiency of vertical and horizontal SVE systems. The vertical system operated between 5 May and 10 June 1993, while the horizontal SVE test was conducted between 1 December 1994 and 6 January 1995. During the vertical SVE test, approximately 10 000 kg of hydrocarbons were removed via volatilization from the subsurface, an average of 300 kg/d, com-

Strachan Simulations	ID	k_{till} (m^2)	k_{sand} (m^2)
3D horizontal well simulation (AIR3D)	k_{A1}	1.0×10^{-12}	7.0×10^{-11}
2D axisymmetric vertical well simulation (VapourT) (Armstrong *et al.*, 1995; Gilmour, 1996)	k_{A2}	6.0×10^{-12}	k_h=1.5×10^{-10} k_v=2.5×10^{-10}
2D cartesian horizontal well simulation (VapourT) (Armstrong *et al.*, 1995)	k_{A3}	6.0×10^{-12}	2.0×10^{-10}
Additional 3D horizontal well simulation (AIR3D)	k_{A4}	2.05×10^{-12}	6.15×10^{-11}

Table 4.1: Till and sand permeabilities selected for different modelling simulations at Strachan.

pared to only 20 to 60 kg/d for the horizontal well system (Komex, 1994d; Komex, 1996). Although the difference between the mass removal of the two systems could be attributed to the different contaminant distribution and different initial concentrations, it is likely that the location of the vertical well deeper in the unsaturated zone, closer to the higher concentrations of condensate resulted in a higher mass removal rate (Komex, 1996). The mass removal rate by biodegradation was also estimated and found to be approximately 230 kg/d in both systems (Komex, 1996).

Air flow and contaminant transport modelling was performed by Armstrong *et al.* (1995) and Gilmour (1996). Based on observed pressures and the extraction rate (Q_{ex}) from a single vertical well pump test, a permeability of 6.0×10^{-12} m^2 for the till and 2.5×10^{-10} m^2 in the horizontal direction and 1.5×10^{-10} m^2 in the vertical direction for the sand was estimated by considering radial flow to a single vertical well with axisymmetric coordinates in VapourT. These permeabilities will be referred to as k_{A2} throughout the remainder of this Chapter (Table 4.1). A similar analysis of the horizontal SVE test data using cartesian coordinates in VapourT estimated a similar till permeability, but a sand permeability of 2.0×10^{-10} m^2, referred to as k_{A3} in Table 4.1 (Armstrong *et al.*, 1995).

Using k_{A2} and k_{A3} permeability values, the performance of the vertical well and horizontal well were compared (Armstrong *et al.*, 1995). First, the area of coverage for a given pressure and depth was observed and secondly, travel time to the well from a given distance and depth was estimated. Note that the distance from the vertical well, which was modelled with axisymmetric coordinates, is a radial distance, whereas the distance from the horizontal well, where cartesian coordinates were used, is the lateral distance perpendicular to the midpoint of the well.

The results show that the horizontal well exhibited greater model drawdowns than the vertical well. At a depth of 6.5 m, a pressure drawdown of 1 % atm was observed 46 m from the horizontal well, compared to 28 m for the vertical well. These distances increased to 97 m and 71 m, respectively, for 0.1 %atm drawdown (Armstrong *et al.*, 1995). The horizontal model results were supported by measuring oxygen concentrations during the horizontal SVE test. Elevated O_2 values were observed during the extraction test at a monitoring point 100 m away at a depth of 7 to 8 m (Komex, 1996). After 1 hour of SVE extraction, model particle tracking results showed that particles at a depth of 6.5 m and a lateral distance of 15 m from the vertical well, but only particles 7 m from the horizontal well at the same depth were removed (Armstrong *et al.*, 1995). This was partly attributed to near well effects: a larger pressure gradient existed at a depth of 6.5 m with the vertical well screened down to 6.5 m (Komex, 1996). The differences in pressure distributions between the horizontal and vertical well decreased at larger travel times and distance from the well.

The conclusion of this approximate evaluation was that one horizontal well was roughly equivalent in areal coverage and travel time to 1.5 to 2 vertical wells and the cost of the 30 m horizontal trench/well was close to the cost of drilling 2 vertical wells (Armstrong *et al.*, 1995).

Review of the input and output files from the VapourT simulations for the horizontal well showed that a well flowrate of 0.17 m^3/s was specified in Armstrong *et al.*'s (1995) analysis. However, an extraction rate of 0.085 m^3/s should have been used to account for the half grid utilized. This adds a degree of error to the permeabilities, travel times and area of coverage results from the horizontal SVE modelling performed by Armstrong *et al.* (1995).

4.1.5 Numerical Model Set-up

Extensive two-dimensional modelling was completed with the vertical extraction well test and the horizontal extraction well test with VapourT by Armstrong *et al.* (1995) and Gilmour (1996). Thus, this study focused on using the AIR3D model to analyze three-dimensional flow with the data acquired from the horizontal well SVE test. The horizontal well SVE test involved measuring the horizontal well extraction flowrate while observing pressures in the extraction well and 17 surrounding monitoring points, located at different depths and distances from the well, after steady-state conditions were reached.

Pressure Drawdown Analysis from Horizontal SVE Testing

The measured steady-state pressure drawdown distributions in the sand during the field test of the horizontal well SVE are illustrated in Figure 4.2 for cross-sectional and plan views respectively. No pressure data was available for the till. Initial analysis of the pressure data indicated that there were minimal pressure losses with depth in the sand, except for the three monitoring well nests closest to the extraction well. The multi-level monitoring wells nearest to the horizontal well, ML9, ML15, and ML16, displayed larger pressure drawdowns in the shallower monitoring points, as would be expected for flow converging to a horizontal well located near the top of the sand. At distances greater than 30 m from the horizontal well, the multi-level points exhibited both increasing and decreasing pressures with depth, indicating that the vertical location of the horizontal well location was not as significant. Because flow in the sand is essentially horizontal towards the well, only one plan view section is plotted with all the data points from all layers included. The pressure drawdowns ranged from 0.005 %atm in the farthest monitoring well (SVE-5A) to 1.1 %atm in

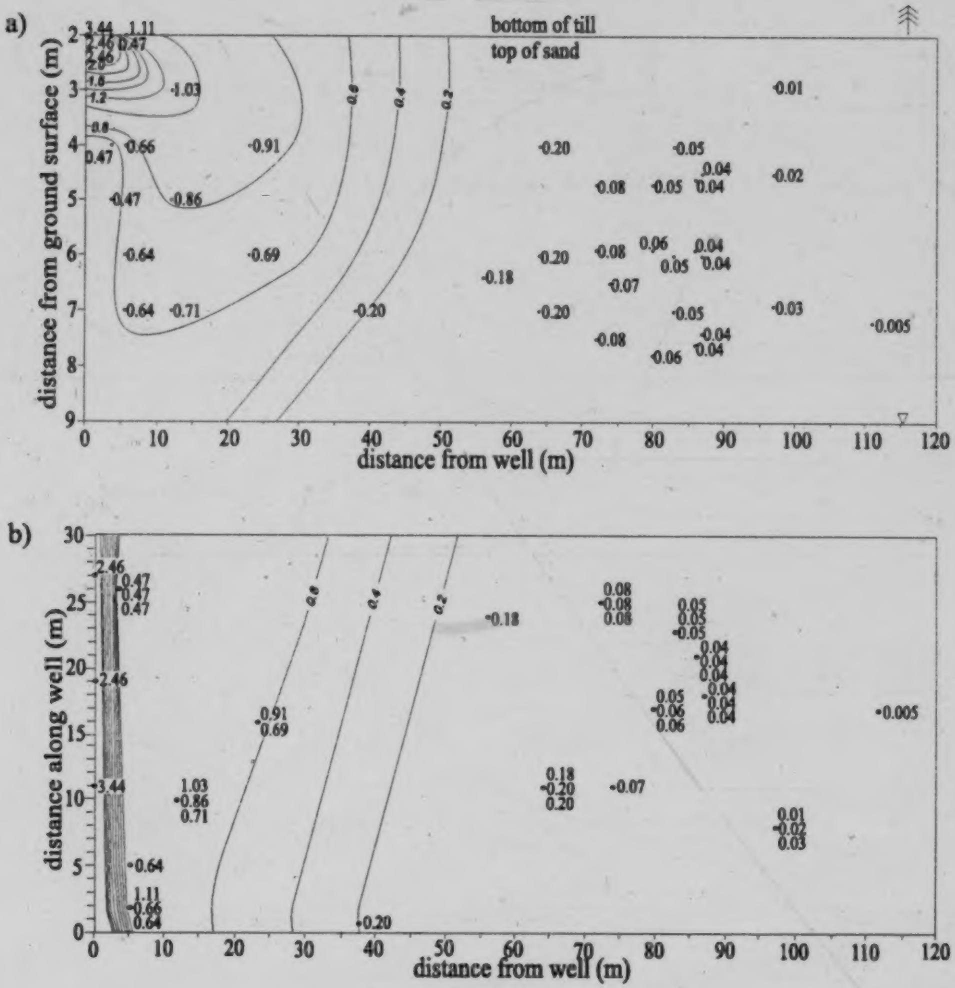

Figure 4.2: Field pressure drawdown distributions in the sand at Strachan. Contour interval = 0.2 to 2.0 %atm by 0.2 %atm. (a) Column cross-section. (b) Layer cross-section.

ML16, 5.5 m from the horizontal well. Although ML19 is perpendicularly closer to the horizontal well, ML16 is closest to the extraction blower and exhibited higher pressure drawdowns.

During the horizontal SVE test, a suction pressure of 8.4 %atm, with Q_{ex} equal to 170 L/s, was observed at the well head. The measured drawdowns at 10, 20 and 30 m along the horizontal well were 3.4, 2.5 and 2.5 %atm, respectively. This pressure loss along the extraction well was one reason why a three-dimensional flow model is necessary to represent the configuration of the horizontal well at Strachan. A two-dimensional analysis would not account for such well losses. Additionally, three-dimensional modelling is able to approximate the end effects present with horizontal wells, although pressure data was only available for the area extending perpendicular to the horizontal well. No data was available on the pressures beyond the lateral extent of the horizontal well, in the "end effects" zone. A knowledge of the pressures extending parallel to the well would have also provided information on the lateral anisotropy in k_x and k_y.

Grid Discretization and Boundary Conditions:

A grid was designed in AIR3D with the dimensions of 150 m in the x-direction and 300 m in the y-direction and 9.0 m in depth (z). To reduce computer CPU time and storage space, a half grid was used with a vertical symmetry boundary along the well axis (Figure 4.3). The well had a row, column and layer spacing of 0.1 m, 0.05 m (to account for symmetry boundary), and 0.1 m and was orientated along the y-axis. Moving away from the well, sequential cells spacing increased by a factor of 1.5 as recommended by Anderson and Woessner (1992). This resulted in a grid with 98 columns, 49 rows and 24 layers, for a total of 115 248 cells.

The symmetry boundary along which the horizontal well was located was specified as an impermeable boundary. The remaining three lateral boundaries were set to atmospheric pressure and placed far enough away from the extraction well such that greater than 96% of the air recharge to the system entered from the ground surface.

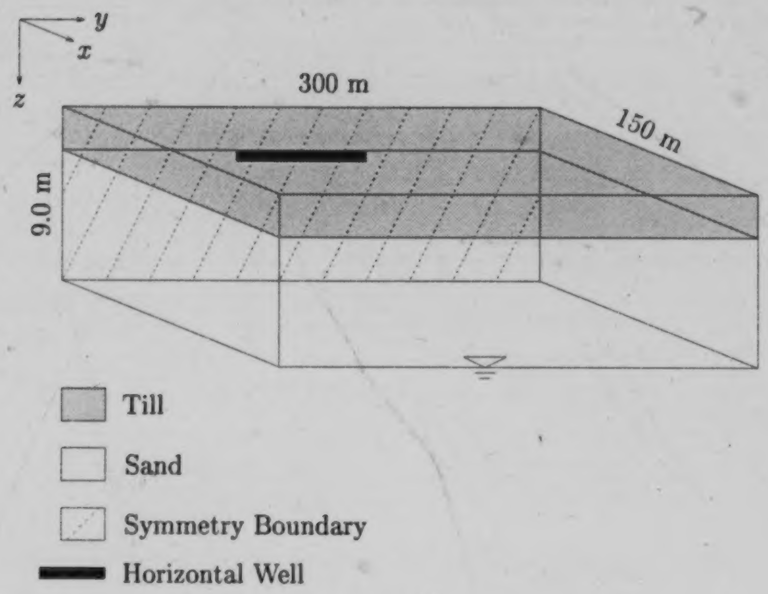

Figure 4.3: Conceptual model at Strachan *(not to scale)*.

The watertable was represented as an impermeable boundary and the ground surface was set to atmospheric pressure. Figure 4.4 illustrates the plan view, and two cross-sectional views of the boundary conditions.

Well Representation:

As discussed in Chapter 2, a horizontal well can be represented in a number of different ways within a numerical model. The method utilized for the AIR3D modelling was to assign the well an effective permeability and constrain the first node of the well to the pressure observed in the field test. The well permeability was based on equations for turbulent and laminar flow in a pipe and Darcy's law, as discussed in Chapter 2. This method resulted in some pressure losses along the well as observed in the field (Armstrong *et al.*, 1995). The simulated and observed pressures within the well are plotted in Figure 4.5.

With Q_{ex} equal to 0.17 m^3/s and a well radius of 0.05 m, the well permeability at

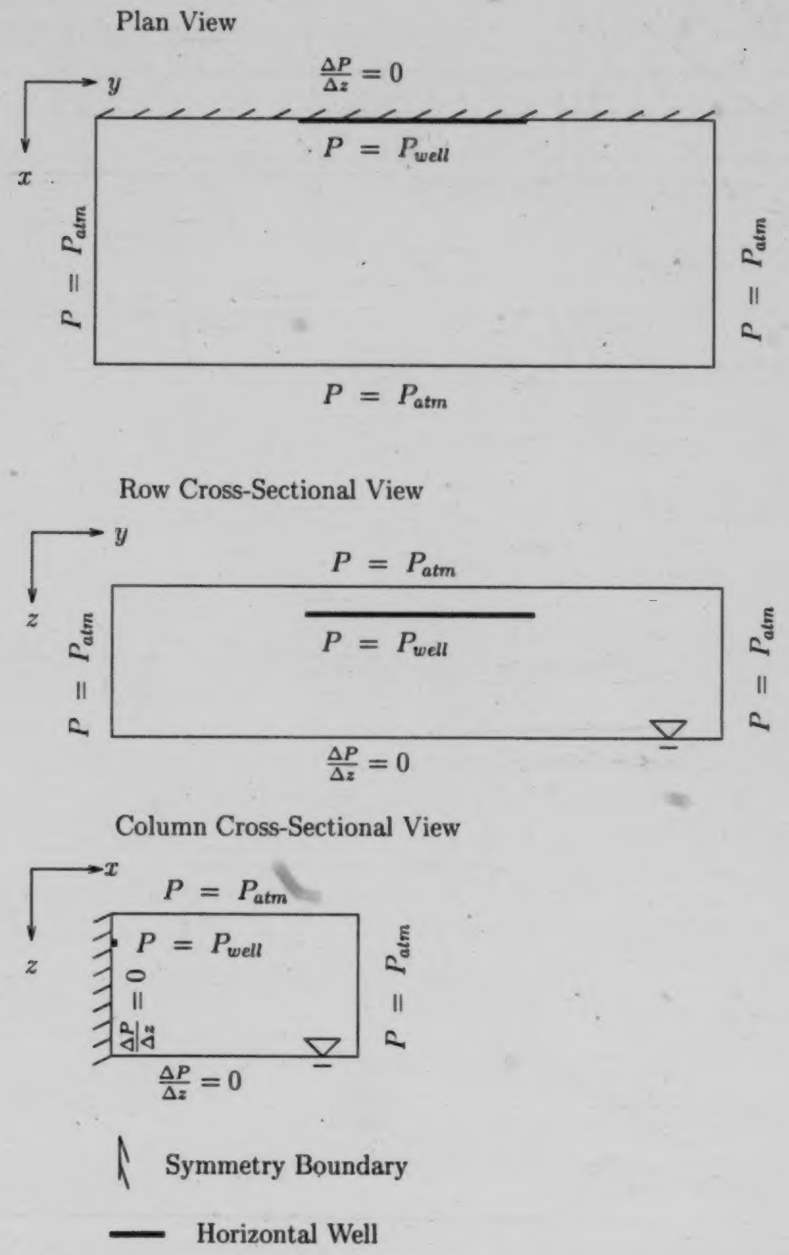

Plan View

Row Cross-Sectional View

Column Cross-Sectional View

$\frac{\Delta P}{\Delta z} = 0$
y
x
$P = P_{well}$
$P = P_{atm}$
$P = P_{atm}$
$P = P_{atm}$
y
z
$P = P_{atm}$
$P = P_{well}$
$P = P_{atm}$
$P = P_{atm}$
$\frac{\Delta P}{\Delta z} = 0$
x
z
$P = P_{atm}$
$P = P_{well}$
$\frac{\Delta P}{\Delta z} = 0$
$P = P_{atm}$
$\frac{\Delta P}{\Delta z} = 0$
Symmetry Boundary
Horizontal Well

Figure 4.4: Schematic illustration of the boundary conditions for horizontal well AIR3D simulations.

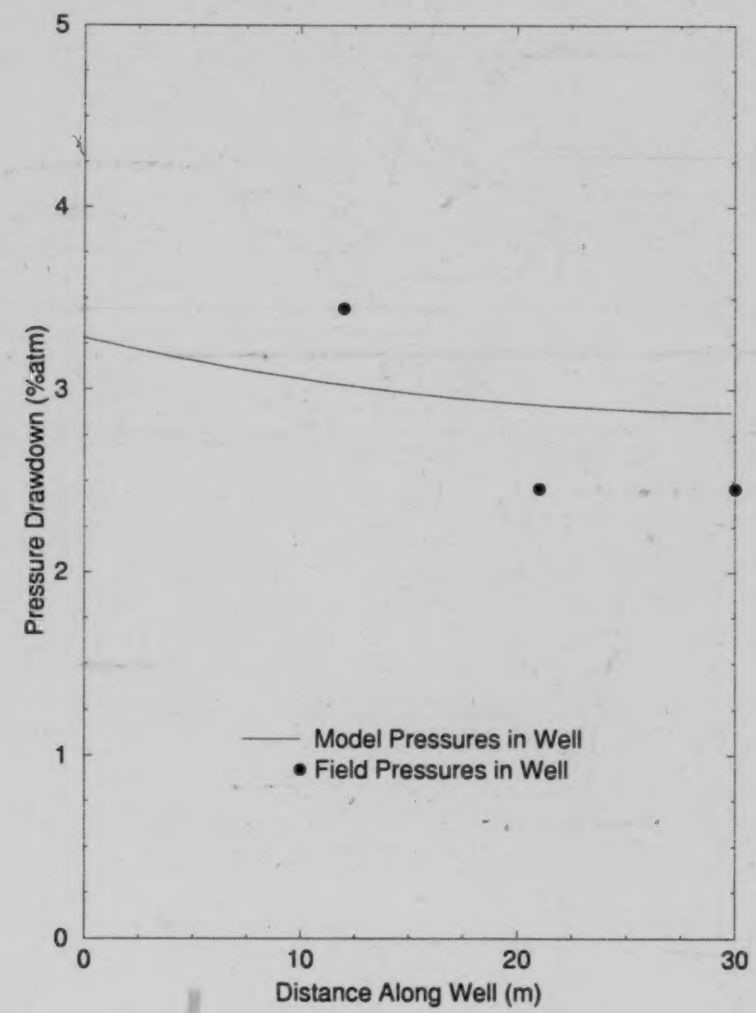

Figure 4.5: Model and field well pressures within the 30 m horizontal well at Strachan.

Strachan was estimated to vary from 7.2×10^{-6} m^2 for turbulent flow near the blower to 3.1×10^{-4} m^2 for laminar flow, with the transition zone between turbulent and laminar flow occurring at a permeability of 1.5×10^{-4} m^2. A single permeability of 1.1×10^{-5} m^2, 1.5 $\times10^5$ times larger than the surrounding sand, was selected as the uniform well permeability. The sensitivity of the well permeability to the extraction rate and flow solution is discussed later.

To model a horizontal well in AIR3D, a constrained pressure in the extraction well was required for input, with an extraction rate calculated as output. The observed Q_{ex} was 0.17 $\div$ 2 m^3/s, to account for a half grid. The pressure in the first cell of the extraction well was constrained to a P_D of 3.3 %atm and the till and sand permeabilities were adjusted until the best match for measured and modelled pressures was found. Although 3.3 %atm is smaller than the observed header pressure of 8.4 %atm, a smaller pressure was necessary in order for the simulated pressure in the extraction well to match the observed pressure, and for the simulated Q_{ex} to equal the observed Q_{ex}. Based on pipe flow theory, it is reasonable to assume that significant pressure losses occur between the end of the well screen and the header where pressure was measured.

4.1.6 AIR3D Horizontal Well Numerical Modelling Results

The horizontal SVE scenario was simulated using the three-dimensional air flow model AIR3D (Joss and Baehr, 1995) and the results were compared to field observations. As outlined previously, AIR3D has the advantage of accommodating important three-dimensional effects such as pressure losses along the horizontal well and end effects. Table 4.2 displays the input data required for the model and the previous section outlines the model discretization and boundary conditions.

As explained above, the permeabilities were adjusted until the calculated model Q_{ex} equaled the measured Q_{ex} and a good match was found between the simulated and observed pressures. With the amount of data available, approximately 40 pressure observation points, the permeabilities that resulted in the best match between

Parameter	Value
GRID:	
width of grid	300 m
length of grid	150 m
depth of grid	9 m
number of columns	98
number of rows	49
number of layers	24
AIR PROPERTIES:	
system pressure	1 atm
system temperature	283.15 K
air viscosity at system temp.	1.76×10^{-5} kg/m·s
GEOLOGICAL PROPERTIES:	
k	see Table 4.1
till depth	0 to 2 m
sand depth	2 to 9 m
watertable depth	9 m
air-filled porosity	0.25
WELL PROPERTIES:	
radius of extraction well	0.05 m
length of well	30 m
depth of well	2 to 2.1 m
P_D	3.3 %atm
Q_{ex} (for half grid)	0.085 m^3/s
well permeability	1.1×10^{-5} m^2

Table 4.2: Input parameters required for AIR3D modelling at Strachan.

Simulation	k^* (m^2)	P_D (%atm)	Q_{ex} ($\times 10^{-2}$ m^3/s)	Model	Constrained Variable
Case 1	k_{A1}	3.3	8.5	AIR3D	P_D
Case 2	k_{A2}	1.1	8.5	AIR3D	P_D
Case 3	k_{A2}	3.3	24	AIR3D	P_D
Case 4	k_{A3}	3.3	8.5	AIR3D	P_D
Case 5	k_{A1}	17.5	30.5	VapourT, axis.	Q_{ex}
Case 6	k_{A2}	5	30.5	VapourT, axis.	Q_{ex}
Case 7	k_{A1}	5.3	8.5	VapourT, cart.	Q_{ex}
Case 8	k_{A2}	1.4	8.5	VapourT, cart.	Q_{ex}
Case 9	k_{A3}	1.5	8.5	VapourT, cart.	Q_{ex}

Table 4.3: Input permeabilities, pressure drawdowns and extraction rates for different AIR3D and VapourT simulations for Strachan. k^* refer Table 4.1

field and model pressures were found. These permeabilities are listed as k_{A1} in Table 4.1 and the comparison between the simulated and measured field drawdowns is displayed in Figure 4.6. A total of four sets of data are plotted on Figure 4.6, listed in Table 4.3. Also the 1:1 best fit line is plotted for a perfect match between model and field drawdown pressures.

Two plots for k_{A2}, estimated by Armstrong *et al.* (1995) and Gilmour (1996), are shown on Figure 4.6. The first simulation, Case 2, constrained Q_{ex} to be 8.5 $\times 10^{-2}$ m^3/s, and through a series of trial and error, P_D of 1.1 %atm was necessary for the given Q_{ex} and k. The second simulation, Case 3, required P_D to equal 3.3 %atm, resulting in Q_{ex} of 2.4 $\times 10^{-1}$ m^3/s. Note that the incorrect extraction rate used by Armstrong *et al.* (1995) falls within the extraction rates listed in Table 4.3.

The plots indicate applying k_{A2}, estimated by Armstrong *et al.* (1995) and Gilmour (1996) from the vertical SVE test, resulted in underpredicted model drawdowns in the three-dimensional horizontal well air flow model. With Case 2, P_D of 1.1 %atm is obviously too low to match the field pressure data. However, a P_D of 3.3 %atm (Case 3) resulted in Q_{ex} equal to 2.4×10^{-1} m^3/s, significantly higher than the observed Q_{ex}. The near well pressures match the field drawdowns satisfactorily using k_{A2}, but as the distance from the well increases, the simulated pressure drawdowns are less than

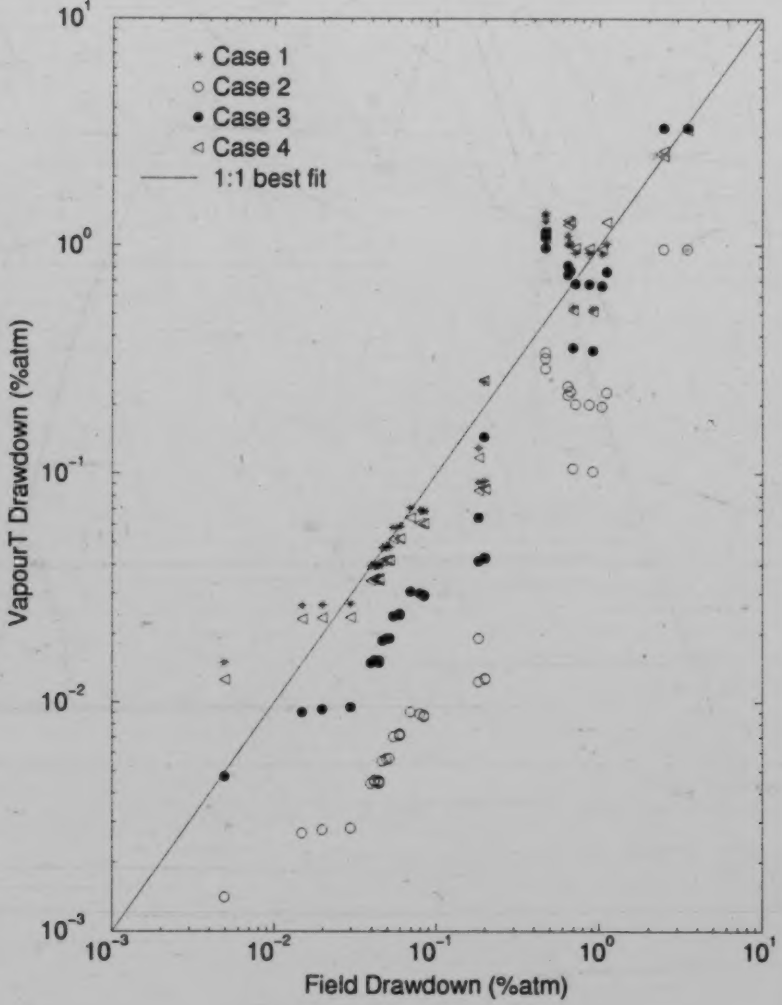

Figure 4.6: AIR3D 3D horizontal well model drawdowns vs. field drawdowns at Strachan. Log scale.

the field drawdowns. One explanation for this difference is the reduction in the ratio in the till to sand permeability compared to Case 1. The ratio between the till permeability and the sand permeability was found to be 1:70 for k_{A1}, compared to 1:30 for k_{A2}. As this ratio increases, the pressure drawdown distributions extend farther from the well. This effect is discussed further in Chapter 5.

An additional simulation, Case 4, was run, attempting to find an alternative permeability set, k_{A3}, with a till to sand ratio of 1:30, similar to k_{A2}, so Q_{ex} would equal 8.5×10^{-2} m^3/s for the given P_D of 3.3 %atm. The resulting till and sand permeabilities were 2.05×10^{-12} m^2 and 6.15×10^{-10} m^2 respectively. As illustrated in Figure 4.6, this combination resulted in close, but slightly underpredicted, model drawdowns.

With the amount of scatter found in the model versus field drawdowns in Figure 4.6, it was concluded that adding any y-directional and z-directional variation in the permeability was not justified without further evidence of anisotropy, therefore the till and sand were considered isotropic. Chapter 5 will further investigate the effect of including anisotropy.

The solution to the permeabilities is not unique as different combination of Q_{ex}, P_D, and k may yield similar flow solutions. This is another possible explanation for the different estimates of k_{A1} and k_{A2}. By only having a good estimate of the field Q_{ex}, various combinations of P_D and permeabilities will result in the required extraction rate, but only a few combinations will have a good fit between model and field drawdowns.

Another explanation for the difference between k_{A1} and k_{A2} is that k_{A2} estimated the permeability in the vicinity of SVE-1, compared to k_{A1} which was the best fit for the permeability in the area of the horizontal well and it is possible that the permeabilities vary between the two locations. As well, the horizontal well SVE test was conducted at a different P_D and Q_{ex} than the vertical SVE and at a different time of the year which could result in different air-filled porosities and permeabilities.

4.1.7 VapourT Numerical Modelling Results

A second method to evaluate the permeabilities was to use the two-dimensional axisymmetric model VapourT to simulate the vertical SVE test simulated by Gilmour (1996) and to compare the simulated pressures to pressures measured in the field during the vertical SVE test. Two simulations were completed applying k_{A1} and k_{A2}. The extraction rate was constrained to 3.05×10^{-1} m^3/s in the vertical well with resulting pressure drawdowns in the midpoint of the 3 m screened well calculated to be 17.5 %atm for Case 5 and 5.0 %atm for Case 6. The results illustrated in Figure 4.7 indicate that k_{A1} overpredicts the vertical well SVE test.

Finally, a VapourT simulation for two-dimensional flow to the horizontal well in cartesian coordinates was completed, neglecting all end effects. As illustrated in Figure 4.8, utilizing k_{A1} (Case 7) yields model drawdowns greater than the field drawdowns and applying k_{A2} and k_{A3} (Cases 8 and 9) resulted in underpredicted model drawdowns. This demonstrates the difference between the two-dimensional VapourT model and the three-dimensional AIR3D model. Ignoring the flow component beyond the ends of the well in VapourT created greater model drawdowns than three-dimensional flow in AIR3D. A comparison between two- and three-dimensional flow is further explored in Chapter 5.

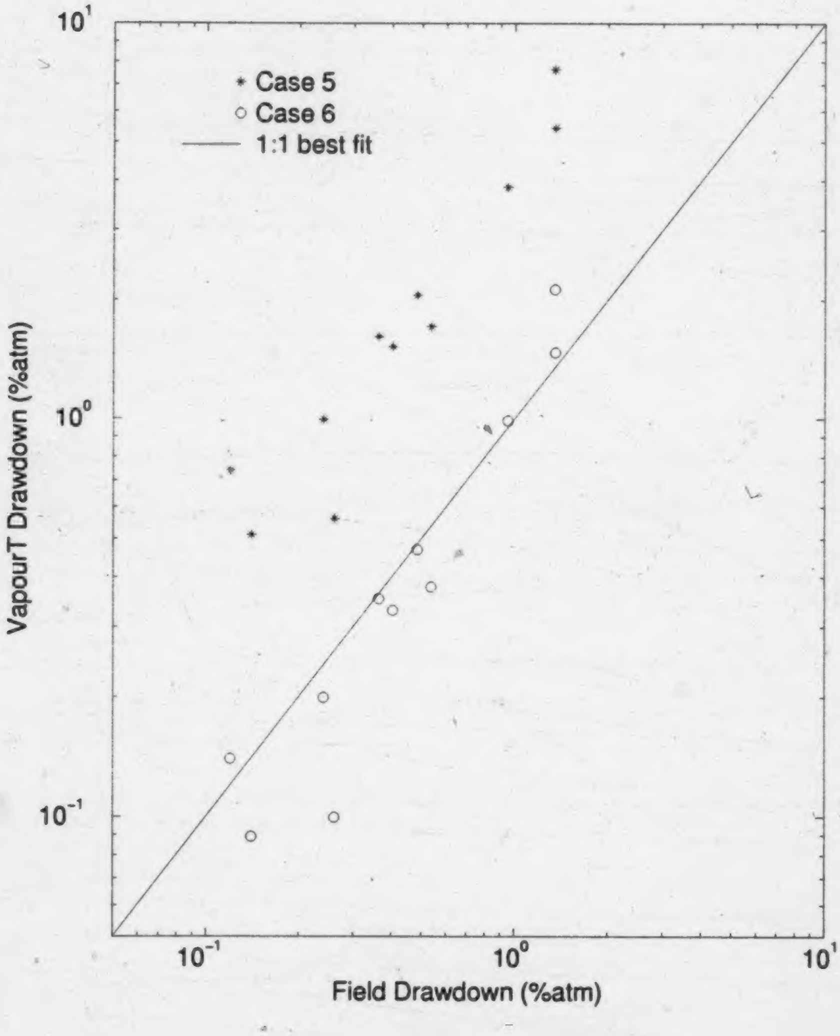

Figure 4.7: VapourT 2D axisymmetric vertical well model drawdowns vs. field drawdowns at Strachan.

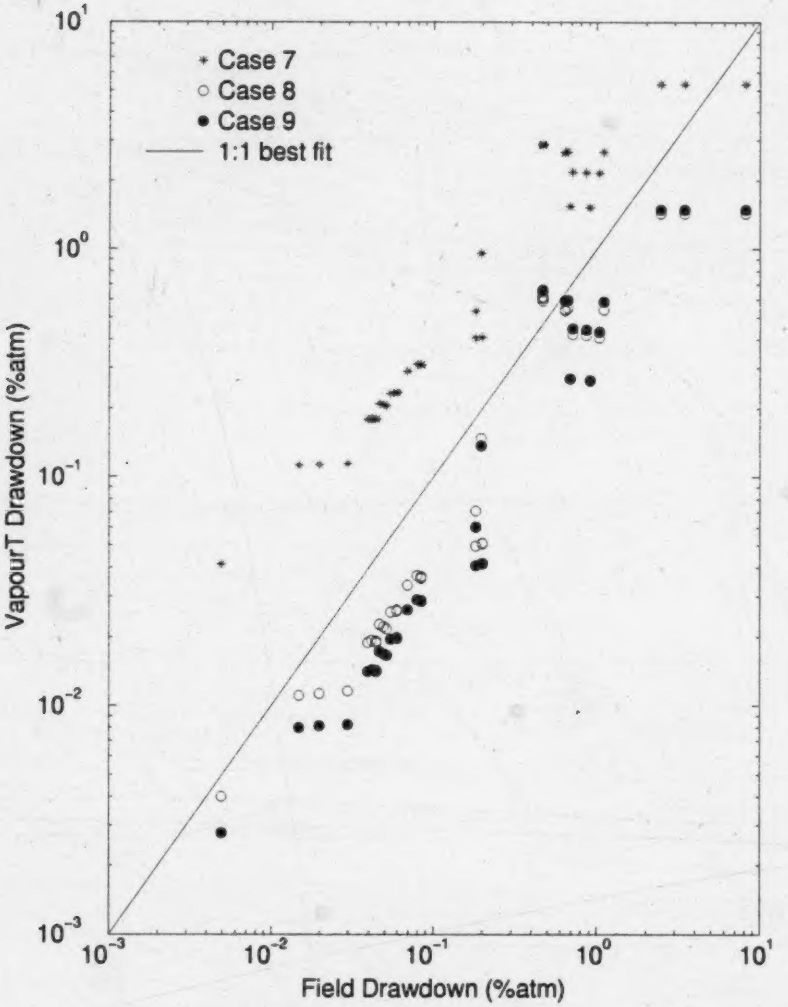

Figure 4.8: VapourT 2D cartesian coordinates horizontal well model drawdowns vs. field drawdowns at Strachan.

4.2 Site B

Site B is a gas plant located on the plains in Western Canada. Komex was contracted to monitor and design a remediation system to remove hydrocarbons from the unsaturated subsurface. A number of pilot tests conducted at Site B during 1991 and 1992 investigated the feasibility of vertical and horizontal SVE as a remediation method and the results of the activities were summarized by Komex (1994c) and Armstrong *et al.* (1995). These investigations indicated the contamination in the subsurface at the site was volatile and thus SVE was selected as a promising technique.

Due to the confidentiality agreement between Komex and the site owners, the site is known only as Site B and a limited amount of site information was available. Despite this limitation, the contrast in the geology and in the horizontal well SVE systems between Strachan and Site B made modelling this site essential in the analysis of air flow to horizontal well SVE systems.

4.2.1 Geology and Hydrogeology

The surficial geology of the area consists of a 7 m thick layer of silty sand fining downwards to sandy silt, of which approximately 5 m is unsaturated (Armstrong *et al.*, 1995). Grain size analyses showed that 100% of the porous medium is finer than fine sand to silt (0.2 mm), 50% finer than the sand/silt divide (0.0625 mm) and 10 to 15% finer than clay size. Freeze and Cherry (1979) provide the following approximate permeability values for various materials: silty sand 10^{-14} to 10^{-10} m^2; silt 10^{-16} to 10^{-12} m^2; and glacial till 10^{-19} to 10^{-13} m^2. Below the Quaternary silt deposits lies clay till of unknown thickness. The watertable is known to fluctuate approximately 1 m seasonally and groundwater flows from south to north (Armstrong *et al.*, 1995).

4.2.2 Contamination

Above the watertable, a layer of liquid condensate covers an area of approximately 40 000 m^2. Up to 2 m of free-phase product has been observed in piezometers at the site (Armstrong *et al.*, 1995). The horizontal well is located above a portion of the free phase condensate and dissolved phase plume as illustrated in Figure 4.9.

4.2.3 Vertical and Horizontal Well Installation and Configuration

Horizontal wells were considered at this site for two reasons. Tests conducted with vertical wells showed that the radius of influence is small, and thus many vertical wells would be needed to cover the extensive area of contamination. Furthermore, the site has many surface structures such as storage tanks, roads, railroad tracks and fences and it was thought that the horizontal wells could run beneath these structures, minimizing the surface piping and providing a longer screened interval per well (Armstrong *et al.*, 1995).

Three horizontal wells were installed using two different drilling techniques. Initially, a hammering technique was utilized to install the horizontal wells, but difficulties with the drill bit catching on the driving rod and lack of steering control forced the contractor to abandon this technique (Komex, 1994c). These attempts resulted in two horizontal wells (HW-1 and HW-2) with screen lengths of approximately 20 m. The third horizontal well (HW-3) was directionally drilled using a jetting fluid with rotational and pushing force on the drill bit, providing adequate steering control. The 80 m long well, constructed with 0.075 m (3 in) diameter PVC pipe with a screen length of 60 m, was positioned at a depth of 3.5 m (Komex, 1994c). The well head is located at the north end of HW-3, with the screened portion of the well beginning 10 m from the well head. In addition, two trenches, an interceptor trench and two sets of vertical extraction wells were installed. The location of the horizontal and vertical SVE wells, trenches and monitoring wells are shown in Figure 4.9.

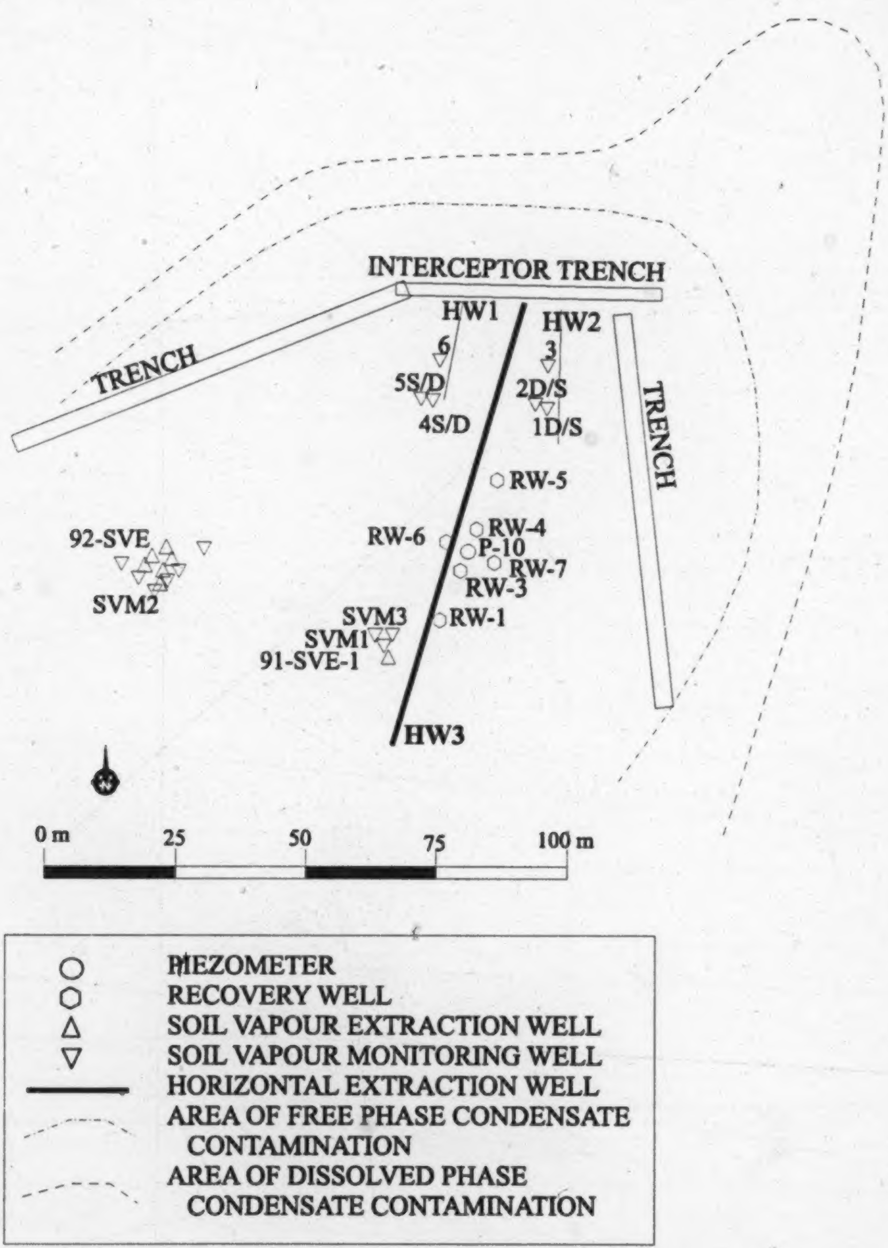
INTERCEPTOR TRENCH
TRENCH
TRENCH
HW1
HW2
HW3
6
5S/D
4S/D
3
2D/S
1D/S
RW-5
RW-4
RW-6
P-10
RW-7
RW-3
RW-1
92-SVE
SVM2
SVM3
SVM1
91-SVE-1
0 m
25
50
75
100 m
PIEZOMETER
RECOVERY WELL
SOIL VAPOUR EXTRACTION WELL
SOIL VAPOUR MONITORING WELL
HORIZONTAL EXTRACTION WELL
AREA OF FREE PHASE CONDENSATE CONTAMINATION
AREA OF DISSOLVED PHASE CONDENSATE CONTAMINATION

Figure 4.9: Site map at Site B (Komex, 1994c).

4.2.4 Previous Field Activities and Modelling Results

SVE testing was conducted to evaluate the rate of mass extraction, to assess the applicability of bioventing and to estimate the pressure distribution around the horizontal well. Three horizontal SVE tests were conducted between 29 September and 3 October 1994. The flowrates during the tests were between 0.11 m^3/s and 0.15 m^3/s and steady-state conditions reached were within hours (Komex, 1994c). Pressure drawdowns were recorded in 22 SVE vertical wells, recovery wells and piezometers.

Short-term mass extraction tests yielded removal rates of approximately 220 kg/d for HW-1, 1380 kg/d for HW-2 and 600 kg/d for HW-3. Based on these removal rates it was concluded that SVE can successfully remove contaminants from the subsurface on short time scales (Komex, 1994c). Long-term tests would be necessary to determine to what extent kinetic effects might lead to decreased removal rates. It was estimated that approximately 5 kg of hydrocarbons were removed daily through enhanced biodegradation.

Two-dimensional VapourT modelling by Armstrong *et al.* (1995) utilizing cartesian coordinates yielded permeabilities of 1.5×10^{-11} m^2 for the till in the upper 3.5 m and 1.9×10^{-12} m^2 for the till approaching the capillary fringe, listed as k_{B2} in Table 4.4. VapourT was then applied to estimate pressures at different locations in order to determine the effective radius of influence, defined by Armstrong *et al.* (1995) to be the radius at a given depth in which the pressure drawdown is 25 Pa (0.025 %atm) or 1 in of water. Preliminary results show the effective radius of influence for the horizontal well at Site B was approximately 12 m at the elevation of the horizontal well, compared to 4.5 m for a vertical well. From this, it was estimated that at this site one 60 m horizontal well was equivalent to approximately 22 vertical wells (Armstrong *et al.*, 1995). Because of the small radius of influence of vertical wells and the amount of surface infrastructure, SVE with vertical wells at Site B was judged infeasible and the remaining investigations focused on SVE using horizontal wells.

The same error that occurred at Strachan with the flux for a full grid being applied

Simulation	ID	k_{till1} (m^2)	k_{till2} (m^2)
3D simulations (AIR3D)	k_{B1}	6.0×10^{-12}	1.0×10^{-12}
2D cartesian simulations (VapourT)	k_{B2}	1.53×10^{-11}	1.9×10^{-12}

Table 4.4: Till permeabilities selected for different modelling simulations at Site B.

instead of that a half grid also occurred with Site B VapourT two-dimensional cartesian coordinates model by Armstrong *et al.* (1995). Therefore, all the permeabilities and radii of influence were considered questionable.

4.2.5 Numerical Model Set-up

Only three-dimensional AIR3D simulations were completed for Site B in this study because only data was available from the horizontal SVE tests. The input and observation data utilized in the model was obtained from the three horizontal SVE tests conducted between 29 September and 3 October 1994, including extraction rates and pressures in 22 surrounding monitoring wells. The well head drawdown was estimated to be between 9 %atm to 15 %atm, with Q_{ex} between 0.11 m^3/s and 0.15 m^3/s (Komex, 1994c). Since steady-state conditions were reached rapidly, only steady-state air flow was simulated.

Pressure Drawdown Analysis from Horizontal SVE Test

Figure 4.10 displays a column cross-section of the contoured field pressure drawdowns. Due to the fact that there were no pressure observations within the well and because of the lateral placement of the monitoring points, it was difficult to estimate head losses with distance along the well. Therefore, only one column cross-section is presented. The largest pressure drawdown, 2.6 %atm, was observed in SVE-1, 1 m from the well, 60 m along the well from the well head and at an unknown depth. In comparison,

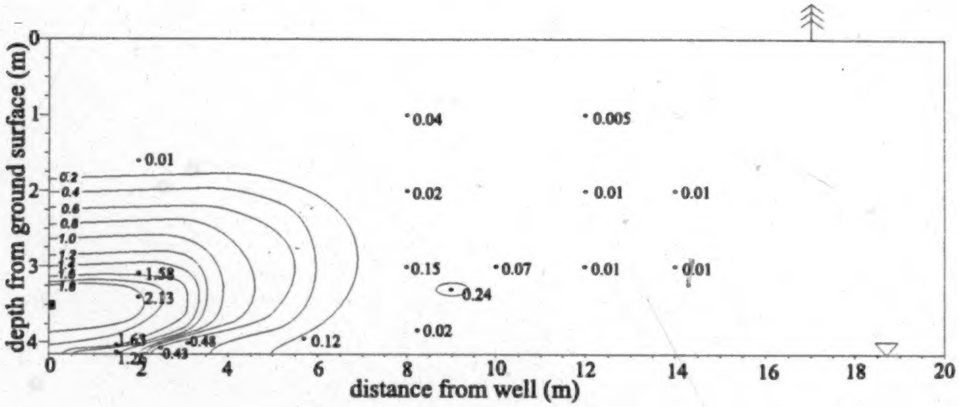

Figure 4.10: Field pressure drawdown distributions at Site B. Column cross-section. Contour interval = 0.2 to 2.0 %atm by 0.2 %atm.

SVM-1 located the same distance along the well, but approximately 2 m from the well at a depth of 3.4 m had a drawdown of 2.1 %atm, while RW-6, 39 m along the well, 1.5 m from the well at a depth of 4.13 m, only had a drawdown of 1.3 %atm. These differences may be a result of a change in permeability with depth or other heterogeneities in the till. Additionally, the accuracy of the depths and distances to the horizontal well for some of the monitoring points were somewhat suspect.

As the distance from the well increased, the pressure dropped quickly. At RW-5 located at approximately the same depth as the horizontal extraction well, only 5.7 m from the well, the pressure drawdown was only 0.12 %atm, demonstrating the rapid decrease in pressure drawdowns as the distance from the extraction well increased.

It can be concluded that the pressure drawdowns created by the SVE test decreased rapidly with distance from the well. Vertically, the largest drawdowns were located at the depth of the horizontal extraction well. These observations were a result of the absence of a confining layer at the ground surface and the depth of the extraction well. The shape of the pressure contours can be described generally as cylindrical with the axis of the cylinder equivalent to the horizontal well. Flow is generally from ground surface down towards to the well. Armstrong *et al.* (1995) concluded that heterogeneities existed in the subsurface because of the poor correspondence between field pressure measurements and distance from the extraction well.

Grid Discretization and Boundary Conditions

The small radius of influence determined through initial investigations resulted in a markedly smaller domain size than that of the Strachan simulations. The width and length of the grid were 100 m and 20 m respectively, with a depth of 4.1 m. Similar to Strachan, a half grid was utilized to save computer time and space. The domain was discretized into 124 columns, 27 rows and 25 layers for a total of 83 700 cells. The horizontal well was assumed to have a radius of 0.05 m and a length of 60 m, located at a depth of 3.5 m.

A distance of 20 m from the horizontal well was determined to be far enough away such that greater than 99% of the recharge air entered from the ground surface. All boundary conditions were identical to that of Strachan, as illustrated in Figure 4.4.

Well Representation

No pressures were monitored within the extraction well during the SVE test, so it was difficult to estimate the pressure losses that would be present in the 60 m long extraction well. The extraction pressure was chosen to be 7.2 %atm. This value is less than the 9 to 15 %atm estimated at the well head, but losses were likely to occur between the well head and the well screen. Similar to Strachan, calculations based on the well radius and extraction rate were conducted and the well k was estimated to vary from 7.9×10^{-6} m^2 to 3.1×10^{-4} m^2. A permeability of 6.0×10^{-6} m^2 was selected as the well permeability. In Chapter 5, the effect of different well permeabilities on the flow solution is examined.

4.2.6 Numerical Modelling Results

AIR3D was capable of simulating end effects and pressure losses along the well. The main difficulty modelling this site was that to predict permeabilities based on observed field data, both P_D and Q_{ex} were required. Reliable values of Q_{ex} were provided with the field data from Komex, but only an estimate of P_D was available. Thus, different combinations of k and P_D could result in matching field and model pressures and a correct value of Q_{ex}.

All the input data required for AIR3D is listed in Table 4.5 and the boundary conditions and grid discretization were discussed previously. Similar to Strachan, the permeabilities were adjusted until the best fit between the field and model pressures occurred and Q_{ex} was equal to 6.0×10^{-2} m^3/s. The permeabilities selected as the best fit were 6.0×10^{-12} m^2 for the till between ground surface and 3.5 m below ground surface and 1.0×10^{-12} m^2 for the till between a depth of 3.5 m and the watertable, listed as k_{B1} on Table 4.4. Simulations with these permeabilities, k_{B1}, as well as the k_{B2} estimated by Armstrong *et al.* (1995), outlined in Table 4.6, are plotted and compared on Figure 4.11.

In previous simulations (Armstrong *et al.*, 1995), the permeability set k_{B2} was found to produce the best match between field and model data using two-dimensional cartesian coordinates in VapourT. For the AIR3D modelling, two simulations were completed with k_{B2} permeability set: 1) Case 11, in which the pressure drawdown was adjusted until Q_{ex} equalled 6.0×10^{-2} m^3/s; and 2) Case 12, in which P_D was constrained to 7.2 %atm, resulting a higher Q_{ex}. The incorrect extraction rate used in previous simulations by Armstrong *et al.* (1995) was within the range listed in Table 4.6.

There is a large amount of scatter in Figure 4.11. Typically the model pressures matched the field pressures at larger drawdowns, but as the pressures decreased, the model drawdowns tend to underpredict the field drawdowns. The pressure distribution in Case 10 and Case 12 are nearly identical. This is due to the extraction well pressure being the same. With a well permeability of 6.0×10^{-6} m^2, the model

Parameter	Value
GRID:	
length of grid	100 m
width of grid	20 m
depth of grid	4.1 m
number of columns	124
number of rows	27
number of layers	25
AIR PROPERTIES:	
system pressure	1 atm
system temperature	283.15 K
air viscosity air at system temp.	1.76×10^{-5} kg/m·s
GEOLOGICAL PROPERTIES:	
k	see Table 4.4
till 1 depth	0 to 3.5 m bgs:
till 2 depth	3.5 to 4.1 m bgs:
watertable depth	4.1 m
air filled porosity	0.25
WELL PROPERTIES:	
radius of extraction well	0.05 m
length of well	60 m
location of well	3.4 to 3.5 m bgs
P_D	7.2 %atm
Q_{ex} (for half grid)	6.0×10^{-2} m^3/s
well permeability	6.0×10^{-6} m^2

Table 4.5: Input parameters required for AIR3D modelling at Site B.

Simulation	k^* (m^2)	P_D (%atm)	Q_{ex} ($\times10^{-2}$ m^3/s)
Case 10	k_{B1}	7.2	6.0
Case 11	k_{B2}	3.4	6.0
Case 12	k_{B2}	7.2	13

Table 4.6: Input permeabilities, pressure drawdowns and extraction rates for different AIR3D simulations for Site B. k^* refer Table 4.4

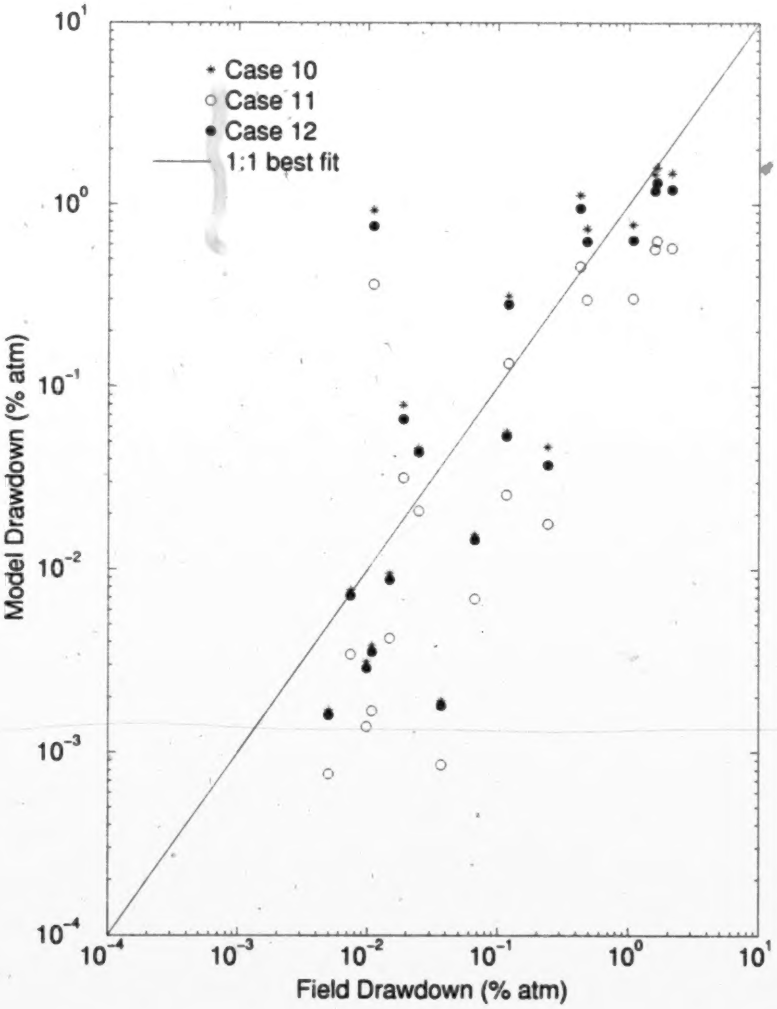

Figure 4.11: AIR3D 3D horizontal well model drawdowns vs. field drawdowns at Site B. Log scale.

predicted a drop in pressure along the 60 m long horizontal well of approximately 1 %atm as illustrated in Figure 4.12.

The permeabilities at Site B were estimated, although the input data uncertainty resulted in a large uncertainty with the permeability estimates. With lack of information regarding well pressure losses, and the possible presence of heterogeneity at the site, it was determined that focusing the modelling on the sensitivity of different parameters on the air flow solution would be more beneficial.

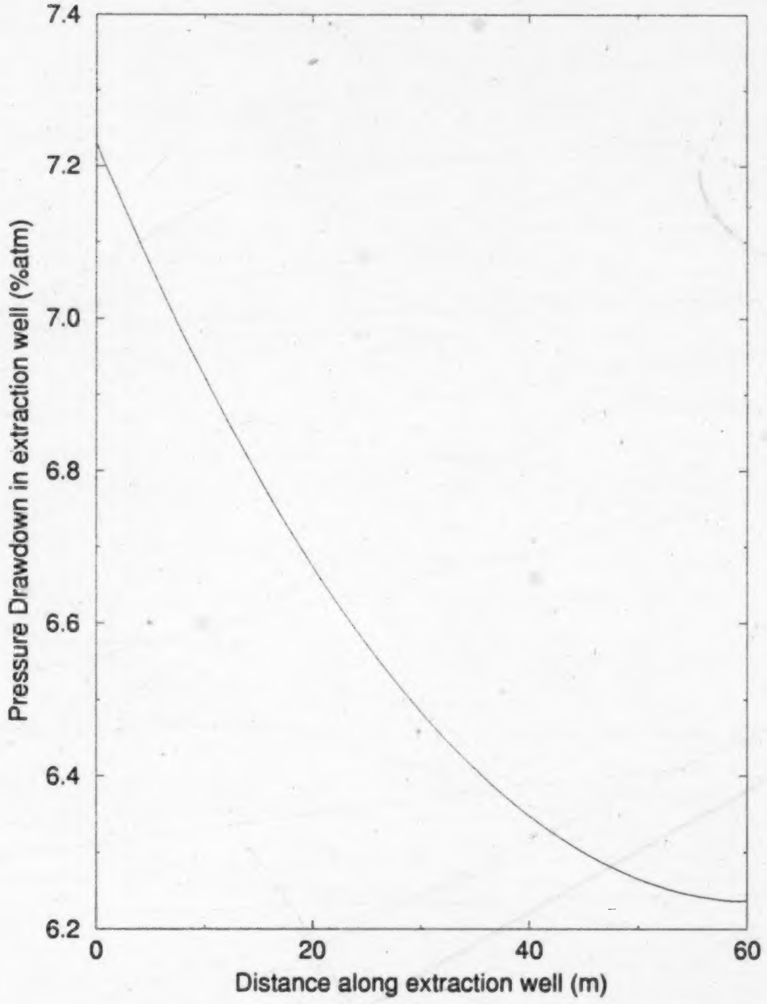

Figure 4.12: Model well pressures within the 60 m horizontal well at Site B.

Chapter 5

Generic Sensitivity Analysis

A sensitivity analysis was conducted to determine the impact of different parameters on the air flow solutions in both two- and three-dimensions. The results of the sensitivity analysis include an estimate of the range of pressure distributions and flowrates, as well as providing insight into which parameters should be further investigated with laboratory and/or field programs.

5.1 Approach

The aim of the sensitivity analysis was to change key system parameters and observe the change in: 1) pressure distributions; 2) the time for various particles within the domain to reach the well; 3) the flowpaths taken by the particles; and 4) the volume of porous media influenced in a given time, t, (V_t^*).

AIR3D (Joss and Baehr, 1995) was used to solve for pressure distributions and the results were compared to Base Case contours. Travel times and flowpaths were determined by placing particles throughout the domain and running Forward Particle Tracking within MODPATH (Pollock, 1989). Finally, the Backward Particle Tracking option in MODPATH was utilized to calculate V_t^* for given time periods. Particles were located in the cells adjacent to the extraction well(s). For each particle, MODPATH was used to calculate the flowpath of the particle based on the pressure distribution. Along the flowpath, a time was calculated for each cell that the particle passed through. The further the cell was from the well, the longer it would take a particle located in the cell to reach the extraction well. A Fortran program was written to take the output from MODPATH, determine which cells had particles with travel times less than a specified time, then sum the total volume. This provides an estimate of the volume of porous media containing air that reaches the extraction well in the given time period. V_t^* is similar to the definition of maximum degree of remediation provided by Johnson and Ettinger (1994), which relates the volume of soil in contact with contaminated soil. This method is preferred over estimating the radius of influence in that it can accommodate non-circular shapes created by multiple vertical wells or horizontal wells, and represents velocities rather than a defined pressure drawdown.

The sensitivity analysis focused on identifying parameters that control the pressure distribution, flowpath, travel time to the well, and V_t^*. The parameters varied were: 1) geological parameters, such as permeability, presence of a cover and location of the watertable; 2) well characteristics, including type of well (i.e., horizontal vs. vertical), number, location, length, permeability, and pressure; and 3) model design, comprising grid size, discretization and dimensionality.

Two generic Base Cases were selected for the sensitivity analysis, similar to the geological properties at Strachan and Site B. The two cases have unique site characteristics: Strachan is comprised of a sand-and-gravel unsaturated zone, herein referred to as the sand unit, capped with a lower permeability glacial till unit, while Site B consists of only a shallow till unit. The well placement and well length are also different at the two sites.

The geological properties of Base Case A were based on the Strachan site, with parameters listed in Table 5.1. The grid dimensions were 150 m (symmetry boundary) by 300 m by 9 m in depth discretized into 49 rows, 98 columns and 24 layers. The geology consisted of a 2 m till unit with isotropic permeabilities of 1.0×10^{-12} m^2 overlying a sand unit with a permeability of 7.0×10^{-11} m^2; the watertable was located at a depth of 9 m. The 30 m horizontal well, located at the top of the sand at a

Parameter	Value
grid dimensions	150 m × 300 m × 9 m
number of cells	49 row, 98 columns, 24 layers
till permeability (0-2 m)	1×10^{-12} m^2
sand permeability (2-9 m)	7×10^{-11} m^2
watertable depth	9 m
till and sand air-filled porosity	0.25
well pressure	96.7 %atm (P_D=3.3 %atm)
well permeability	1.1×10^{-5} m^2
cross-sectional area of well (half-well)	5.0×10^{-3} m^2
well depth	2 to 2.1 m
well length	30 m

Table 5.1: Parameters for Base Case A

Parameter	Value
grid dimensions	20 m × 100 m × 4.1 m
number of cells	27 rows, 124 columns, 25 layers
permeability till$_1$ (0-3.5 m)	6×10^{-12} m^2
permeability till$_2$ (3.5-4.1 m)	1×10^{-12} m^2
watertable depth	4.1 m
till and sand air-filled porosity	0.25
well pressure	93.4 %atm (P_D=6.6 %atm)
well permeability	6.0×10^{-6} m^2
cross-sectional area of well (half-well)	5.0×10^{-3} m^2
well depth	3.4 to 3.5 m
well length	60 m

Table 5.2: Parameters for Base Case B

depth of 2.0 to 2.1 m, was represented with cells having a permeability 1.1×10^{-5} m^2. The cross-sectional dimensions of the well were 0.1 m by 0.05 m to account for the symmetry boundary. The first cell of the well was constrained to a pressure of 96.7 %atm, a drawdown of 3.3 %atm. The boundary conditions were the same as those specified in Chapter 4.

Base Case B had similar characteristics to that of Site B, with a grid 20 m (symmetry boundary) by 100 m by 4.1 m deep, discretized into 27 rows, 124 columns and 25 layers. The Base Case parameters for Case B are listed in Table 5.2. The subsurface was represented by a 3.5 m thick till unit with an estimated isotropic permeability of 6.0×10^{-12} m^2 overlying 0.6 m of till with an estimated permeability of 1.0×10^{-12} m^2. The well, located at a depth of 3.4 to 3.5 m, had cross-sectional dimensions of 0.1 m by 0.05 m to account for the symmetry boundary and a permeability of 6.0×10^{-6} m^2. The pressure in the first cell of the well was constrained to 93.4 %atm, a drawdown of 6.6 %atm.

5.2 Method of Presenting Results

As explained in Section 5.1, four different factors were used as comparison measures in the sensitivity analysis: pressure distributions, travel time and flowpath to well, and V_t^*. Figure 5.1 portrays the cross-sections used in displaying the pressure contours, all of which bisect the horizontal extraction well. The column cross-section was through the middle of the horizontal well, and, although this might not bisect the vertical wells if multiple vertical wells were simulated, it illustrates the cross-sectional view through the middle of a hypothetical contaminant plume.

To compare pressure distributions, the sensitivity analyses were compared to the Base Case by plotting the 0.5 %atm contour and observing the differences in shape and magnitude. This contour was selected because it was far enough from the far lateral boundary that it was not influenced by the boundary conditions, yet it was not so close to the well that it was influenced by near-well effects. Additionally, the flowpaths taken by a particle, placed 30 m and 5 m perpendicular to the middle of the

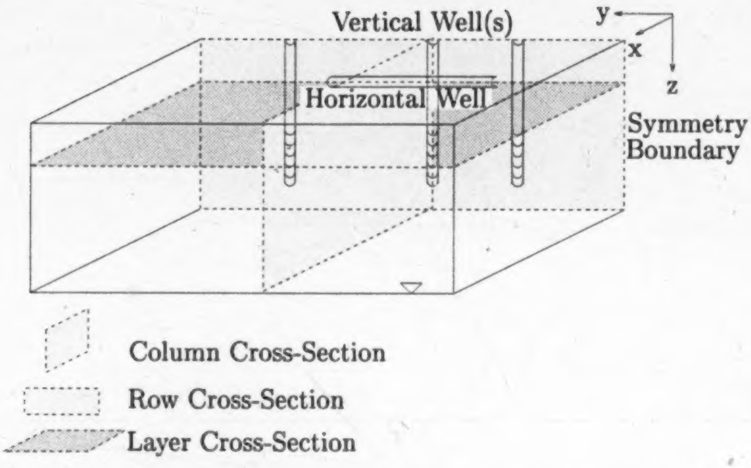

Figure 5.1: Location of cross-sections for sensitivity analysis figures.

well at ground surface for Case A and Case B respectively, were also plotted on the pressure distribution plots. These distances were selected for the same reasons as the 0.5 %atm contour selection. Note that on most plots the scales have been exaggerated and the domains truncated for ease of visualization. Results for travel time to the well, along with calculated extraction rates, are listed in Tables 5.3 and 5.4 for Case A and, later, in Table 5.5 for Case B. Also provided in Tables 5.3, 5.4 and 5.5 are V_t^* after 5 days of extraction for Case A and 0.5 days for Case B. Again, these times were chosen in order to find a V_t^* that was not adversely influenced by the boundary conditions. All extraction rates and volumes are for the half grids simulated; the actual extraction rates and volumes would be twice the value given.

5.3 Base Case A

The pressure drawdown distributions in column, row and layer cross-sections illustrated in Figure 5.1 for Base Case A are shown in Figure 5.2, with a contour interval of 0.01 to 0.1 %atm by 0.01 %atm, 0.1 to 1.0 %atm by 0.1 %atm and 1.0 to 3.0 %atm by 1.0 %atm. The dotted line, 0.5 %atm, was the contour selected to be

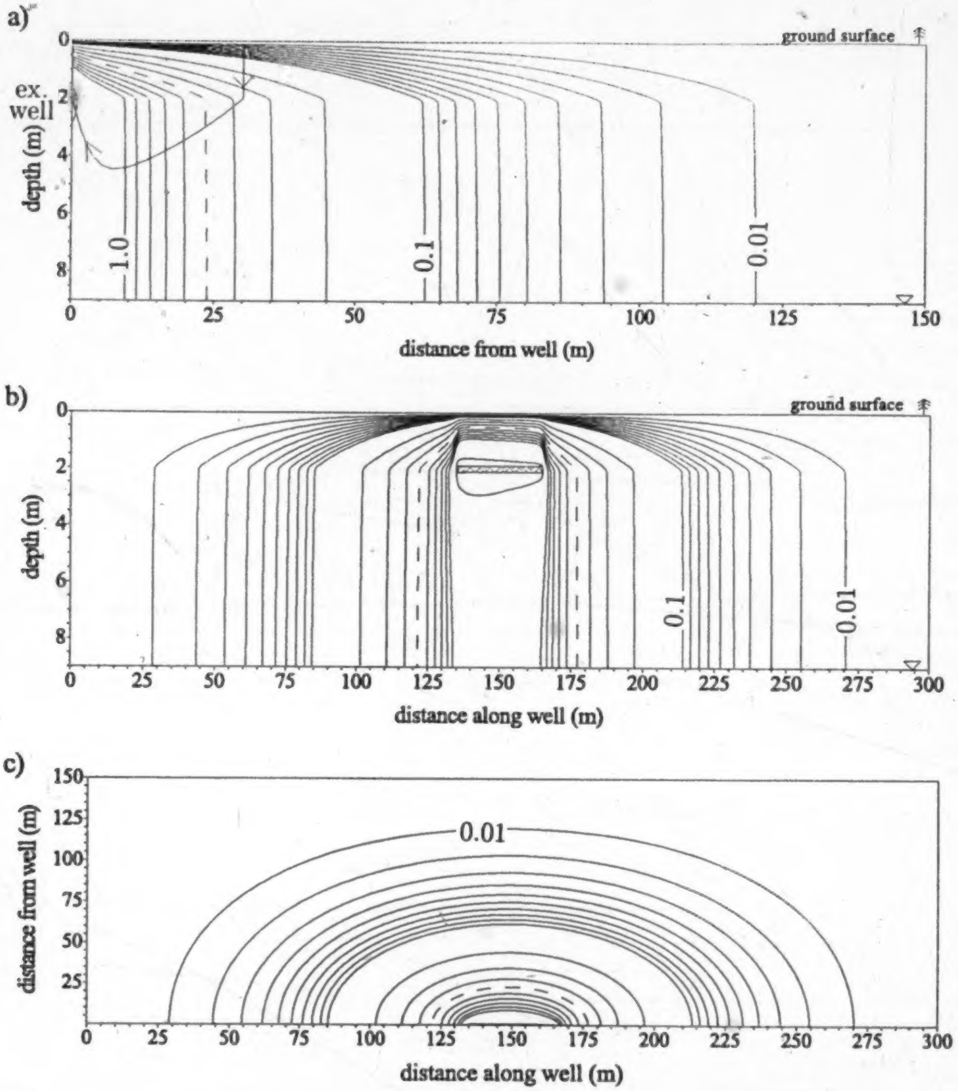

Figure 5.2: Pressure distributions for Base Case A. Dotted line = 0.5 %atm. Flowpath plotted on column cross-section for a particle 30 m from the middle of the horizontal well. Contour interval (%atm): 0.01 to 0.1 by 0.01 , 0.1 to 1.0 by 0.1, and 1.0 to 3.0 by 1.0 (a) Column cross-section, (b) Row cross-section, and (c) Layer cross-section.

Sensitivity Analysis	Travel Time Total	Travel Time Sand	Q_{ex}	V_5^*	Change in V_5^*
	(days)		(m^3/s)	($\times10^3$ m^3)	(%)
Base Case A	**1.1**	**0.6**	**8.5×10^{-2}**	**65**	**0**
Watertable Location, 9 m depth					
rises 2 m	1.0	0.5	7.8×10^{-2}	51	-22
drops 2 m	1.2	0.7	9.0×10^{-2}	78	19
Till, k=1.0×10^{-12} m^2					
no till, k=7.0×10^{-11} m^2	11	9.1	2.3×10^{-1}	11	-84
k=1.0×10^{-11} m^2	1.9	1.4	1.3×10^{-1}	26	-61
k=1.0×10^{-13} m^2	2.7	0.6	6.6×10^{-2}	101	55
Sand, k=7.0×10^{-11} m^2					
k=7.0×10^{-10} m^2	0.3	0.1	6.7×10^{-1}	343	430
k=7.0×10^{-12} m^2	17	14	1.3×10^{-2}	9	-85
k_z=7.0×10^{-12} m^2	9.6	7.5	4.5×10^{-2}	41	-37
Well Location, top of sand					
middle of the sand	0.9	0.5	1.1×10^{-1}	78	20
watertable	1.0	0.6	8.9×10^{-2}	57	-13
bottom of till	1.4	0.8	6.8×10^{-2}	65	0
Grid Dimensions and Discretization					
dec. grid discretization	1.1	0.6	8.6×10^{-2}	45	-30
inc. grid dimensions	1.1	0.6	8.5×10^{-2}	63	-4
full grid	na		1.7×10^{-1}	na	na
2D flow	0.8	0.5	6.0×10^{-2}	20	-69

Table 5.3: Results from sensitivity analyses for varying different geological and grid parameters, Case A. Bold font represents the Base Case values. Travel times are for a particle 30 m perpendicular to the middle of the horizontal well to travel to the well, Q_{ex} is the simulated extraction rate and V_5^* is the volume of porous media influenced after 5 d of extraction. The total volume of the domain is 405 000 m^3 except for cases with modified grid dimensions.

Sensitivity Analysis	Travel Time Total (days)	Travel Time Sand (days)	Q_{ex} (m^3/s)	V_5^* ($\times 10^3$ m^3)	Change in V_5^* (%)
Base Case A	**1.1**	**0.6**	**8.5×10^{-2}**	**65**	**0**
Well Length 30 m					
+ 20 m	1.0	0.6	1.1×10^{-1}	81	25
− 10 m	1.3	0.7	6.6×10^{-2}	53	-19
Well k=1.1×10^{-5} m^2					
k=1.1×10^{-6} m^2	1.7	1.0	5.4×10^{-2}	49	-24
k=1.1×10^{-4} m^2	1.0	0.6	9.2×10^{-2}	68	4
no well k	1.1	0.6	8.8×10^{-2}	66	2
Vertical Wells			(per well)	(per well)	(total)
one	3.5	1.8	2.2×10^{-2}	25	-62
one (point well)	na		8.5×10^{-2}		
two 10 m apart†	2.2	1.3	2.0×10^{-2}	19	-40
two 30 m apart†	5.8	4.7	2.1×10^{-2}	20	-38
two 60 m apart†	32	31	2.2×10^{-2}	22	-32
three 30 m apart†	2.2	1.3	2.1×10^{-2}	19	-14
Horizontal Wells			(per well)	(per well)	(per well)
two 113 m apart†	1.1	0.6	8.4×10^{-2}	60	-8
two 220 m apart†	1.1	0.6	8.5×10^{-2}	65	0
P_D=3.3 %atm					
P_D=2.3 %atm	1.6	0.9	6.0×10^{-2}	53	-19
P_D=4.3 %atm	0.8	0.5	1.1×10^{-1}	76	17
P_D=13.2 %atm	0.3	0.2	3.6×10^{-1}	131	102

Table 5.4: Results from sensitivity analyses for varying well properties, Case A. Bold font represents the Base Case values. Travel times are for a particle 30 m perpendicular to the middle of the horizontal well to travel to the well, Q_{ex} is the simulated extraction rate and V_5^* is the volume of porous media influenced after 5 d of extraction. The total volume of the domain was 405 000 m^3 except for lengthen and shorten well, and 2 horizontal wells. † Travel times, Q_{ex} and V_5^* are not symmetrical, therefore values cannot be doubled for full grid.

compared in sensitivity analyses pressure contour comparison. As well, the flowpath for a particle 30 m from the middle of the horizontal well has been plotted on the column cross-section. The pressure drawdown, P_D, in the first cell of the well was set to 3.3 %atm, with a calculated loss of 0.41 %atm along the 30 m well. This pressure distribution in the well corresponded to a simulated extraction rate of 8.5×10^{-2} m^3/s. Approximately 96.5% of the recharge to the system was through the ground surface boundary; the remaining 3.5% of the recharge entered from the 3 lateral boundaries. Thus, the grid is an adequate size.

As portrayed in the three cross-sections, flow in the till unit was essentially vertical. The till, acting as a confining layer, forced air to flow horizontally to the extraction well in the sand, creating a large zone of influence. A particle 30 m perpendicular from the middle of the well at ground surface took approximately 1.1 d to reach the well. Two particles were also placed 30 m perpendicular to the middle of the well, one at the bottom of the till and the second just below the first in the top of the sand. It took approximately 0.5 d for the particle to flow vertically through the 2 m thick till unit, and then a further 0.6 d to travel 30 m through the sand to the well. In comparison, a particle located near the watertable at the same lateral distance from the well took 0.8 d to travel to the well. At a distance of 75 m perpendicular to the middle of the well, a particle travelled from ground surface to the top of the sand in 4.7 d and took 11.0 d to travel the remaining distance through the sand. The volume of porous media influenced after 5 d of extraction (V_5^*) from the horizontal well was calculated to be 65 000 m^3, extending approximately 70 m from the well in the sand, as illustrated in Figure 5.3. This volume decreased to 23 000 m^3 for 1 d of extraction and to 43 000 m^3 for 2.5 d of extraction, and increased to 97 000 m^3 for 10 d of extraction.

With the defined air-filled porosity of 25%, the volume of air within the 5 d volume of influence was 16 000 m^3. Based on an extraction rate of 8.5×10^{-2} m^3/s, the calculated volume of air removed after 5 d from the extraction well was 37 000 m^3.

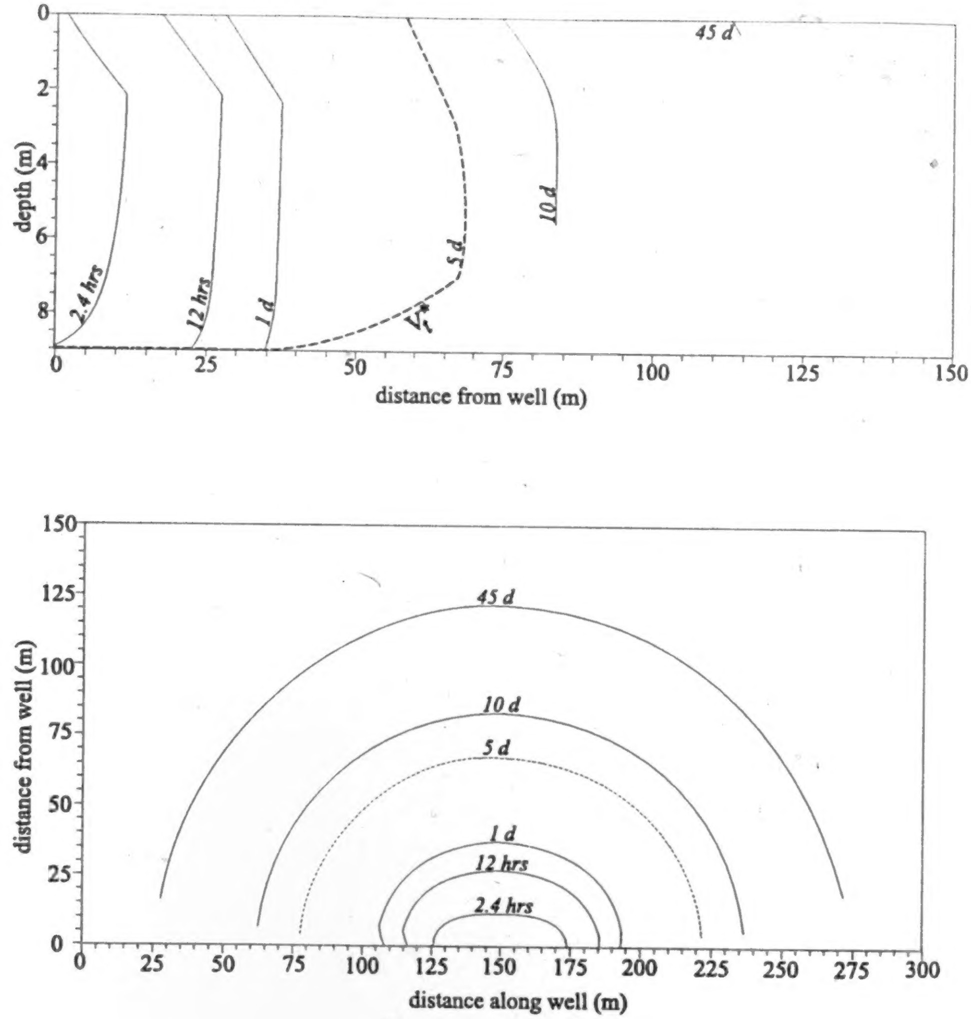

Figure 5.3: Volume of porous media influenced after: 2.4 hrs, 12 hrs, 1 d, 5 d, 10 d, and 45 d of extraction. Case A. (a) Column cross-section through middle of extraction well. (b) Layer cross-section at a depth of z = 2.1 m

The resulting three-dimensional volumetric flowrates per unit area are illustrated in Figure 5.4. Based on an extraction rate for a full grid of 0.17 m^3/s and a well cross-sectional area of 0.01 m^2, the velocity of air in the extraction well was approximately 17 m/s. As shown in the column and row cross-sectional plots (Figures 5.4(a) and 5.4(b)), the velocities below the extraction well were at least 1.0×10^{-4} m/s (10 m/d). In the lateral direction, the velocity of 1.0×10^{-4} m/s extends out approximately 20 m in the x- and y-directions.

One obvious difference between horizontal and vertical extraction wells is that flow to a horizontal well is not axisymmetric. The influence of end effects was evaluated by placing particles 30 m perpendicular and 30 m parallel to the well as illustrated in Figure 5.5. With a vertical extraction well and homogeneous porous media properties (i.e., an axisymmetric configuration), the travel times for particles at different angles, but the same distance from the well were, of course, identical. In comparison, when the particles were placed parallel to the horizontal well from both ends, 0.8 d were required to travel through the till and an additional 1.0 d were required to travel through the sand compared to 0.5 and 0.6 d perpendicular to the horizontal well, an increase of 0.7 d in the total travel time. Therefore, due to the end effects of the horizontal well, the pressure drawdown at a point perpendicular to the well was greater than a point parallel at the same distance from the well. The magnitude of this difference would decrease with decreasing well length, as the horizontal well approaches the configuration of a single extraction point.

5.4 Sensitivity Analysis for Case A

In the sensitivity analysis, geological and system parameters were varied and the results of the pressure distribution, travel time and flowpaths to the well, and the volume of porous media influenced after 5 d were compared to the Base Case. The geological and flow parameters representing Base Case A were described in Section 5.1 and outlined in Table 5.1.

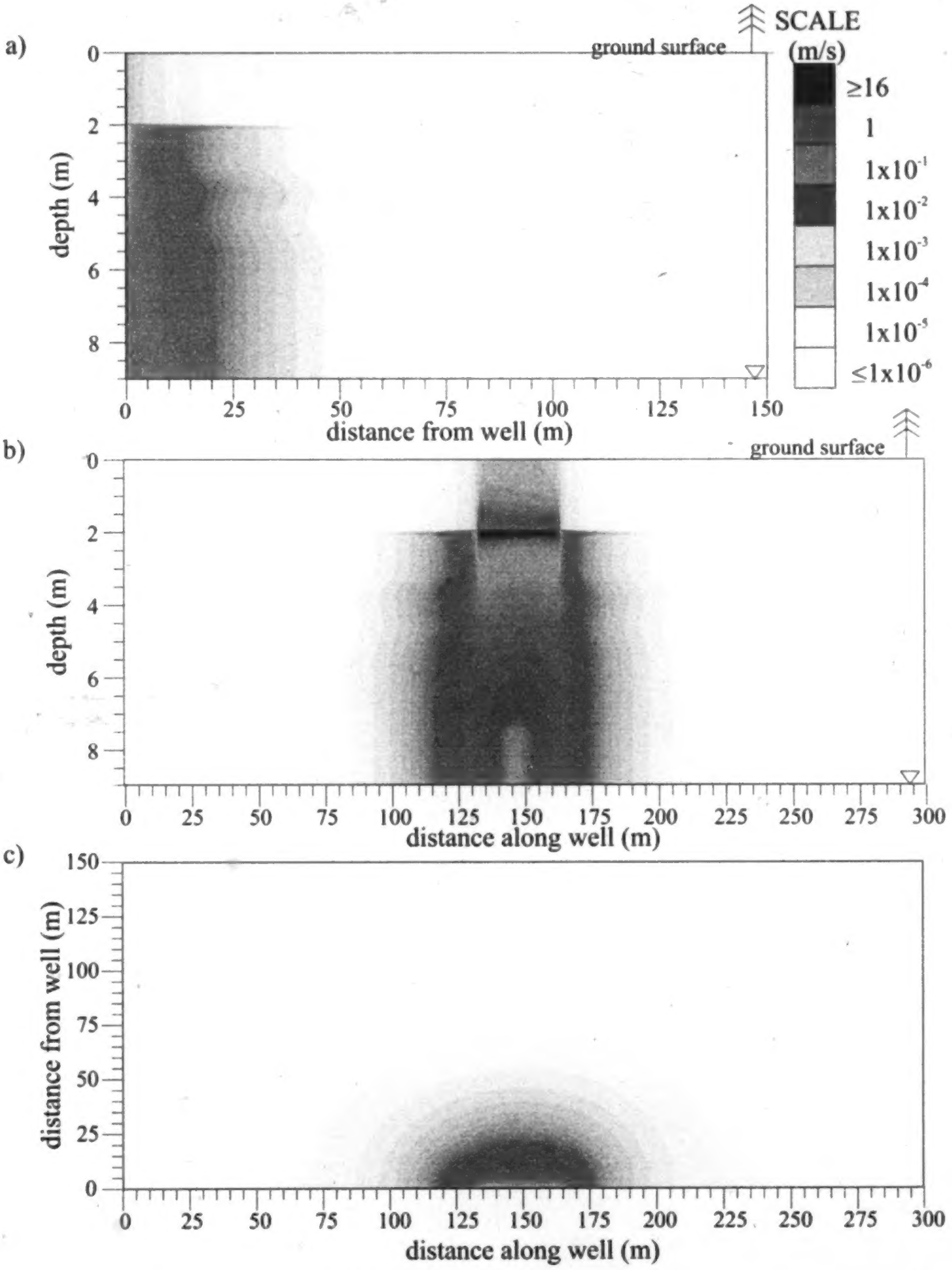

Figure 5.4: Volumetric flowrates per unit area for Base Case A. (a) Column cross-section, (b) Row cross-section, and (c) Layer cross-section.

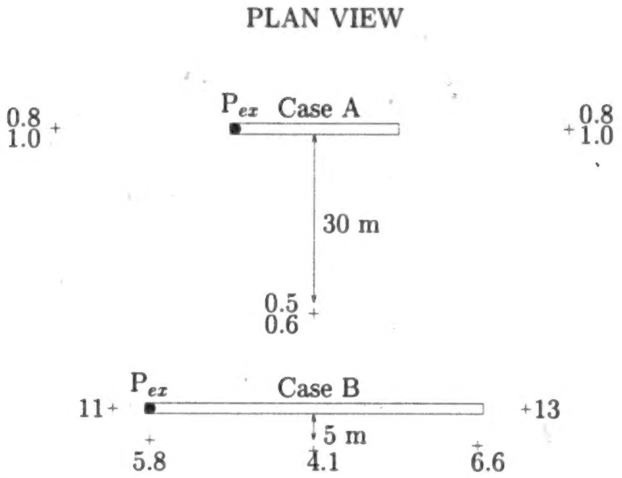

Figure 5.5: Travel times to well for different particle locations. For Case A times shown are time to travel through the till and time to travel through the sand in days. For Case B total time through till in hours is presented.

5.4.1 Permeability

The sensitivity of the flow solution to changing the permeabilities of the sand unit and the till unit was investigated. Numerical simulations by Rathfelder *et al.* (1991) showed that the efficiency of soil venting systems is highly sensitive to the soil permeability. The two geological units were treated separately in the analysis. For Case A, the base isotropic permeabilities were selected to be 1.0×10^{-12} m^2 for the till and 7.0×10^{-11} m^2 for the underlying sand.

Due to the heterogeneities of the geological properties, flow net analysis was not conducted on the cases in which only the sand permeability or only till permeability were varied. However, an order of magnitude decrease in both the till and sand permeability resulted in identical pressure distributions as illustrated in Figure 5.6, but an order of magnitude decrease in the extraction rate, as predicted by flow net theory.

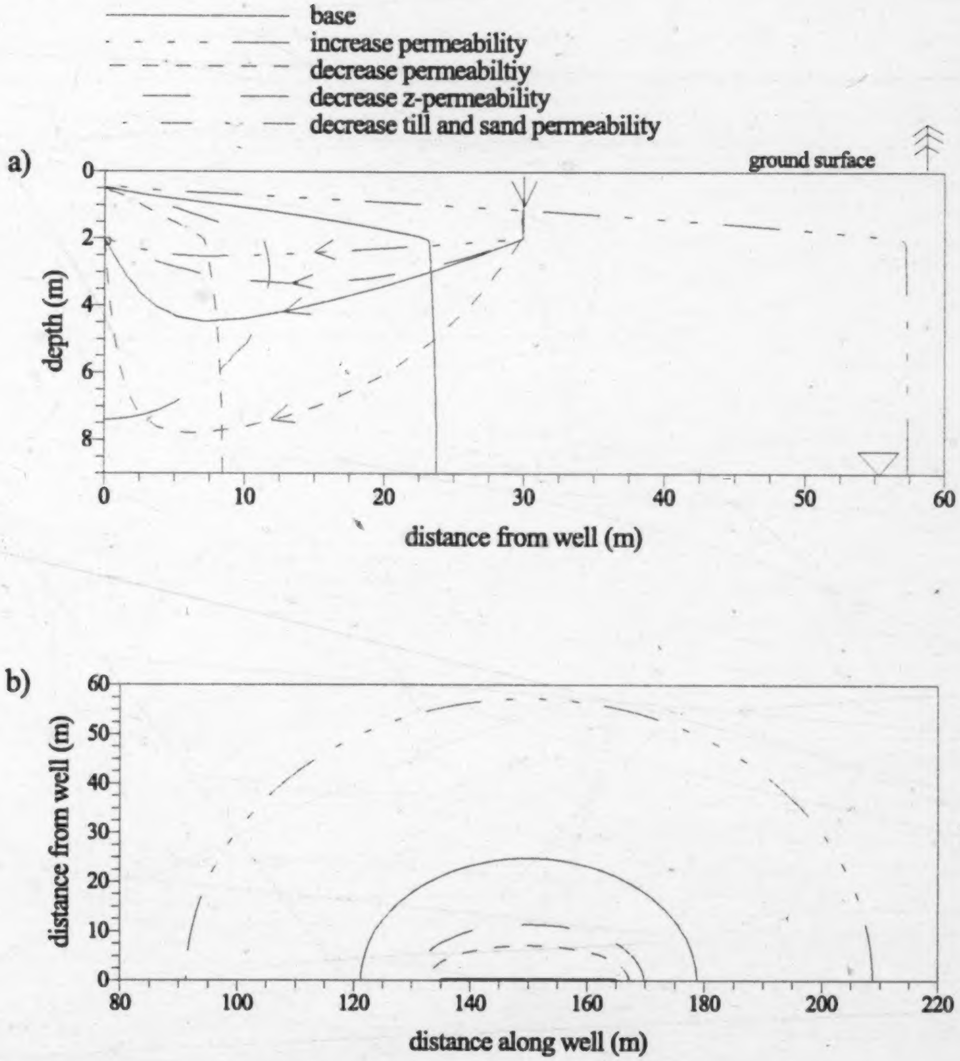

Figure 5.6: Varying the sand permeability, pressure drawdown contour = 0.5 %atm, P_D in extraction well = 3.3 %atm, particle trace for a particle located 30 m from extraction well. (a) Column cross-section. (b) Layer cross-section.

Sand Permeability

Three different analyses were simulated with varying sand permeability: 1) increasing the permeability one order of magnitude; 2) decreasing the permeability one order of magnitude; and 3) decreasing the z-permeability one order of magnitude. The well permeability was kept constant.

Increasing the permeability, which increased the permeability contrast between the sand and the till, caused greater pressure drawdowns as illustrated in Figure 5.6. The travel time in the sand decreased to 0.1 d, from 0.6 d.

By decreasing the sand permeability, to properties close to those of the till, the pressure drawdowns shrunk closer to the well. This also increased the travel time in the sand. A decrease in the sand z-permeability also resulted in the pressure drawdowns shrinking and the vertical flow component decreased in comparison to the horizontal component.

The volume of porous media influenced, listed in Table 5.3, clearly illustrates the effect of varying the sand permeability. Increasing the permeability one order of magnitude resulted in V_5^* increasing 5 times from the Base Case. However, in this simulation the boundary conditions utilized for all simulations were not appropriate as only 53% of the recharge was through the ground surface with the remaining 47% entering through the lateral boundaries. An order of magnitude decrease in the sand permeability resulted in V_5^* decreasing to 9 000 m^3, while decreasing the z-permeability decreased the volume to 41 000 m^3. Because the extraction pressure was kept constant, the calculated extraction rates change proportionally in all cases.

Till Permeability

Three scenarios were specified for varying the till permeabilities: 1) decreasing the till permeability one order of magnitude; 2) increasing the till permeability one order of magnitude; and 3) removing the till by assigning the till unit the permeability of the sand. Figure 5.7 illustrates the change in pressure distribution and flowpaths due to varying the till permeability.

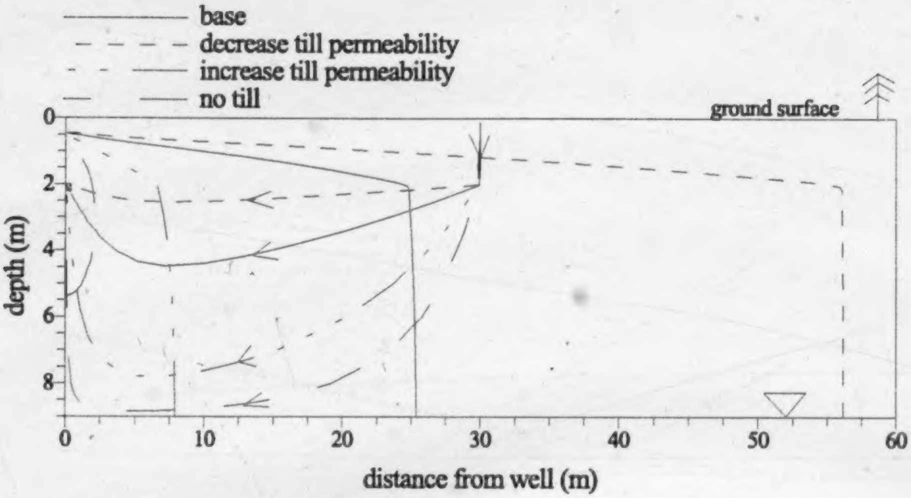

Figure 5.7: Varying the till permeability, pressure drawdown contour = 0.5 %atm, P_D in extraction well = 3.3 %atm, particle trace for a particle located 30 m from extraction well. Column cross-section.

Decreasing the permeability, and thus increasing the permeability contrast between the sand and the till, elongated the pressure drawdown contours. The decreased till permeability enhanced the ability of the till to behave like an impermeable cap, increasing the amount of flow through the sand. The path taken to the well was more direct, bypassing the volume of soil between the well and the watertable. The total travel time to the well doubled, while the travel time in the sand stayed constant. It also increased V_5^* to 101 000 m^3. Simulations of sites with a thick layer of low permeable soil at ground surface by Mohr and Merz (1995) found the best match between field and simulated pressures occurred when a barrier at the ground surface was specified. Similar to increasing the permeability of the sand, the boundary conditions selected were no longer strictly valid, with only 44% of the recharge entering through the ground surface boundary.

The two simulations with increased till permeability, the first in which the x- and z-permeabilities were decreased one order of magnitude and the second in which the till was replaced with sand, resulted in a decreased capability of the till to induce horizontal flow through the sand, and an increased amount of air entering vertically through the ground surface above the extraction well. As the till permeability was increased to that of the sand, the path taken to the horizontal well became deeper, with more flow along the watertable. V_5^* decreased drastically from 65 000 m^3 to 26 000 m^3 for increasing the till permeability one order of magnitude and to approximately 11 000 m^3 with no till cover. For the simulation with no till, the total travel time increased one order of magnitude, with the travel time in the sand also increasing one order of magnitude. Note that the geological conditions of no till makes this simulation similar to that of Case B in which no confining layer at ground surface is present.

5.4.2 Watertable Location

It is known that the watertable location at Strachan can vary seasonally by up to 3 m. Two simulations were conducted to observe the changes in the pressure distribution as a result of the watertable being located 2 m above and 2 m below the Base Case watertable elevation. The pressure distributions, flowpaths and travel times to the well did not change significantly. However, V_5^* increased approximately 20% as the volume of the system increased with a 2 m lower watertable.

5.4.3 Well Characteristics

Well characteristics, such as number and type of well, the well length, the well placement, and well permeability were examined in the sensitivity analysis. The Base Case horizontal well was 30 m in length and was located at the top of the sand at a depth of 2 m.

Number and Type of Wells

An important design aspect of a soil vapour extraction system is the selection of the type and number of wells. Modelling can provide a vital tool estimating the well configuration necessary for the required remediation goals. A number of different simulations with varying combinations of type and number of extraction wells were performed. These simulations included adding an additional horizontal well at different distances apart and simulating single and multiple vertical well systems. All the horizontal wells had 30 m screen lengths and were located at the top of the sand. The vertical wells were screened from the top of the sand to 2.5 metres above the watertable.

The two additional horizontal well simulations consisted of locating a second horizontal well either 113 m or 220 m from, and parallel to, the original horizontal well. The resulting pressure distributions are illustrated in Figures 5.8 and 5.9. By placing the horizontal wells 113 m apart, the zone of capture of the two horizontal wells overlapped as shown in Figure 5.9. V_5^* for each well decreased to 60 000 m^3 as a result of the first well influencing the second well. With two horizontal wells 220 m apart, V_5^* did not change from the Base Case, confirming that the wells were performing independently. Note that the volume calculated was only for half a grid and, depending on the conditions on the other half of the grid, this may not be symmetrical; therefore, the volumes, extraction rates and travel times are approximate.

The influence of multiple horizontal wells on the velocity field is illustrated in Figure 5.10. By placing two horizontal wells 220 m apart, the velocities at a distance of 75 to 110 m from the well decreased, creating a "dead zone" between the two wells. "Dead Zones" are defined by DePaoli (1991) as areas of the subsurface that display large pressure drawdowns, but low air velocities. So, although the zone of influence was essentially doubled with two wells 220 m apart, the porous media at a distance of 75 to 110 m from the horizontal well displayed decreased velocities. In contrast, when the wells were moved to only 113m apart, the volume of the dead

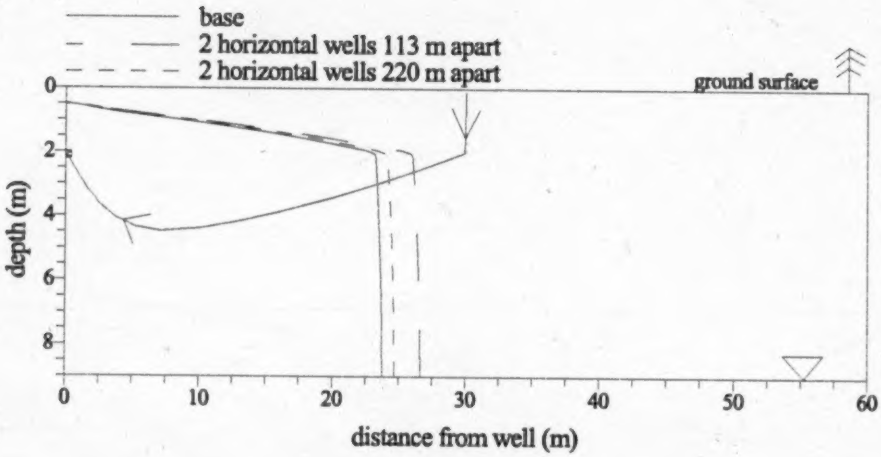

Figure 5.8: Varying the number of horizontal extraction wells, pressure drawdown contour = 0.5 %atm, P_D in extraction well = 3.3 %atm, particle trace for a particle located 30 m from extraction well. Column cross-section

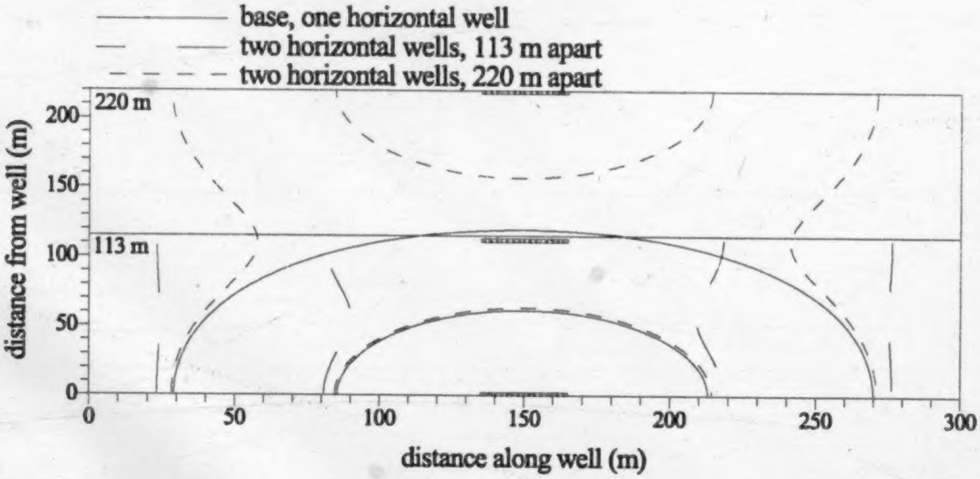

Figure 5.9: 0.01 and 0.1 %atm pressure contours for two horizontal wells at different distances apart, the dotted lines (only pressures between the two horizontal wells have been plotted), and the Base Case, solid line. Layer cross-section.

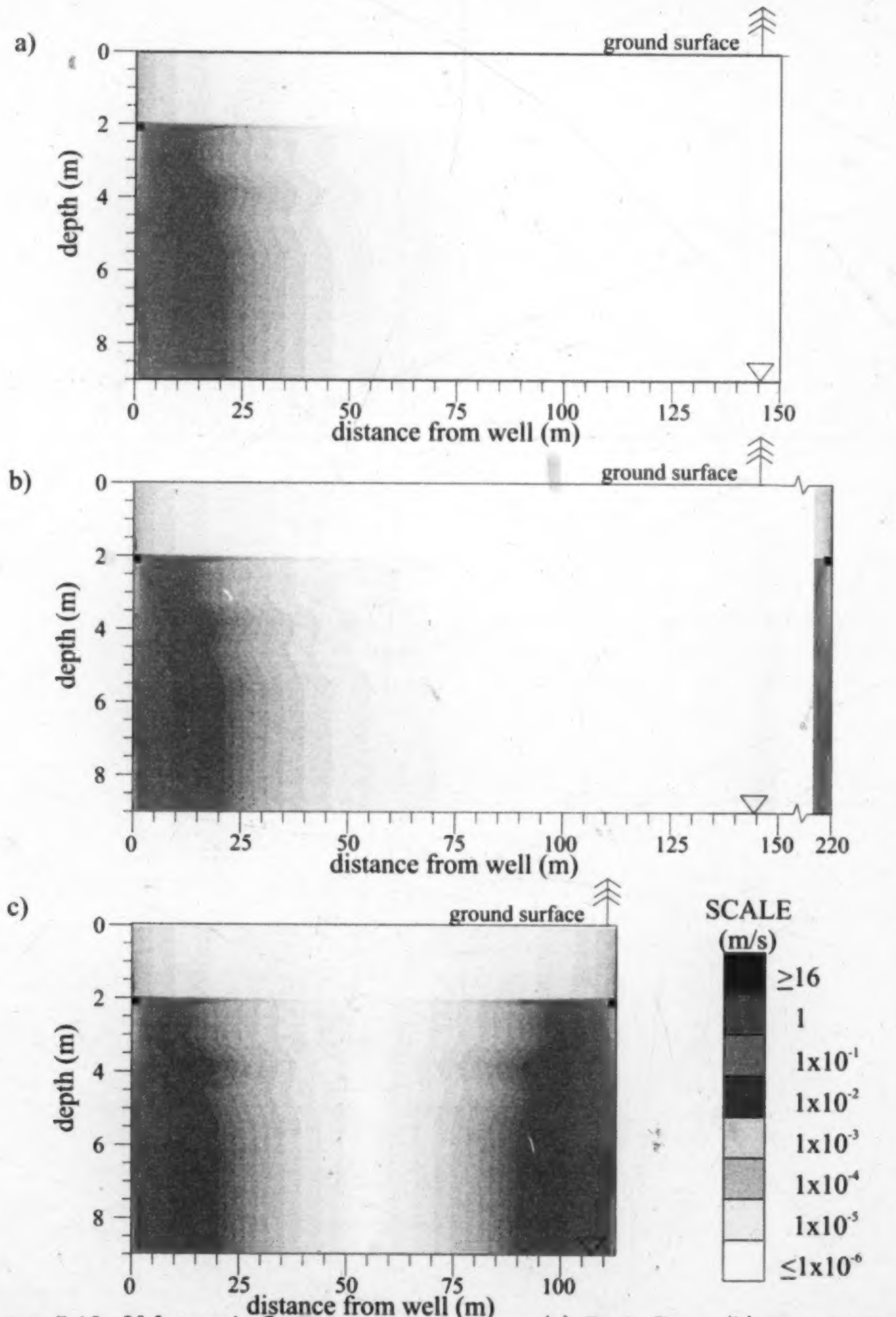

Figure 5.10: Volumetric flowrate per unit area. (a) Base Case, (b) Two horizontal wells 220 m apart, and (c) Two horizontal wells 113 m apart.

zone decreased.

At Strachan, there were a number of advantages of installing vertical wells. Compared to the horizontal well, the vertical wells were easier and less expensive to install and were able to access the entire depth of the unsaturated zone. A number of different vertical well configurations were simulated including: 1) one vertical well; 2) two vertical wells 10 m apart; 3) two vertical wells 30 m apart; 4) two vertical wells 60 m apart; 5) three vertical wells, each 30 m apart; and 6) one point well with the same Q_{ex} as Base Case A, screened from 2 to 2.1 m depth. These combinations were selected because the actual arrangement of vertical wells at the Strachan site involved one central vertical well with additional vertical wells located 30 m from the first vertical well. This analysis was designed to compare the existing vertical well system to that of the horizontal well for the given site geological conditions, to estimate the most efficient well configuration and to determine whether two-dimensional axisymmetric flow can represent flow to a horizontal well.

The pressure distribution and the values for V_5^* for the vertical wells were slightly smaller than for the horizontal well, as shown in Figures 5.11 and 5.12. The magnitude of V_5^* was dependent on the number of vertical wells and the extraction rate. As the vertical wells were placed farther apart, the area of overlap reduced to the point that their drawdowns were independent of one another. One vertical well had just under half V_5^* from the single horizontal well, but only one-quarter the extraction rate. The difference in extraction rates made the comparison between the horizontal and vertical well configurations approximate. The volume, V_5^*, increased to 56 000 m^3 for 3 vertical wells, just 9 000 m^3 less than the Base Case, for a total extraction rate of 6.3×10^{-2} m^3/s. The zone of influences between the horizontal and vertical wells simulations were similar primarily due to: 1) the influence the till as an impermeable barrier, preventing short circuiting to the well; and 2) the relatively short length of the horizontal well.

One simulation was completed with a vertical, or point, well at the same Q_{ex} as the Base Case. The vertical well was only screened from 2 to 2.1 m depth, and

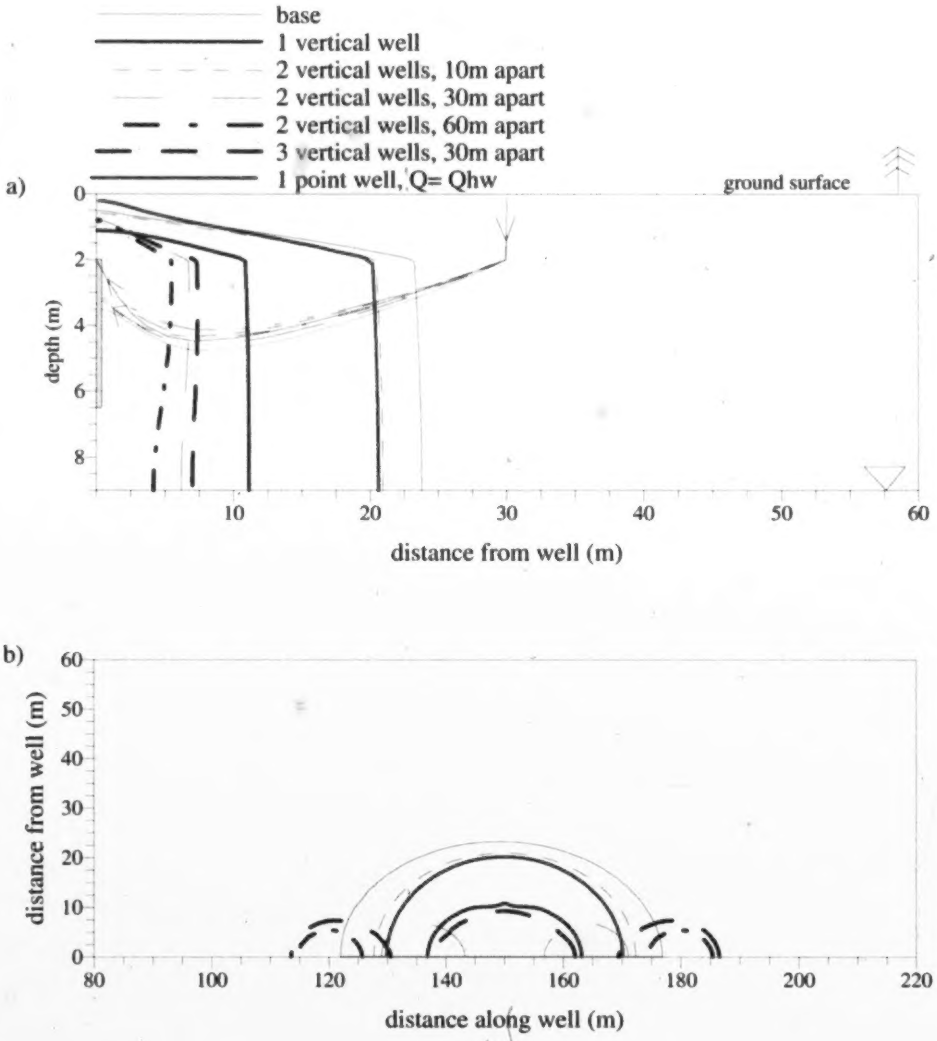

Figure 5.11: Varying the number of vertical extraction wells, pressure drawdown contour = 0.5 %atm, P_D in extraction well = 3.3 %atm, particle trace for a particle located 30 m from extraction well. (a) Column cross-section. (b) Layer cross-section.

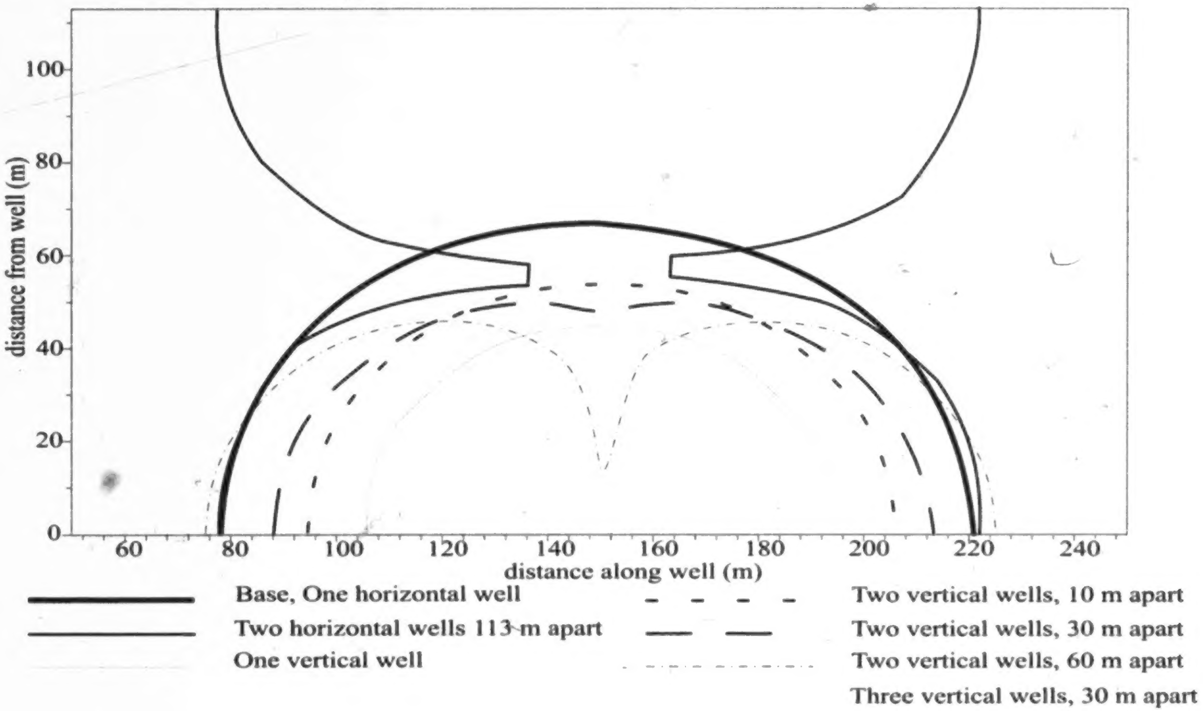

Figure 5.12: Zone of Capture of V_5^* for different well combinations. Layer cross-section at 2 m depth.

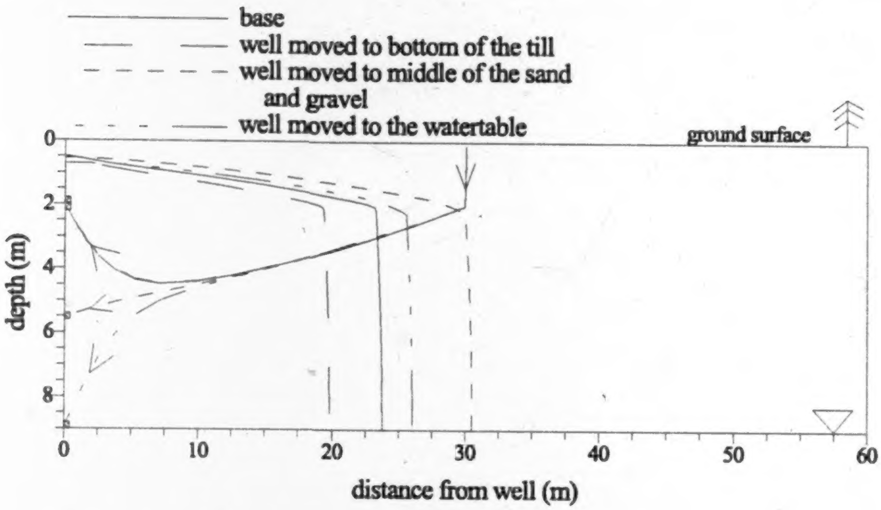

Figure 5.13: Varying well placement, pressure drawdown contour = 0.5 %atm, P_D in extraction well = 3.3 %atm, particle trace for a particle located 30 m from extraction well. Column cross-section.

the pressure drawdown was constrained to 27 %atm in order for the extraction rate to equal that of the horizontal well. Figure 5.11 shows that the pressure distributions were slightly less than the horizontal well. The implication of this is that two-dimensional axisymmetric coordinates modelling of a single point well can be used to approximate three-dimensional flow to a horizontal well under the geological, hydrogeological and SVE system conditions of Base Case A.

Well Location

Due to installation constraints at Strachan, a horizontal well installed in the top of the sand was the only feasible option. Other possible locations, but not practical from an installation perspective, included the middle of the sand at a depth of 3.35 to 3.45 m and at the bottom of the sand, just above the watertable. In addition to these two locations, installing the well at the bottom of the till was examined.

The effect of varying the well placement is illustrated in Figure 5.13. As would be expected, placing the well at the bottom of the till decreased the pressure drawdowns in the system and increased the travel time to the well. If the well were placed at the watertable, the pressure distribution, travel time to the well and V_5^* did not change significantly; however, a crucial difference with this scenario was the flowpath taken to the well. When the well was placed close to watertable, air flowed deeper in the unsaturated zone. This is important if the SVE was designed to remove contaminated air located near the watertable. However, locating a horizontal well in proximity to the watertable runs the risk of being affected by watertable fluctuations and upwelling. When the horizontal well was located in the middle of the sand, V_5^* increased by 13 000 m^3, a reflection of the greater volume of sand accessible and the increased pressure drawdowns created when the well was located in the middle of the sand.

Well Length

The length of the well is determined by installation method, blower capabilities, area of contamination and site logistics. Shortening the horizontal well to 20 m, approaching the configuration of a vertical well, decreased the pressure drawdowns and, correspondingly, decreased V_5^* by 19%. With a 50 m horizontal well, V_5^* increased by 25%. The particle flowpaths and times to reach the well changed only slightly. The 20 m long horizontal well exhibited less pressure loss along the length of the well: 0.2 %atm compared to 0.9 %atm for the 50 m long horizontal well.

Well Permeability

The horizontal well was represented in the Base Case by assigning every cell in the well a permeability of 1.1×10^{-5} m^2 and assigning a constrained pressure to only the first cell in the well. As explored in Chapter 2, a horizontal well can be expected to exhibit pressure losses in the well, as well as a change in well permeability, due to the transition from turbulent flow near the blower to possibly laminar flow near the far end of the well. With the limited amount of data available, a single permeability was examined in the base simulations. An option in AIR3D is to not assign the well a permeability and the model assumes the cells have an infinite permeability.

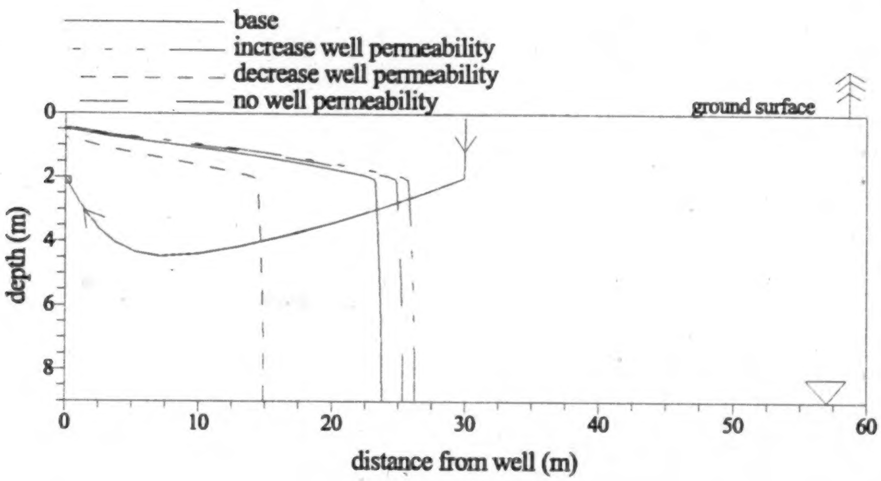

Figure 5.14: Varying well properties, pressure drawdown contour = 0.5 %atm, P_D in extraction well = 3.3 %atm, particle trace for a particle located 30 m from extraction well. Column cross-section.

As illustrated in Figure 5.14, increasing the well permeability one order of magnitude or assigning no well permeability did not affect the pressure distribution, travel time to the well nor V_5^* significantly. In comparison, decreasing the well permeability by one order of magnitude decreased V_5^* by 25% and increased the the travel time to the well by 0.6 d. The pressure difference between the two ends of the horizontal well decreased to less than 0.1 %atm when the well permeability was increased in contrast to a pressure difference of 2.0 %atm when the well permeability was decreased. The change in extraction rate and fraction of recharge from the atmosphere were insignificant.

Well Pressure

The method of defining the extraction rate required assigning a constrained pressure in the well. A P_D of 3.3 %atm was selected as the Base Case pressure, corresponding to an extraction rate of 8.5×10^{-3} m^3/s. At Strachan, only an estimate of the

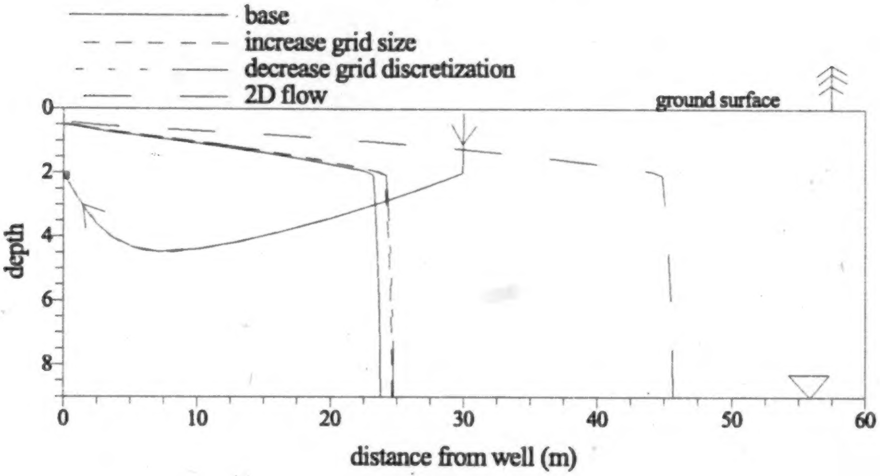

Figure 5.15: Varying model design, pressure drawdown contour = 0.5 %atm, P_D = 3.3 %atm, particle trace for a particle located 30 m from extraction well. Column cross-section.

pressure drawdown was available, hence an analysis of the consequences of changing the well pressure on the extraction rate, pressure distribution and V_5^* was important. By decreasing P_D to 2.3 %atm, the extraction rate decreased to 6.0×10^{-2} m^3/s and V_5^* was reduced to 53 000 m^3. In contrast, an increase of P_D to 4.3 %atm produced an extraction rate of 1.1×10^{-1} m^3/s and a V_5^* of 76 000 m^3. The pressure drawdown was then increased further to 13 %atm and the extraction rate increased to 3.6×10^{-1} m^3/s with V_5^* doubling to 131 000 m^3. At this pressure, the drawdown was still within the range acceptable for applying groundwater equations to air flow equations (Massmann, 1989).

5.4.4 Model Design

To ensure that the solution was not affected by the boundary conditions, a grid with the dimensions of 200 m by 400 m by 9 m was examined. As illustrated in Figure 5.15, increasing the grid dimensions had little effect on the pressure distributions, flowpath and travel time to the well and V_5^*. Furthermore, the fraction of recharge from the ground surface did not change. This confirms that for the Base Case, the boundary conditions selected were adequate.

A simulation of the Base Case conditions using a full grid-300 m by 300 m by 9 m (i.e., with no symmetry boundary) was analyzed. The pressure distribution of the Base Case was identical to that of a full grid and the extraction rate was twice that of the Base Case, confirming that the solution was not influenced by using only a half grid with a symmetry boundary.

The grid discretization of the Base Case was increased by a factor of 1.5 from the previous cell as recommended for FDM grid design (Anderson and Woessner, 1992). A subsequent grid was designed with cell discretization only increasing by a factor of 1.2, increasing the total number of cells in the domain from 115 000 cells to 178 000. Similar to increasing the grid dimensions, decreasing the grid discretization had little effect on the pressure distribution solution. However, V_5^* decreased by 30%. The solution to the volumetric flux requires the gradient to be calculated; a discretization factor of 1.2 resulted in a more accurate solution of the fluxes.

Finally, a two-dimensional scenario was simulated in AIR3D by reducing the grid dimension in the x-direction to 30 m and assigning impermeable boundaries to the two lateral boundaries. As illustrated with the pressure distributions in Figure 5.15, utilizing a two-dimensional model to simulate a horizontal well produced overpredicted pressure distributions because the same amount of air was extracted from a smaller volume, neglecting all end effects.

5.5 Base Case B

The pressure drawdown distributions in layer, row and column cross-sections illustrated in Figure 5.1 for Base Case B are shown in Figure 5.16. The pressure contour intervals are the same as Base Case A, except that 4.0 %atm, 5.0 %atm and 6.0 %atm pressure drawdown contours were also included. The 0.5 %atm contour was also selected for comparison between the Case B simulations. The pressure in

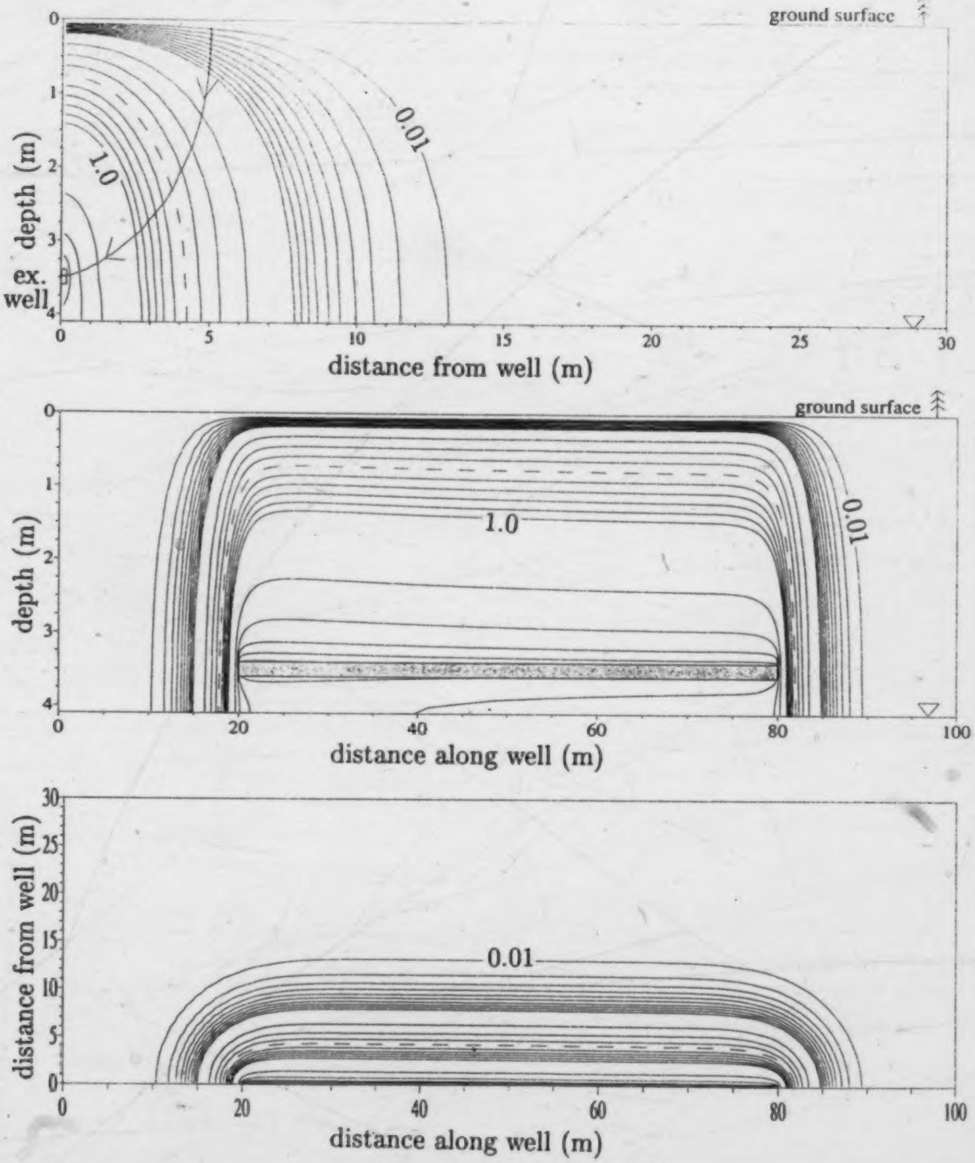

Figure 5.16: Pressure distributions for Base Case B. Dotted line = 0.5 %atm. Flowpath plotted on column cross-section for a particle 5 m from the middle of the horizontal well. Contour interval (%atm): 0.01 to 0.1 by 0.01 , 0.1 to 1.0 by 0.1, and 1.0 to 6.0 by 1.0 (a) Column cross-section, (b) Row cross-section, and (c) Layer cross-section.

Sensitivity Analysis	Travel Time (hours)	Q_{ex} (m^3/s)	$V^*_{0.5}$ ($\times 10^3$ m^3)	Change in $V^*_{0.5}$ (%)
Base Case B	**4.1**	**5.4×10^{-2}**	**1.9**	**0**
Watertable Location, 4.1 m depth				
rises 0.5 *m*	4.3	5.2×10^{-2}	1.6	-15
drops 0.5 *m*	4.1	5.6×10^{-2}	2.0	6
till, k_1=6.0×10^{-12} m^2, k_2=$k_1/6$				
k_1=6.0×10^{-11} m^2, k_2=$k_1/6$	0.4	5.5×10^{-1}	2.8	48
k_1=6.0×10^{-13} m^2, k_2=$k_1/6$	40	5.5×10^{-3}	0.8	-58
k_{z1}=6.0×10^{-13} m^2, k_{z2}=$k_{z1}/6$	9.1	1.7×10^{-2}	2.0	5
Add Cover	2.8	4.5×10^{-2}	2.6	34
Well Location, 3.5 m depth near watertable				
bottom of the till	3.8	8.2×10^{-2}	1.8	-8
middle of the till	4.3	5.0×10^{-2}	2.1	11
Flow				
Two-dimensional Flow	4.1	5.3×10^{-2}	1.8	-6
Well Length, 60 m				
+ 20 *m*	4.4	6.7×10^{-2}	2.7	39
− 30 *m*	3.8	2.9×10^{-2}	1.1	-45
Well k=6.0×10^{-6} m^2				
k=6.0×10^{-7} m^2	7.6	3.2×10^{-2}	1.6	-17
k=6.0×10^{-5} m^2	3.8	5.9×10^{-2}	1.9	1
no well *k*	4.0	5.5×10^{-2}	1.9	1
Number and Type of Wells		(per well)	(per well)	(total)
2 horizontal 30 m apart†	4.2	5.4×10^{-2}	1.9	0
2 vertical†	8.4	4.4×10^{-3}	0.3	-86
P_D=6.6 %atm				
P_D=5.6 %atm	4.8	4.6×10^{-2}	1.8	-4
P_D=7.6 1 %atm	3.6	6.2×10^{-2}	2.0	2
P_D=16.6 %atm	1.7	1.4×10^{-1}	2.4	23

Table 5.5: Results from sensitivity analyses for Case B. Travel times are for a particle 5 m perpendicular to the middle of the horizontal well to travel to the well, Q_{ex} is the simulated extraction rate and $V^*_{0.5}$ is the volume of porous media influenced after 0.5 d of extraction. The total volume of the domain is 12 300 m^3 except for lengthen and shorten well. † Travel times, Q_{ex} and V^*_5 are not symmetrical, therefore values cannot be doubled for full grid.

the first cell of the 60 m horizontal extraction well was constrained to 93.4 %atm, P_D = 6.6 %atm, which corresponded to a simulated extraction rate of 5.4×10^{-2} m^3/s. The pressure loss from the beginning of the well to the last cell of the well was 0.9 %atm. Approximately 99.95% of the air entering the domain did so through the ground surface, satisfying the criteria that the boundaries be placed far enough from the extraction well that they have minimal effect on the solution.

The zone of influence created by the horizontal extraction well for Case B was small due to the absence of a cover and the low permeability of the porous media. As illustrated in Figure 5.16, flow was essentially vertical from the ground surface to the well. There was some horizontal flow along the watertable due to the location of the extraction well near the watertable, but the velocities were relatively small. The volume of porous media influenced after 0.5 d of extraction was 1 900 m^3.

A particle placed at ground surface 5 m perpendicular to the middle of the well took 4.1 hrs to travel to the well from ground surface compared to 14 hrs for a particle placed at the same distance along the watertable. This increase in time for the latter particle was due to the lower permeability in the till with an increased residual saturation, located directly above the watertable. At a similar distance parallel to the well, a particle took 11 hrs to travel from ground surface to the end of the well closest to the well head, and 13 hrs to travel to the end farthest from the well head. As well as demonstrating the consequence of end effects, this example also illustrated the influence of well losses.

The volume of porous media influenced after 0.5 d, $V^*_{0.5}$, was calculated to be 1 900 m^3. This volume decreased to 1 100 m^3 when the time was reduced to 0.1 d and increased to 2 300 m^3 after 1 d of extraction. As illustrated in Figure 5.17, the volume influenced after 0.5 d extends out from the well approximately 7 m. Based on an extraction rate of 5.4×10^{-2} m^3/s and an air-filled porosity of 25%, the volume of air removed by the extraction well after 0.5 d was 2 300 m^3, compared to a volume of 600 m^3 in the 0.5 d zone of influence.

The velocity in the extraction well, based on a volumetric flowrate of 0.11 m^3/s

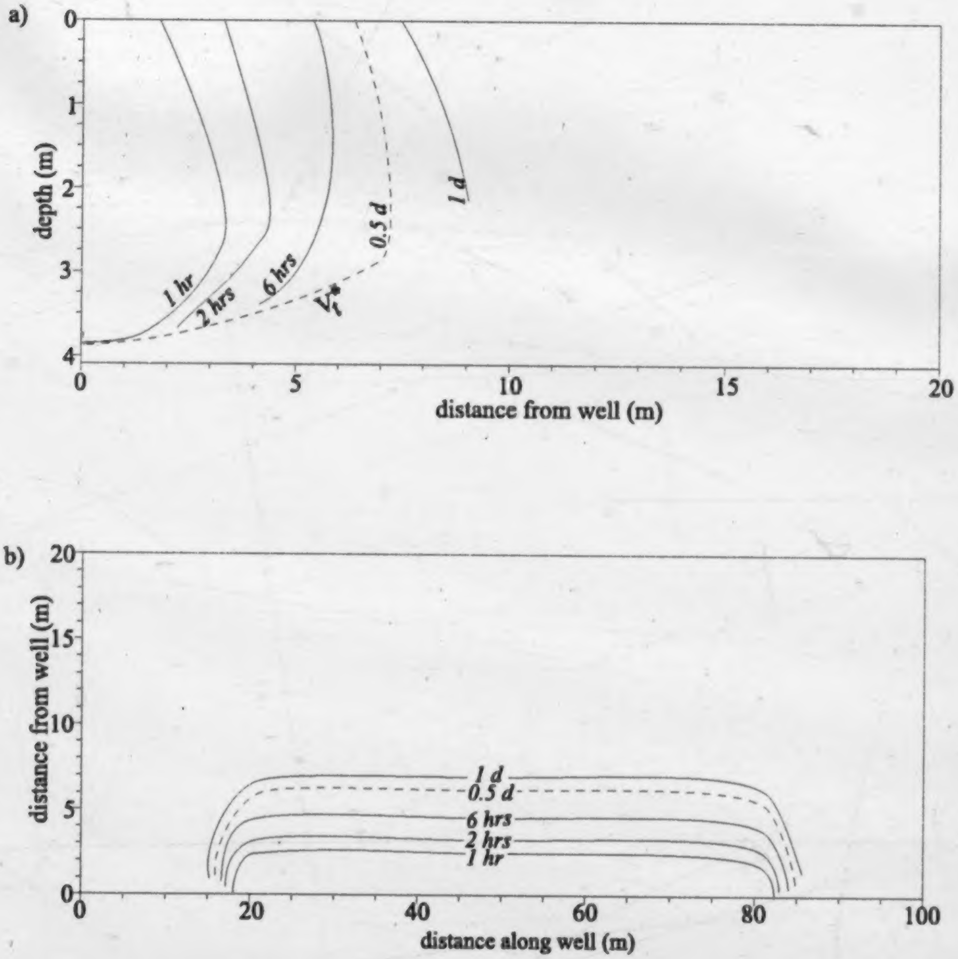

Figure 5.17: Volume of porous media influenced after: 1 hr, 2 hrs, 6 hrs, 0.5 d, and 1 d of extraction. Case B. (a) Column cross-section through middle of extraction well. (b) Layer cross-section at a depth of $z = 3.5$ m

(for a full grid) and a cross-sectional area of 0.01 m^3, was 11 m/s. The fluxes for the column, row and layer cross-sections are plotted on Figure 5.18. In comparison to Base Case A, a velocity of 1.0×10^{-4} m/s (10 m/d) was only observed at a lateral distance of approximately 5 m from the extraction well. Additionally, the velocity decreased in the lower permeability till at 3.6 to 4.1 m depth, as illustrated in Figure 5.18(a).

5.6 Sensitivity Analysis for Case B

The geological and flow parameters representing the Base Case B were described in Section 5.1 and outlined in Table 5.2. The boundary conditions and grid domain used for the Base Case were found to be suitable for all the sensitivity analyses and will not be discussed further.

5.6.1 Permeability

As outlined in Section 5.1, the unsaturated zone geology of Case B was divided into two till units, the first unit extending from ground surface to a depth of 3.5 m, with a permeability of 6.0×10^{-12} m^2, and a lower till with a permeability of 1.0×10^{-12} m^2. Four simulations were performed to determine the sensitivity of the flow solution to the permeabilities: 1) increase the till permeability one order of magnitude; 2) decrease the till permeability one order of magnitude; 3) decrease the till z-permeability one order of magnitude; and 4) add a cover. The latter was accomplished by changing the permeability of the top layer of the domain to 1.0×1.0^{-14} m^2, two orders of magnitude smaller than the till. This was intended to represent some impermeable barrier situated at ground surface to prevent air short circuiting to the well.

Flow net theory can be used to predict the change in flowrate and pressure distribution with changing permeability. As explained in Section 2.5, an order of magnitude increase in the x- and z-permeabilities of both till units only resulted in an order of magnitude increase in the flowrate with no change in the pressure distribution, as

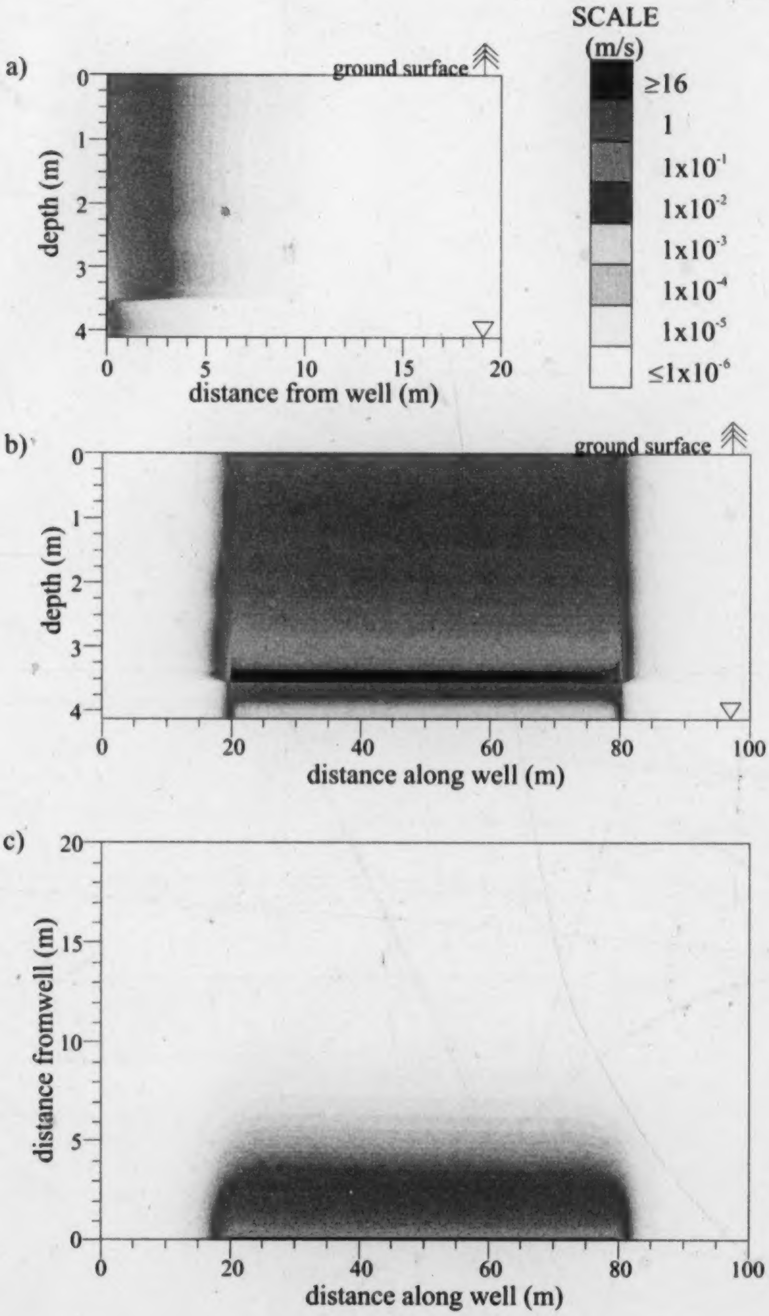

Figure 5.18: Volumetric flowrates per unit area for Base Case B. (a) Column cross-section, (b) Row cross-section, and (c) Layer cross-section.

illustrated in Figure 5.19. Likewise an order of magnitude decrease in the permeability resulted in an order of magnitude decrease in the flowrate with no change in the pressure distribution. Although the pressure distribution did not change for altering both k_x and k_z, $V^*_{0.5}$ changed to 2 800 and 800 m^3 for an increase and decrease in the permeability, respectively.

However, when only k_z was decreased by one order of magnitude, (2.28) and (2.29) were used to estimate the location of the transformed pressure distribution. Based on these equations, the x-component of the pressure contours was transformed by:

$$x_{inv} = x_{trans} \times \sqrt{10} \tag{5.1}$$

In decreasing the z-direction permeability, the horizontal component of flow was increased, thus the pressure distribution was shifted laterally as illustrated in Figure 5.19.

The advantage of adding a lower permeability cover to a SVE system is evident in Figure 5.20, where the pressure drawdowns increased substantially from the Base Case. By obstructing the short circuiting of air flowing vertically from the ground surface to the extraction well, air was forced to flow laterally within the domain towards the well and the pressure distributions were shifted laterally, resulting in the $V^*_{0.5}$ increasing to 2 600 m^3.

5.6.2 Watertable Location

As with Case A, changing the watertable location had little effect on the pressure distribution and travel time to the well. Only $V^*_{0.5}$, as shown in Table 5.5, was influenced with the increase in domain size. In reality, a rising watertable could present problems for this site, by decreasing the air-filled porosity and permeability near the well with increased water saturation and possibly flooding the well with product and water, which did occur at Site B.

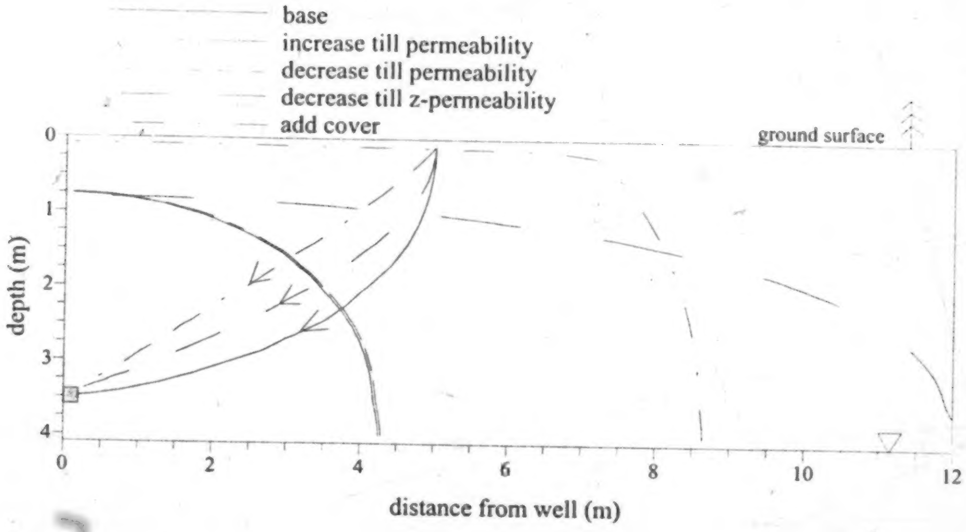

Figure 5.19: Varying the till permeability, pressure drawdown contour = 0.5 %atm, $P_D = 6.6$ %atm, particle trace for a particle located 5 m from extraction well. Column cross-section.

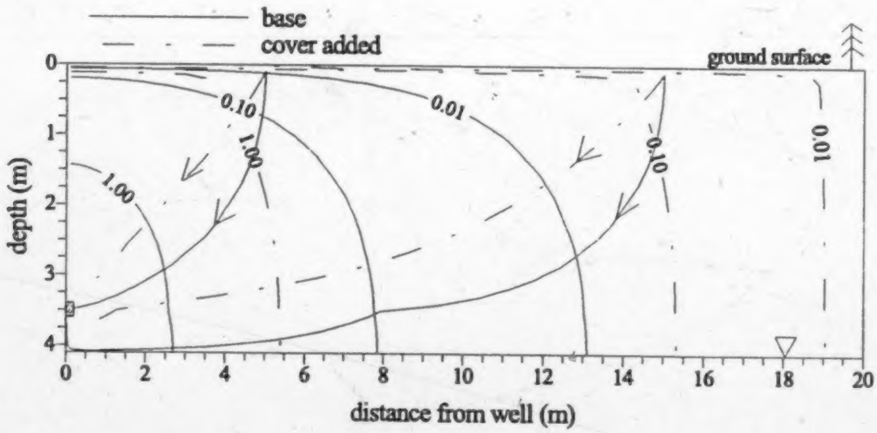

Figure 5.20: Pressure distribution for adding a cover and Base Case. Column cross-section

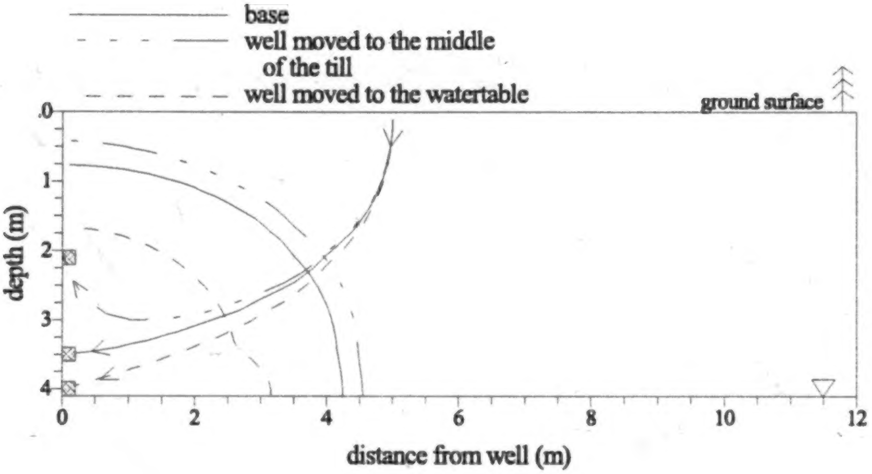

Figure 5.21: Varying the well location, pressure drawdown contour = 0.5 %atm, P_D = 6.6 %atm, particle trace for a particle located 5 m from extraction well. Column cross-section

5.6.3 Well Characteristics

Well Location

Two new well positions were selected, as shown in Figure 5.21: one located just above the watertable and a second located in the middle of the till at a depth of 2.0 to 2.1 m. In locating the well just above the watertable, the well was placed in the lower permeability till, thus the pressure drawdowns decreased, $V^*_{0.5}$ decreased and the travel times for a particle to reach the well from ground surface increased. As well, locating the horizontal well too close to the watertable may result in water and product entering the well. When the well was located in the middle of the till, a slight increase in the pressure drawdown and $V^*_{0.5}$ was observed. However, with the well located in the middle of the till, less flow was observed along the watertable.

Number and Type of Well(s)

The shallow unsaturated zone at Site B required that vertical wells have short screen lengths. A number of vertical wells were installed at Site B in clusters, with approximately 20 to 100 m separating the clusters. Additionally, three parallel horizontal wells were installed, each separated by approximately 15 m. Initial modelling estimated that the lateral zone of influence was on the order of 10 m. Therefore to observe the influence of overlapping pressure distributions, well spacings of 15 and 30 m were selected. To compare the different well arrangements at Site B, three well configurations were established: 1) two vertical wells 40 m apart; 2) two horizontal wells 30 m apart; and 3) two horizontal wells 15 m apart. Both vertical wells were screened at a depth of between 1 and 4 m and the horizontal wells were both 60 m long, located at the same depth as the Base Case.

Figure 5.22 clearly displays the large difference between the horizontal well pressure distributions and those of the vertical wells. Essentially, the shape of $V^*_{0.5}$ for both the horizontal well and vertical wells was cylindrical, with the cylinder aligned vertically for the vertical well and laterally for the horizontal well. The consequence was that $V^*_{0.5}$ was less than 600 m^3 the vertical wells, compared to 1900 m^3 for a horizontal well.

The influence of multiple horizontal wells on the velocity field is illustrated in Figure 5.23. There was no change in the velocity distribution by placing the wells 30 m apart, with little interaction between the two wells. In contrast, when a second horizontal well was placed 15 m from the original well, the volume of the “dead zone”, zone of high pressure drawdowns and low velocities, decreased.

Well Length

The length of the horizontal well considered in Base Case B was 60 m. Two simulations were performed with well lengths of 30 m and 80 m. The configuration of the horizontal well when shortened 30 m verged on that of a vertical well with less end effects, as indicated in Figure 5.24. Therefore the pressure at the mid-section

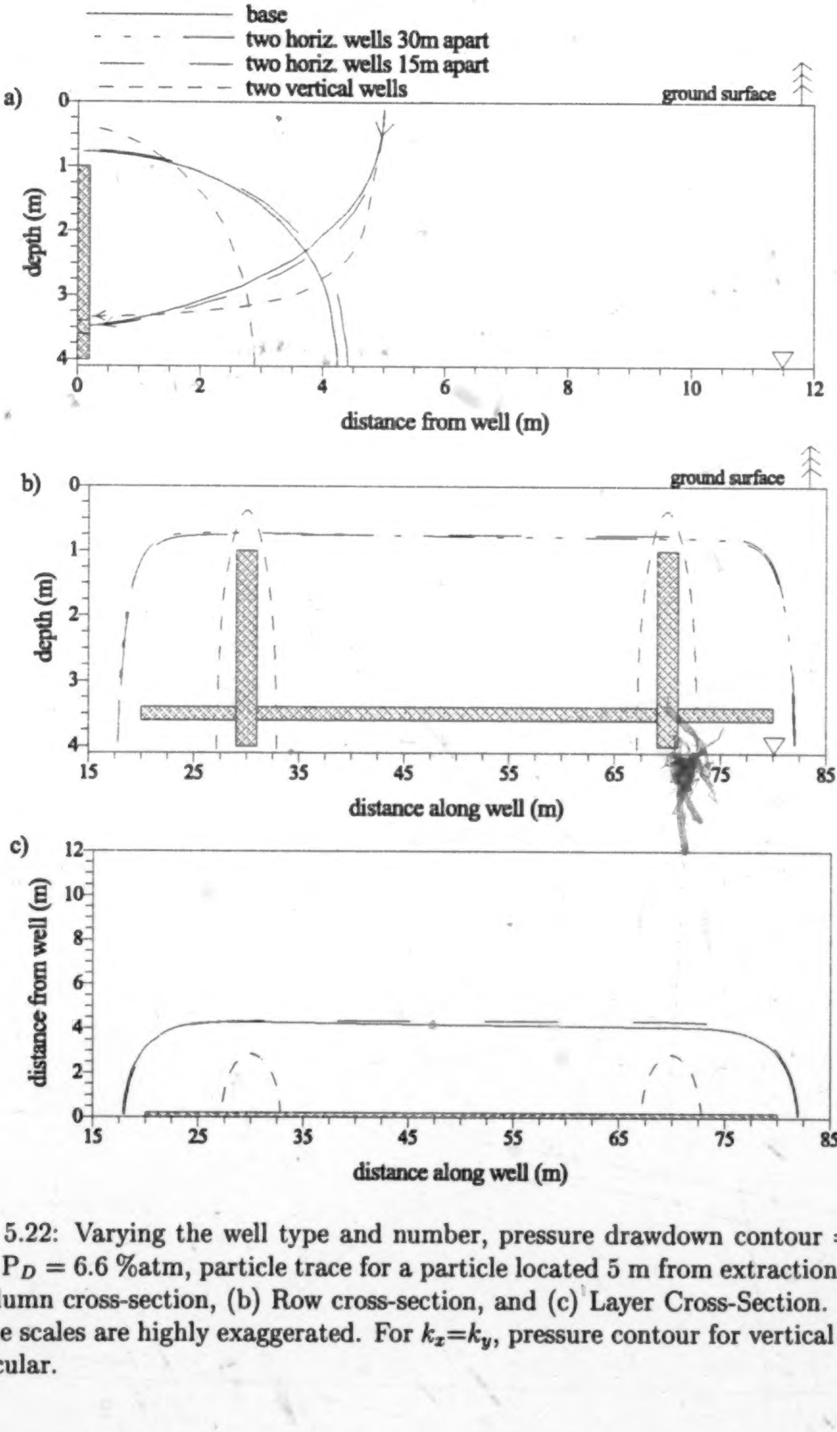

Figure 5.22: Varying the well type and number, pressure drawdown contour = 0.5 %atm, P_D = 6.6 %atm, particle trace for a particle located 5 m from extraction well. (a) Column cross-section, (b) Row cross-section, and (c) Layer Cross-Section. Note that the scales are highly exaggerated. For $k_x = k_y$, pressure contour for vertical wells are circular.

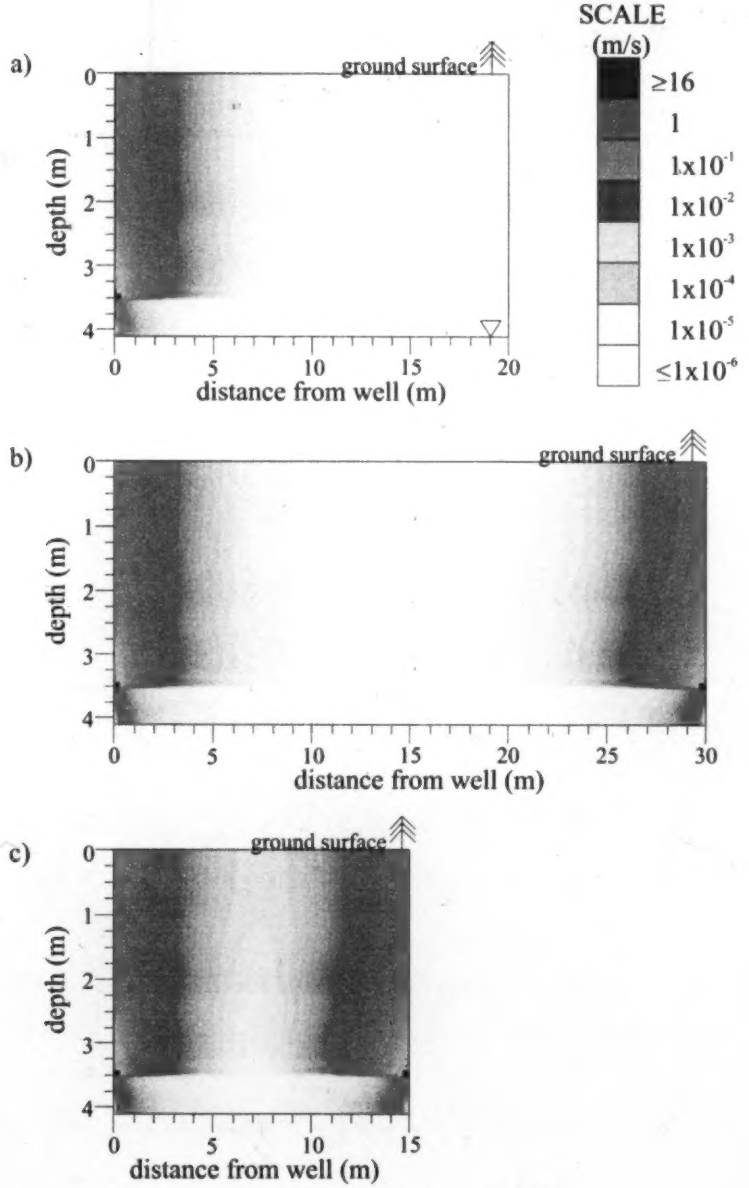

Figure 5.23: Volumetric flowrate per unit area. (a) Base Case, (b) Two horizontal wells 30 m apart, and (c) Two horizontal wells 15 m apart.

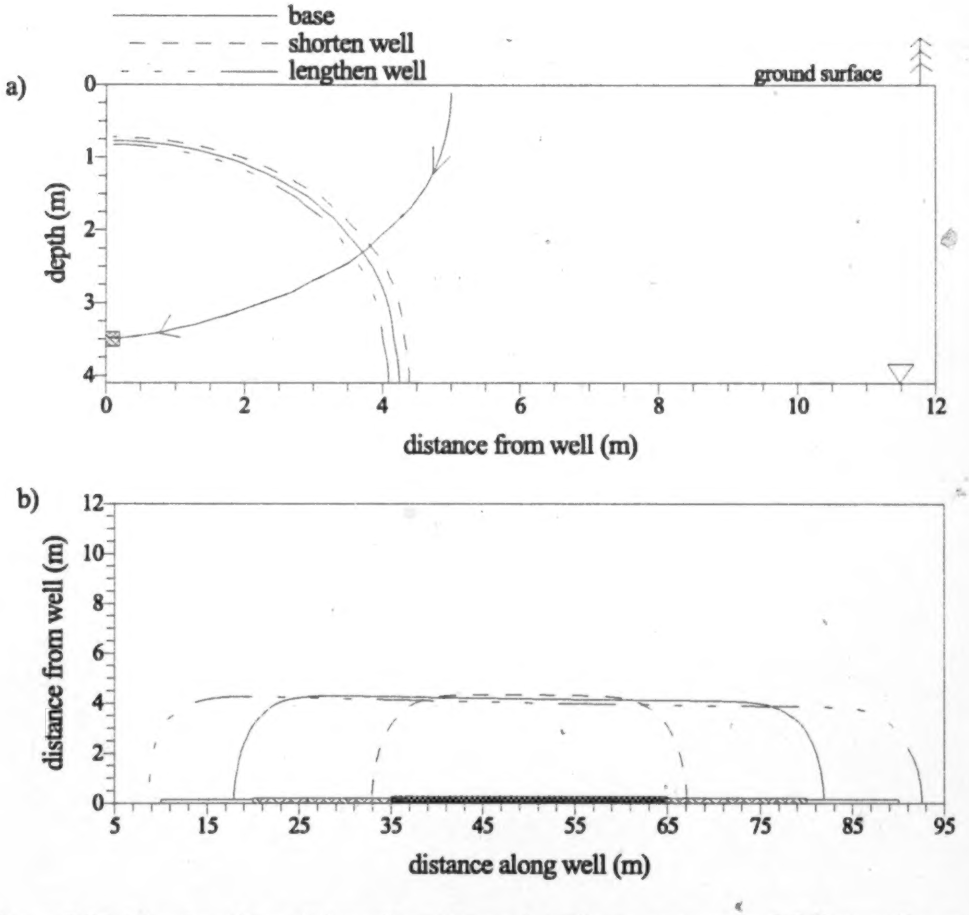

Figure 5.24: Varying the well length, pressure drawdown contour = 0.5 %atm, P_D = 6.6 %atm, particle trace for a particle located 5 m from extraction well. (a) Column cross-section. (b) Layer cross-section.

of the well was greater than the Base Case. With the shorter well, $V^*_{0.5}$ and the extraction rate were nearly half that of the Base Case. Lengthening the horizontal well 20 m increased $V^*_{0.5}$ to 2 700 m^3. The modelled pressure loss along the 30 m horizontal well was calculated to be 0.3 %atm compared to 1.5 %atm for an 80 m well.

Well Permeability

The well permeability selected for Case B was 6.0×10^{-6} m^2. This value took into account the longer length of the well and higher extraction rate in (3.8) compared to Case A. The pressure distribution in Figure 5.25 confirms that an increase of one order of magnitude in the well permeability had no effect on the pressure distribution, flowpath, extraction rate and $V^*_{0.5}$. The same results were observed when no well permeability was selected. In comparison, a decrease of the well permeability one order of magnitude resulted in the pressure drawdowns decreasing and $V^*_{0.5}$ decreasing by 17%. It is interesting to observe the pressure losses in the well varying from 0.9 %atm for a well permeability of 6.0×10^{-5} m^2 to almost 4.4 %atm for a well permeability of 6.0×10^{-7} m^2. Thus, because of the potential for well losses, well diameter may be an important parameter for horizontal wells.

Well Pressure

Finally, the effect of varying the pressure drawdown on $V^*_{0.5}$ and the extraction rate was analyzed. Table 5.5 displays the results of $V^*_{0.5}$. A 1 %atm decrease in the pressure drawdown resulted in a decrease of $V^*_{0.5}$ by 4% and a decrease in the calculated extraction rate by 15%. The volume enlarged 2% with a 1 %atm increase in the pressure drawdown and by 23% with a 10 %atm increase. The resulting extraction rates also increased by 15% and 165% respectively. A pressure drawdown of 16.5 %atm is still within the recommended range for applying groundwater equations to air flow equations (Massmann, 1989).

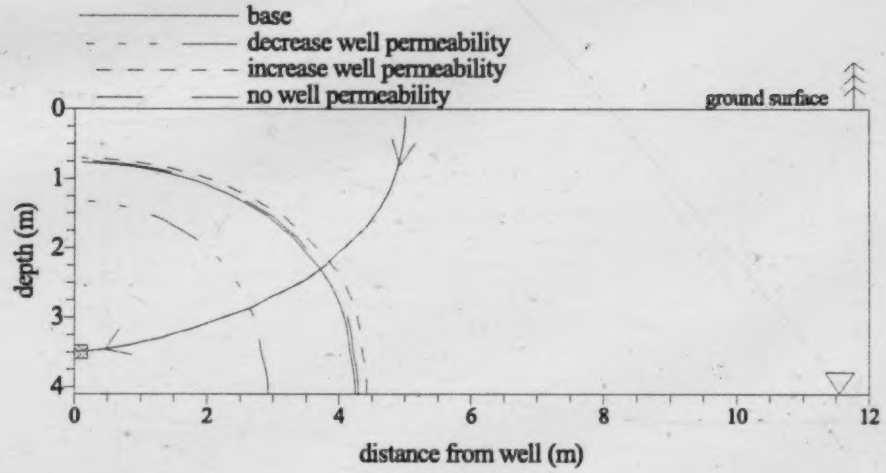

Figure 5.25: Varying the well permeability, pressure drawdown contour = 0.5 %atm, P_D = 6.6 %atm, particle trace for a particle located 5 m from extraction well. Column cross-section

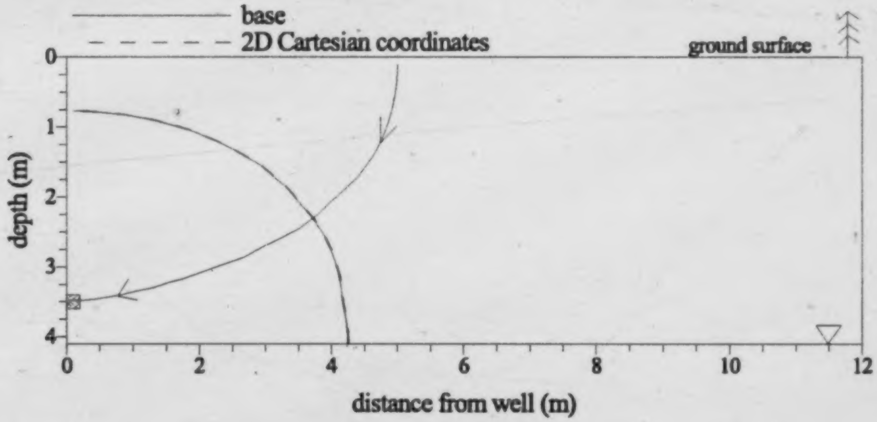

Figure 5.26: 2D cartesian coordinates, pressure drawdown contour = 0.5 %atm, P_D = 6.6 %atm, particle trace for a particle located 5 m from extraction well. Column cross-section

5.6.4 2D Flow

Flow in a section represented by two-dimensional cartesian coordinates was simulated in AIR3D by decreasing the grid dimensions to 60 m and specifying the lateral boundaries to be impermeable. As illustrated in Figure 5.26, the pressure distribution created by two-dimensional cartesian flow to the horizontal well was close to that of the Base Case and the travel times to the well were identical. The volume of porous media influenced only decreased by 6%.

5.7 Comparison of Case A to Case B

To illustrate the contrast between Case A and Case B, an analysis of the effect of the geological and pressure characteristics was conducted. The 0.5 %atm pressure drawdown for the two Base Cases are plotted on Figure 5.27. For Case A, the 0.5 %atm contour extended out approximately 25 m from the horizontal well compared to only 4 m for Case B. This difference was more evident when comparing the V_1^* (i.e., 1 d of extraction): 23 000 m^3 for Case A compared to 2 300 m^3 for Case B. Factors that account for this large difference includes pressure and extraction rates, well lengths and location, permeability of the subsurface units, presence of a cover, and depth to the watertable. Even when properties such as well length and depth to the watertable were factored into the volumes, Case A still has an order of magnitude larger volume. Subsequently Case A was simulated with the till and sand having properties of the till at Case B. V_1^* for Case A decreased to 5 600 m^3, illustrating the importance of the high permeability sand with the low permeability barrier at the ground surface. A simulation of Case A with Case B till properties and P_D=6.6%atm yielded V_1^* for Case A of 13 800 m^3.

5.8 Summary

A sensitivity analysis was conducted to determine the effect that geological and hydrogeological parameters, well characteristics and model design have on the pressure

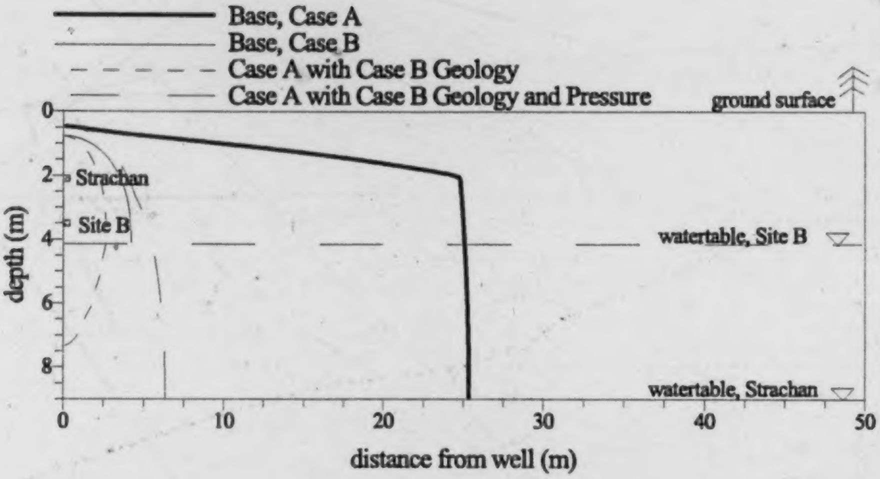

Figure 5.27: Comparison of the two Base Cases, pressure drawdown contour = 0.5 %atm. Column cross-section

distribution, flowpath and travel time to the extraction well, and the volume of porous media influenced after a given time. Two generic cases with similar characteristics to the two sites examined in Chapter 4 were examined.

A method was developed to determine the volume of porous media influenced after a given time. This method can be used as a comparison method for analyzing the effect of changing properties; however, similar grids must be used because the solution is somewhat dependent on the grid discretization. The results were also dependent on the number of particles used in MODPATH, therefore a large number of particles (e.g., 1000 or more) should be used.

For Base Case A, the pressure distribution representing the 0.5 %atm pressure drawdown contour was located approximately 24 m from the extraction well. A particle placed 30 m perpendicular from the well at ground surface took 0.5 d to travel 2 m vertically through the till and an additional 0.6 d to travel 30 m through the sand. An analysis of the volume of porous media influenced after 5 d of extraction estimated a volume of 65 000 m^3. The zone of the subsurface which contained velocities greater than 10 m/d extended vertically from the extraction well to the watertable and 20 m horizontally from the well.

In comparison, the 0.5 %atm pressure contour was observed at a distance of only 4 m for Base Case B. The time required for a particle to travel approximately 5 m from ground surface to the extraction well was 4.1 hours. The volume of porous media influenced after 0.5 d of extraction was calculated to be 1 900 m^3. Finally, the zone where the velocities were greater than 10 m/d only extended laterally approximately 5 m from the extraction well.

In both cases, the permeability and the influence of a low-permeability cover were the most sensitive parameters. As confirmed by flow net theory, an order of magnitude increase or decrease in all the permeabilities only resulted in a change in the extraction rates and velocities, not in the pressure distribution. For Case A, an order of magnitude decrease in the sand permeability resulted in more than an order of magnitude increase in the total travel time to the well and an 85% decrease in V_5^*. Similarly, removing the till cap resulted in an order of magnitude decrease in the travel time and a 84% decrease in V_5^*. This emphasizes the importance in characterizing the subsurface permeability properties as accurately as possible. Likewise, Case B exhibited similar results to Case A with varying permeabilities. An order of magnitude decrease in the till permeability resulted in an order of magnitude increase in the travel time to the well and a 58% decrease in the volume of porous media influenced after 0.5 d. A simulation conducted to determine the effect of adding a cover at ground surface resulted in $V_{0.5}^*$ increasing by 34%.

One consequence of locating the horizontal well near the watertable is that the extraction well may also remove product and water. Simulations showed the largest volume of soil influenced occurred when the well was located in the middle of the unsaturated zone. For Case B, however, this resulted in slightly less flow along the watertable than if the well was located near the watertable. In practice the location of the horizontal well is often determined by installation constraints.

Only limited amount of data were available on the pressure distributions within the actual extraction wells. The method developed in this study uses pipe-flow theory to represent the well, which assigns a single permeability to the well, and yielded similar results to assigning no well permeability. The implication of this was that, although assigning no well permeability resulted in no pressure losses in the horizontal well, much time and computer space was saved in the process. Until more data or information is known on well losses, the default well setting in AIR3D appears to be a suitable method.

The air flow results for horizontal wells were compared to simulations with vertical wells. A limitation to this analysis is that for a given horizontal and vertical well, the extraction rate, and thus the volume of porous media influenced, was highly dependent on the screened length. AIR3D requires a constrained pressure, with the extraction rate calculated as output, thus for comparison purposes the constrained variable was the pressure.

For Case A, a constrained pressure of 3.3 %atm in a vertical well resulted in an extraction rate approximately one quarter of the horizontal well extraction rate. The volume of soil influenced after 5 d of extraction for one vertical well decreased by 60% for Base Case A. This difference decreased to less than 14% when three vertical wells were utilized. An increased extraction rate in the vertical wells would further decrease the difference in the volumes. These similar volumes were a result of the high permeability of the sands compared to the till, the large volume of soil influenced because of the till cap, and the screened length of the vertical well throughout the sand unit.

A comparison of horizontal and vertical wells for Case B was examined. The resulting extraction rate for a vertical well, based on a constrained pressure, was over an order of magnitude smaller. The volume of porous media influenced created by two vertical wells decreased by 86% to less than 600 m^3 total. As illustrated in Figure 5.22, the discrepancy between the vertical and horizontal wells was due to the pressure distributions, with only a small zone of influence created by the vertical wells. Although the pressure distribution was approximately the same in the x-

direction (Figure 5.22(a)), the advantage of having a long screened length with the horizontal well is illustrated in Figure 5.22(c).

Two-dimensional cartesian coordinates simulations were completed for both cases. For Case A, the two-dimensional cartesian coordinates simulation grossly overpredicted the pressure drawdowns and under predicted V_5^* for the horizontal well due to the zone of influence and the short horizontal well. However, a simulation with two-dimensional axisymmetric flow from a point source resulted in pressure distributions similar to the horizontal well. In contrast to Case A, the two-dimensional cartesian coordinates analysis of the horizontal well in Case B resulted in only a 6% decrease in $V_{0.5}^*$. The implication of this is that a two-dimensional cartesian coordinates simulation of the flow conditions with Case B parameters is adequate.

Chapter 6

Conclusions

Soil vapour extraction is a remediation technique for removing volatile contaminants from the unsaturated zone. The use of horizontal wells with SVE, rather than traditional vertical wells, has been examined. As part of SVE systems at two gas plant sites in Western Canada, horizontal wells were installed by Komex International Ltd. The contrast between the two sites where the horizontal wells were installed clearly illustrates the significance of geological conditions in controlling air flow. At Strachan, a 30 m trench well was installed below 2 m of till at the top of 7 m of unsaturated sand. In contrast, a 60 m directionally drilled horizontal well was located near the watertable at a depth of 3.5 m in till at Site B.

Two numerical models were utilized to examine air flow during soil vapour extraction. VapourT, a two-dimensional FEM, formulated to use either axisymmetric or cartesian coordinates, simulated the steady-state flow of incompressible gas. The second model utilized, AIR3D, is a three-dimensional FDM that simulated the steady-state flow of compressible air. One-dimensional and two-dimensional flow analyses were performed to estimate the differences that occurred in the two models due to compressibility effects and the method of formulation of the FEM and FDM equations. These differences were minimal if the pressure drawdown at the well was within typical SVE conditions and a fine grid discretization was used near the extraction well.

Data from field SVE tests conducted by Komex International Ltd. were used to estimate the permeabilities at the two sites through numerical modelling of air flow. Pressure drawdown in the extraction well was required to estimate the permeabilities with AIR3D. The permeabilities were adjusted until the best match between pressures observed during the horizontal SVE test and pressures simulated with AIR3D was found.

A limitation of AIR3D was that the extraction well pressure drawdown and either the permeability or the extraction rate were required as input. For both field programs, the extraction rate was known, but only estimates of the pressure drawdown in the extraction well and the soil permeabilities were available. Thus, different combinations of the extraction well pressure drawdown and permeabilities would result in the required extraction rate.

Most studies investigating SVE focus on the transport of volatile contaminants in the unsaturated zone. However, an understanding of the factors controlling air flow and the sensitivity of different parameters on air flow is vital for estimating transport during SVE. Therefore, a sensitivity analysis was conducted to determine the most sensitive geological, hydrogeological and well parameters, and model design to the air flow solution based on the pressure distribution, flowpaths and travel times to the extraction well, and the volume of porous media influenced after a given time.

The air flow results were most sensitive to the permeabilities. An order of magnitude change in the permeability estimates could be the result of poorly characterized site parameters, heterogeneities or changing moisture content with watertable fluctuations or upwelling. Within the expected range of permeabilities, large differences in the pressure distribution, travel time to the well and volume of porous media influenced in a given time were calculated. The techniques used in the sensitivity analysis are not unique to horizontal wells and can be applied to vertical SVE systems as well.

The effect of an impermeable barrier at ground surface was demonstrated by comparing Base Case A to a simulation with no till cap, and Base Case B to a simulation in which the top layer was assigned a permeability two orders of magnitude smaller than the till. It was shown that the lower permeability layer at ground surface for Case A produced significantly larger pressure drawdowns farther from the well, prevented short-circuiting and created greater velocities and flow along the watertable, even with the well located at a depth of only 2 m. The same effect was observed for Case B when a low permeability was assigned to the top layer. Whether construction of such barriers are possible warrants investigation.

Two-dimensional flow to the horizontal well with cartesian coordinates was analyzed for both sites. In the example of Case B, a good estimate of air flow to a horizontal well was simulated with the 2D cartesian coordinates. For Case A, 2D cartesian coordinates provided a poor estimate to the flow to the horizontal well. However, 2D axisymmetric flow to a point source provided a satisfactory estimate of three-dimensional flow to this horizontal well. Thus, 3D air flow models can be used to determine the applicability of employing a 2D cartesian coordinates model for simulating flow to a horizontal well. If a 2D cartesian coordinates air flow model provided similar pressure distributions to the 3D model, a 2D cartesian coordinates transport model could be used to model transport in 2D rather than 3D, saving computer processing time and storage space.

Pressure losses were observed along the length of horizontal well during SVE test at Strachan. An equation was developed to estimate the equivalent permeability of the pipe under turbulent and laminar flow conditions. However, both field and numerical analyses should be performed to better predict the influence of well diameter, soil permeability, perforation size, and well length on pressure losses in horizontal wells during SVE.

Simulations examining the effect of multiple extraction wells indicated that there is little advantage to installing horizontal wells at Strachan. The vertical wells, which were screened in the sand, were capable ensuring air flow near the watertable. The difficulty in installing directionally drilled or dug horizontal wells near the watertable in the sand and gravel also make the selection of vertical wells at Strachan more feasible. In contrast, the simulations indicate that the long horizontal well at Site B provides a more efficient SVE system than vertical wells. Therefore, fewer wells would have to be installed with horizontal wells than if vertical wells were utilized, reducing the amount of surface disturbance at the site. Directional drilling techniques that were possible at the site allowed installation of the horizontal well at a depth deeper than a dug trench would provide.

An in-depth analysis to compare the costs of installation, operational and maintenance costs should be conducted to determine whether horizontal or vertical wells are more practical at a given site.

Appendix A

FDM and FEM Grid Discretization Figures

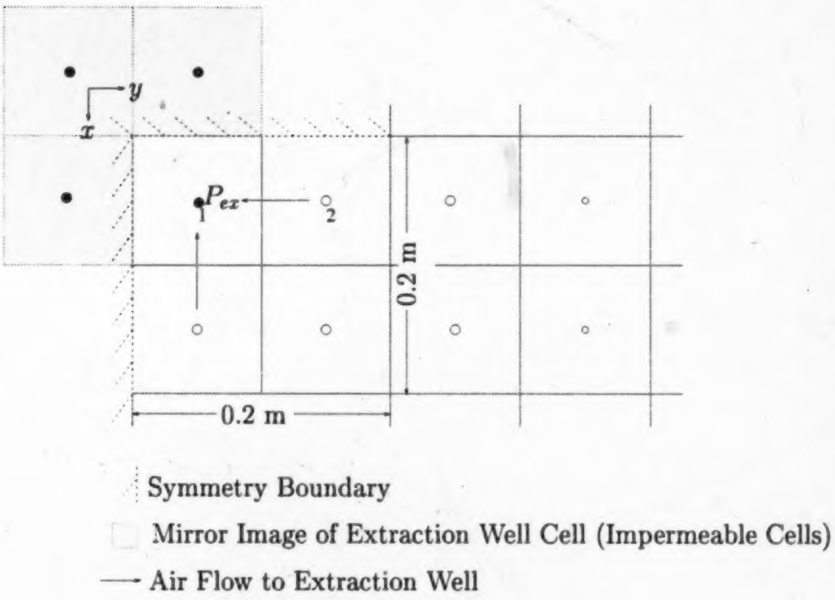
y
x
P_ex
1
2
0.2 m
0.2 m
Symmetry Boundary
Mirror Image of Extraction Well Cell (Impermeable Cells)
Air Flow to Extraction Well

Figure A.1: AIR3D quarter grid ($a3_q$)

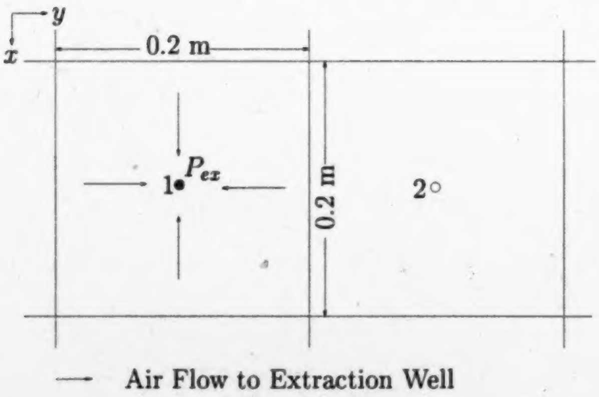
y
x
0.2 m
0.2 m
1
P_ex
2
Air Flow to Extraction Well

Figure A.2: AIR3D full initial grid (a3)

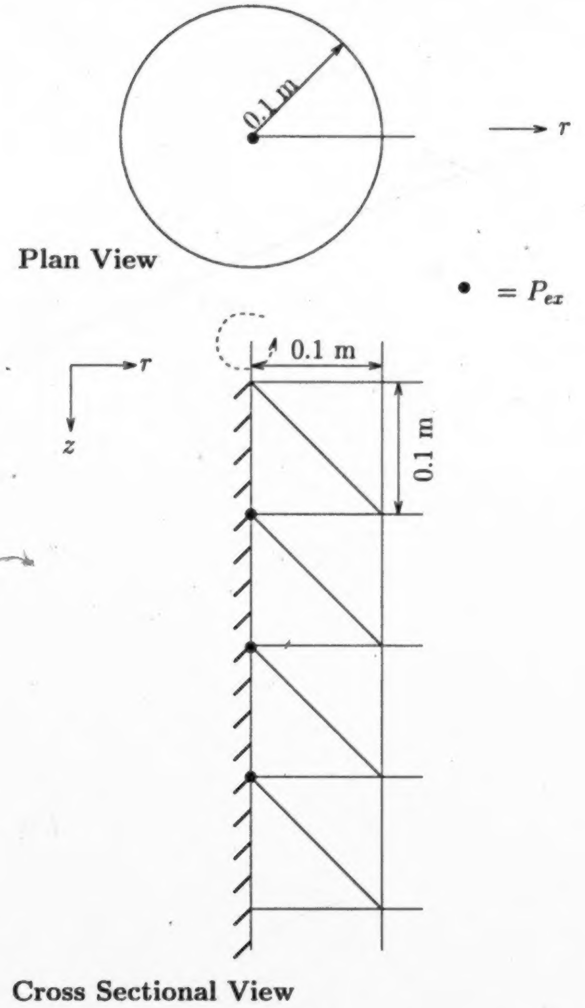
0.1 m
r
Plan View
● = P_{ex}
r
z
0.1 m
0.1 m
Cross Sectional View

Figure A.3: VapourT initial grid, $r_i = 0$ m (v1)

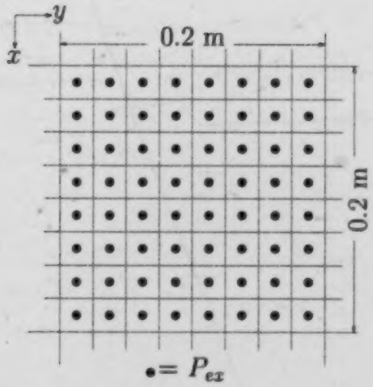
y
x
0.2 m
0.2 m
•= P_{ex}

Figure A.4: AIR3D full fine grid (a4)

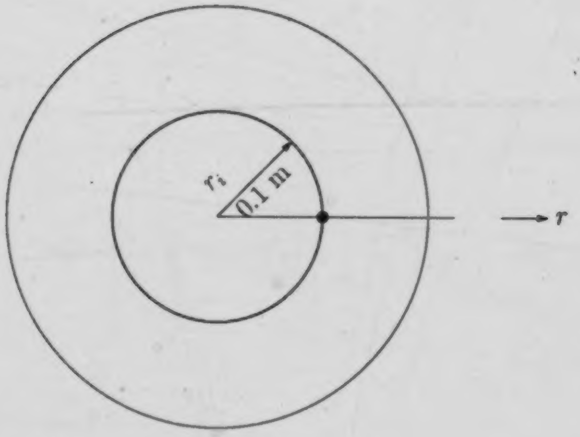

Plan View

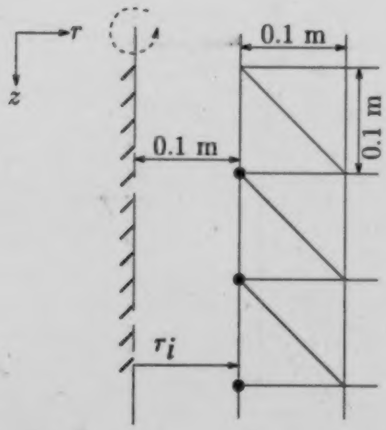
r
z
0.1 m
0.1 m
0.1 m
r_i

Cross Sectional View

Figure A.5: VapourT initial grid, $r_i = 0.1$ m ($\mathrm{v1}_r$)

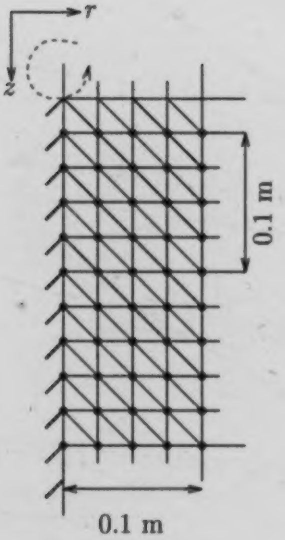

Cross Sectional View

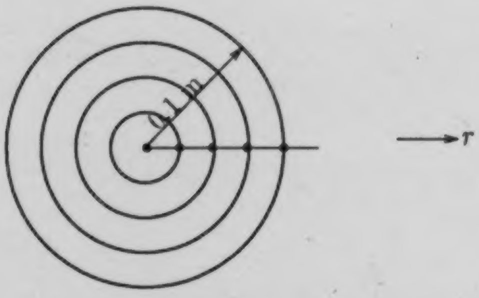

Plan View

Figure A.6: VapourT fine grid, $r_i = 0$ m, (v 2)

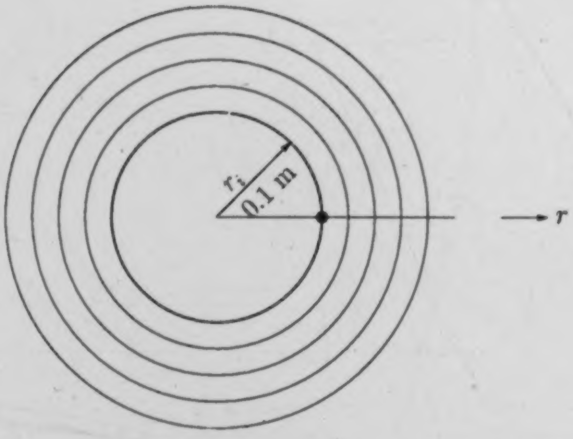

Plan View

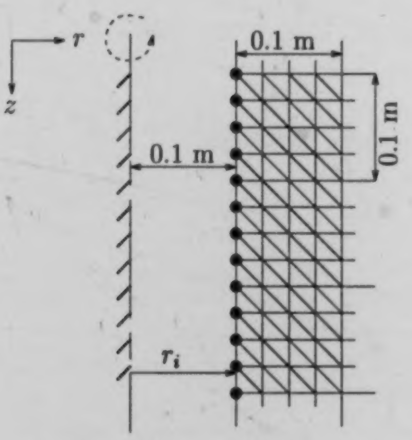
r
z
0.1 m
0.1 m
0.1 m
r_i

Cross Sectional View

Figure A.7: VapourT fine grid, $r_i = 0.1$ m (v2_r)

References

Abdul, A. S. 1988. Migration of petroleum products through sandy hydrogeologic systems. *Ground Water Monitoring Review*, **8**(4), 73–81.

Anderson, M. P., and Woessner, W. W. 1992. *Applied Groundwater Modeling: Simulation of Flow and Advective Transport.* San Diego, CA, USA: Academic Press, Inc.

Armstrong, J. E., Moore, B. J., Mendoza, C. A., and Hardisty, P. E. 1995. A comparison of horizontal versus vertical wells for soil vapour extraction. In: *Solutions '95, International Association of Hydrogeologists, International Congress XXVI*, 205-208.

Baehr, A. L. 1987. Selective transport of hydrocarbons in the unsaturated zone due to aqueous and vapor phase partitioning. *Water Resources Research*, **23**(10), 1926–1938.

Baehr, A. L., and Hult, M. F. 1991. Evaluation of unsaturated zone air permeability through pneumatic tests. *Water Resources Research*, **27**(10), 2605–2617.

Basinet, R., and Wollenberg, J. 1997. Petroleum hydrocarbons clean-up using soil vapor extraction and air sparging via horizontal wells at a commercial Navy site in San Diego, CA. In: *Fourth International In Situ and On-Site Bioremediation Symposium*, **1**, 205-208.

Bass, D. H. 1993. Estimation of effective cleanup radius for soil-vapor extraction systems. *Journal of Soil Contamination*, **2**(2), 191–202.

Bass, D. H. 1994. Prediction of vacuum distribution along perforated pipes in vented soil piles and SVE applications. In: *Proceedings of the 1994 Focus Conference on Eastern Regional Ground Water Issues*, 101-112.

Battaglia, A., and Morgan, D. J. 1994. Ex-situ forced aeration of soil piles: A physical model. *Environmental Progress*, **13**(3), 205–208.

Beckett, G. D., and Huntley, D. 1994. Characterization of flow parameters controlling soil vapor extraction. *Ground Water*, **32**(2), 239–247.

Beljin, M. S., and Losonsky, G. 1992. HWELL: A horizontal well model. In: *Proceedings of the 1992 Solving Ground Water Problems with Models Conference*, Ground Water Management, Book 9 of the Series, 45-54.

Clarke, A. N., Mutch, R. D. Jr., and Wilson, D. D. 1992. Results of a year long simulation of the end of a site remediation using in situ vapor stripping. In: *Proceedings of the Symposium on Soil Venting, Results of a Year Long Simulation of the End of a Site Remediation Using In Situ Vapor Stripping*, 229-247.

DePaoli, D. W., Herbes, S. E., Wilson, J. H., Solomon, D. K., Jennings, H. L., Hylton, T. D., and Hyquist, J. E. 1991. *Field demonstrations of in situ soil venting at Hill Air Force Base: JP-4 jet fuel spill site.* Tech. rept. Oak Ridge National Laboratory.

Dickinson, W., Dickinson, R. W., Crosby, T. W., and Head, H. N. 1986 (Dec.). Horizontal drilling beneath Superfund sites. In: *Proceedings of the 7th National Conference on Management of Uncontrolled Hazardous Waste Sites*, 258-263.

DiGiulio, D.C. 1996. *Evaluation of Soil Venting Application.* Chelsea, MI, USA: Ann Arbor Press. From EPA Environmental Engineering Sourcebook, edited by Russell J. Boulding, EPA/540/S-92/004. Pages 123–132.

Downs, C. E. 1996. Multimedia remediation applications of horizontal wells. In: *Proceedings of the Tenth National Outdoor Action Conference and Exposition; Aquifer Remediation, Ground Water Monitoring, Geophysical Method*, 237-252.

Eastcott, L., Shiu, W. Y., and Mackay, D. 1988. Environmentally relevant physical-chemical properties of hydrocarbons: A review of data and development of simple correlations. *Oil & Chemical Pollution*, 4, 191–216.

Falta, R. W. 1995. Analytical solutions for gas flow due to gas injection and extraction from horizontal wells. *Ground Water*, **33**(2), 235–246.

Fetter, C. W. 1993. *Contaminant Hydrogeology*. New York, NY, USA: Macmillan Publishing Company.

Fetter, C. W. 1994. *Applied Hydrogeology*. 3rd edn. New York, NY, USA: Macmillan Publishing Company.

Freeze, R. A., and Cherry, J. A. 1979. *Groundwater*. Englewood Cliffs, NJ, USA: Prentice-Hall, Inc.

Gannon, K., Wilson, D. J., Clarke, A. N., Mutch, R. D. Jr., and Clarke, J. H. 1989. Soil clean up by in-situ aeration. II. effects of impermeable caps, soil permeability, and evaporative cooling. *Separation Science and Technology*, **24**(11), 831–862.

Gibson, T. L., Abdul, A. S., Glasson, W. A., Ang, C. C., and Gatlin, D. W. 1993. Vapor extraction of volatile organic compounds from clay soil: a long-term field pilot study. *Ground Water*, **31**(4), 616–626.

Gilmour, S. L. 1996. *Numerical simulation of hydrocarbon and oxygen transport and microbial biodegradation during bioventing: application to a field study and sensitivity analysis*. M.Sc. Thesis, University of Alberta.

Goldfarb, A. S., Vogel, G. A., and Lundquist, D. E. 1994. Technical aspects of site remediation: soil vapor vacuum extraction. *Waste Management*, **14**(2), 153–159.

Hardy, L. 1997. Installation of a bio-venting remediation system using directionally drilled horizontal wells. In: *Proceedings of the Eleventh National Outdoor Action Conference and Exposition; Aquifer Remediation, Ground Water Monitoring, Geophysical Method*, 69-79.

Hubbert, M. K. 1940. The theory of groundwater motion. *Journal of Geology*, **48**, 785–944.

Johnson, P. C., and Ettinger, R. A. 1994. Considerations for the design of in situ vapor extraction systems: radius of influence vs. zone of remediation. *Ground Water Monitoring Research*, **14**(3), 123–128.

Johnson, P. C., Stanley, C. C., Kemblowski, M. W., Byers, D. L., and Cothart, J. D. 1990a. A practical approach to the design, operation, and monitoring of in-situ soil-venting systems. *Ground Water Monitoring Research*, **10**(2), 159–178.

Johnson, P. C., Kemblowski, M. W., and Colthart, J. D. 1990b. Quantitative analysis for the cleanup of hydrocarbon-contaminated soils by in-situ soil-venting. *Ground Water*, **28**(3), 413–429.

Jordan, D. L., Mercer, J. W., and Cohen, R. M. 1995. *Review of mathematical modeling for evaluating soil vapor extraction systems.* Tech. rept. GeoTrans, Inc. EPA/540/R-95/513.

Joss, C. J., and Baehr, A. L. 1993. A multispecies transport model to simulate vapor extraction and bioventing remediation of unsaturated zones contaminated with gasoline. In: *Water-Resources Investigations - U.S. Geological Survey Toxic Substances Hydrology Program; Proceedings of the Technical Meeting*, 61-63.

Joss, C. J., and Baehr, A. L. 1995. *AIR3D.* U.S. Geological Survey. Documentation of AIR3D, an adaptation of the ground-water flow code MODFLOW to simulate three-dimensional air flow in the unsaturated zone. Open-File Report 94-533.

Kaback, D., Looney, B. B., Eddy, C. E., and Hazen, T. C. 1991. Innovative ground water and soil remediation: in situ air stripping using horizontal wells. In: *Proceedings of the Fifth National Outdoor Action Conference on Aquifer Restoration, Ground Water Monitoring and Geophysical Methods*, 47-58.

Karlsson, H., and Bitto, R. 1990. New horizontal wellbore system for monitor and remedial wells. In: *Superfund '90...Proceedings of the National Conference.* Silver Spring, MD, USA: Hazardous Materials Control Research Institute. 357-362.

Kidder, R.E. 1957. Unsteady flow of gas through a semi-infinite porous medium. *Journal of Applied Mechanics*, **24**, 329–332. ASME.

Komex, International Ltd. 1994a (Mar.). *1993 Soil vapour extraction program bioventing.* Tech. rept. Draft Appendix, A93-2327-5-4.

Komex, International Ltd. 1994b (Mar.). *1993 Soil vapour extraction program summary report.* Tech. rept. Draft, KI93-2327-5-4.

Komex, International Ltd. 1994c. *1994 Remediation activities and results, (Site B).* Tech. rept.

Komex, International Ltd. 1994d (June). *Soil vapour extraction and bioventing program, summary report 1993 to spring 1994.* Tech. rept. Prepared for: Canadian Association of Petroleum Producers.

Komex, International Ltd. 1996 (Apr.). *Subsurface remedial technology. Research and demonstration program. Horizontal soil vapour extraction. Pilot test summary report.* Tech. rept. Prepared for: Canadian Producers of Petroleum Producers. A94-2327-10.

Kremesec, V. J. Jr., Jeng, C.Y, Wendrow, B., and Trevino, F. M. 1995. The pilot testing and full scale design of horizontal wells for bioventing/SVE applications. In: *Proceedings of the 1995 Petroleum Hydrocarbons and Organic Chemicals in*

Ground Water: Prevention, Detection and Restoration Conference and Exposition, 543-562.

Marley, M. C., Nangeroni, P. E., Cliff, B. L., and Polonsky, J. D. 1990. Air flow modeling for in-situ evaluation of soil properties and engineered vapor extraction system design. In: *Proceedings of the Fourth National Outdoor Conference on Aquifer Restoration, Ground Water Monitoring and Geophysical Methods*, 651-665.

Massmann, J. W. 1989. Applying groundwater flow models in vapor extraction system design. *Journal of Environmental Engineering*, **115**(1), 129–149.

Massmann, J. W., and Madden, M. 1994. Estimating air conductivity and porosity from vadose zone pumping tests. *Journal of Environmental Engineering*, **120**(2), 313–327.

Mast, V. 1996. Horizontal vs. vertical wells - which to use when. Advantages and disadvantages to both for sparging and vapor extraction. *Soil Groundwater Cleanup*, Apr.

McDonald, M. G., and Harbaugh, A. L. 1988. *MODFLOW: A modular three-dimensional finite-difference ground-water flow model.* U.S. Geological Survey Techniques of Water-Resources Investigations, U.S.G.S Book 6 - Modelling Techniques.

McWhorter, D. B. 1990. Unsteady radial flow of gas in the vadose zone. *Journal of Contaminant Hydrology*, **5**(3), 297–314.

Mendoza, C. A. 1992 (Feb.). *VapourT.* University of Alberta. User's Guide.

Mendoza, C. A., and Frind, E. O. 1990. Advective-dispersive transport of dense organic vapors in the unsaturated zone 1. model development. *Water Resources Research*, **26**(3), 379–387.

Mendoza, C. A., Therrien, R., and Sudicky, E.A. 1994. *ORTHOFEM.* User's Guide, Version 1.04.

Mendoza, C. A., Johnson, R. L., and Gillham, R. W. 1996. *Chapter 6: Vapor Migration in the Vadose Zone.* Portland, OR, USA: Waterloo Press. From: Dense Chlorinated Solvents and other DNAPLs in Groundwater, edited by J.F. Pankow and J.A. Cherry.

Mohr, D. A., and Merz, P. H. 1995. Application of a 2D air flow model to soil vapor extraction and bioventing case studies. *Ground Water*, **33**(3), 433–444.

Morgan, J. H. 1992. Horizontal drilling applications of petroleum technologies for environmental purposes. *Ground Water Monitoring Review*, Summer, 98–102.

Pollock, D. W. 1989. *MODPATH.* U.S. Geological Survey. Documentation of computer programs to compute and display pathlines using results from the U.S. geological survey modular three-dimensional finite-difference ground-water flow model. Open-File Report 89-381.

Rathfelder, K., Yeh, W. W-G., and Mackay, D. 1991. Mathematical simulation of soil vapor extraction systems: model development and numerical examples. *Journal of Contaminant Hydrology*, **8**, 263–297.

Rathfelder, K., Lang, J. R., and Abriola, L. M. 1995. *Soil vapor extraction and bioventing: applications, limitations, and future research directions.* Tech. rept. International Union of Geodesy and Geophysics. Reviews of Geophysics, supplement, Paper Number 95RG00402.

Russell, D. L. 1996. Using horizontal wells as a remediation tool. *Environmental Protection*, Jan., 36–43.

Sawyer, C. S., and Kamakoti, M. 1998. Optimal flow rates and well locations for soil vapor extraction design. *Journal of Contaminant Hydrology*, **32**(1-2), 63–76.

Sepehr, M., and Samani, Z. A. 1993. In situ soil remediation using vapor extraction wells, development and testing of a three-dimensional finite-difference model. *Ground Water*, **31**(3), 425–436.

Shan, C., and Falta, R. W. 1992. Analytical solutions for steady-state gas flow to a soil vapor extraction well in the unsaturated zone. *Water Resources Research*, **28**(4), 1105–1120.

Wade, A., Wallace, G.W., Siegwald, S.F., Lee, W.A., and McKinney, K.C. 1996. Performance comparison between a horizontal and a vertical air sparging well: a full-scale one-year pilot study. In: *Proceedings of the National Outdoor Action Conference on Aquifer Restoration, Ground Water Monitoring and Geophysical Methods*, 189-206.

Wang, H. F., and Anderson, M. P. 1982. *Introduction to Groundwater Modelling: Finite Difference and Finite Element Methods.* New York, NY, USA: W.H. Freeman and Company.

Welty, C., Joss, C. J., and Baehr, A. L. 1996. Optimizing the design of vapor-extraction remediation systems for removal of organic contaminants from the unsaturated zone. In: *Water-Resources Investigations - U.S. Geological Survey Toxic Substances Hydrology Program; Proceedings of the Technical Meeting*, 55-59.

White, F. M. 1986. *Fluid Mechanics.* 2nd edn. New York, NY, USA: McGraw-Hill, Inc.

Wilson, D. D., and Kaback, D. S. 1993 (July). *Industry survey for horizontal wells, final report.* Tech. rept. U.S. Department of Energy and Westinghouse Savannah River Company and CDM Federal Programs Corporation. Prepared by CDM Federal Programs Corporation.

Wilson, D. J., and Losonsky, G. 1995. Horizontal environmental well cost evaluation methods. *ASME Drilling Technology*, **65**, 43–50.